Enhancement of Fiber Optical Environmental Sensor Performance Via All-Optical Signal Processing

by

Ole Krarup

A thesis submitted in conformity with the requirements
for the degree of Doctor of Philosophy

Ottawa-Carleton Institute for Physics, Department of Physics
University of Ottawa

Enhancement of Fiber Optical Environmental Sensor Performance Via All-Optical Signal Processing

Ole Krarup
Doctor of Philosophy

Department of Physics
University of Ottawa
2024

Abstract

The manipulation of signals is crucial for countless technologies that support the modern world. From electrical circuits turning modulated radio-waves into sound to optical amplifiers and transceivers handling laser pulses used for digital internet communication, the need for flexible methods that enhance signal quality to improve performance has grown steadily. When handling optical signals representing telecommunications data or measurements from fiber optical environmental sensors, limiting factors include the fundamental physics governing the wave-like nature of photons and the electronics utilized to generate and detect light. For example, the spectral width of an optical cavity is determined by the way light reflects off its end faces, while detecting the interference of two lasers with a frequency difference greater than around 100 GHz is difficult because the response time of electrical components used for detection is too long for such fast variations to be measured. To overcome such limitations and maximize performance, methods for all-optical signal processing, where power-dependent effects in waveguides, such as the Kerr effect, are exploited, have been developed to reshape optical signals before they are detected electronically.

This thesis presents a collection of novel methods for utilizing the Kerr effect to pre-process laser signals from fiber optical environmental sensors. First, the operational principles of a set of fiber optical sensing techniques based on fiber Bragg gratings, chirped pulse optical time domain reflectometry and polarimetry are discussed along with their associated limitations. Results of theoretical analysis show that propagation of two lasers with different frequencies in an optical fiber having a

large power-dependent electric susceptibility gives rise to frequency sidebands. The optical power of these sidebands is expressed in terms of the parameters of the input lasers, and the possibilities for exploiting these sidebands to enhance the performance of environmental sensors are demonstrated via four peer-reviewed papers.

The first paper details how to potentiate the power of a laser signal from a fiber-based temperature sensor and thus increase its resolution by extracting the frequency sidebands generated when launching it and a second laser into a nonlinear medium.

The second paper shows that launching pulses undergoing a frequency sweep and a fixed frequency laser into a nonlinear medium causes higher order sidebands to sweep frequency ranges that are integer multiples of the incident one. In collaboration with a fellow PhD student, this effect is utilized to extend the sensing range of a distributed temperature sensor based on chirped pulse optical time domain reflectometry.

The third paper presents a novel model describing the impact of optical polarization on the generation of sidebands. The effects described by the model are practically utilized for enhancing the sensitivity of a polarimetric optical sensor that measures changes in applied strain.

In the fourth paper, the model presented in the third paper is exploited to develop a novel polarimetry method, which exploits the relationship between laser polarization and sideband power to determine the state of polarization of a laser under test by all-optical means.

Finally, the contributions of this thesis to research on all-optical signal processing are summarized and avenues for further experimental research enabled by this publication are discussed.

The extension of an analytical model of sideband generation to account for polarization and the experimental demonstration of its practical applications constitute the most significant contributions of this thesis to the field of all-optical signal processing as the equations describing laser signals in nonlinear media rarely admit analytical solutions.

To my family

Acknowledgments

This thesis would not have been possible without the assistance and advice of a great number of people. I wish to thank my supervisor, Professor Xiaoyi Bao, for accepting my application for becoming a PhD student in her group and for providing insightful comments and suggestions throughout my research. I would also like to thank Dr. Chams Baker for closely mentoring me and providing inspiration for the experiments presented in this work. For creating a productive research environment with plenty of enlightening discussions, I would like to thank my colleagues and fellow students, Mr. Yuan Wang, Mr. Benoit Vanus, Mr. Haiyang Wang, Mr. Chen Chen, Dr. Song Gao, Dr. Bhavaye Saxena, Dr. Pedro Tovar Braga, Mr. Zichao Zhou and Professor Liang Chen.

My four years as a research assistant in the Fiber Optics Group at the University of Ottawa was funded by the following NSERC grants; RGPIN/06302-2020, RGPIN/06071-2015, 506628/STPGP/2017, and CRDPJ/479630-2015. Charitable financial support for my research was kindly provided by Marie & MB Richter's Foundation (DKK 20.000) and Thomas B. Thriges Foundation (DKK 25.000). The generous support of the Ontario Student Assistance Program should also be acknowledged.

I wish to thank David Boertjes and Alex MacKay of the Ciena Corporation for selecting me for an exciting internship during the summer of 2021 and Suet Yuen of the Infinera Corporation for recruiting me as a part time optical test engineer during the fall of 2021. The experience I gathered in these roles have both been useful in my research and provided a great start to my professional career.

I also wish to thank Ms. Habon Maxamud for expertly developing my potential and for patiently listening to my often long winded explanations.

Finally, I must thank my family for their unwavering support during four years of separation and for the tremendous effort they have expended to stay in touch with me and strengthen the connections I have made in Canada.

Contents

List of Figures

List of Tables

Acronyms

CC Cross-Correlation

CP-OTDR Chirped Pulse OTDR

DFB Distributed Feedback

EDFA Erbium Doped Fiber Amplifier

FBG Fiber Bragg Grating

FFT Fast Fourier Transform

FP Fabry-Pérot

FUT Fiber Under Test

FWHM Full Width at Half Maximum

MWE Maxwell's Equations

NLSE Nonlinear Schrodinger equation

OFDR Optical Frequency Domain Reflectometry

OPD Optical Path Difference

OTDR Optical Time Domain Reflectometry

P-OTDR Polarization OTDR

RFGA Random Fiber Grating Array

SOA Solid State Optical Amplifier

SOP State of Polarization

SOTA State of the Art

SSFM Split-Step Fourier Method

TDR Time Doman Reflectometry

Chapter 1

Introduction

Since ancient times, light as a phenomenon and metaphor has been viewed as central to a great number of cultures and religious traditions [5]. Additionally, the nature of light has been pondered and probed by thinkers throughout history [6]. Greek philosophers debated whether sight arose from the eye capturing a substance emitted by objects or ray-like extramissions from the eye itself reaching out and "touching" objects analogous to a grasping hand [7]. In book 10 of "The Republic", Plato mentions the phenomenon now referred to as "refraction", using the example of a straight rod appearing crooked when partially submerged in water to caution the reader against fallacies arising from the human mind and senses [8]. Medieval Arab scholars such as Al-Kindi and Ibn Sahl developed the theoretical understanding of sight by rejecting the extramission theory and produced practical treaties on lenses and mirrors [9]. Latin translations of these works would inspire European scholars including Huygens and Newton to conduct their own investigations and debate whether light fundamentally consists of discrete particles or continuous waves - a discussion, which arguably remains unresolved to this day [10, 11, 12]. Subsequent efforts by Victorian scientists like Ørsted, Faraday and Ampere to describe electricity and magnetism, phenomena previously considered unrelated to light, led Maxwell to formulate his famous equations, which allow for wave-like solutions propagating at a speed suggestively close to the value of the speed of light first measured by Rømer [13, 11] and later refined by Fizeau [14]. At the turn of the twentieth century, a number of seemingly contradictory experimental results involving light were resolved by Einstein's theory of relativity [15], while Planck pioneered the description of light as discrete packets of energy [16]. Modern quantum mechanical theories of light have provided additional insight and spurred the ongoing development of experimental optics.

Along with scholarly investigations of light, communication based on optical signals has been utilized in many different forms. Examples include arrays of beacon fires

alerting settlements to approaching enemy fleets [17], lighthouses guiding merchant ships to safety [18] and the semaphore system relaying symbols manually adjusted by mechanical means across a network of towers before the advent of the electrical telegraph [19]. With pioneering experiments by Jean-Daniel Colladon in 1842 on total internal reflection [20] and Alexander Graham Bell in 1880 on the photophone laying important groundwork [21], the first fiber optical data transmission was conducted by Manfred Börner in 1965 [22]. Subsequent research, notably by Charles Kao, substantially increased the purity of silica fibers and reduced their attenuation to less than 0.5 dB/km in the near-infrared range from 1000 nm to 2000 nm, thereby enabling modern high-speed internet communication [23, 24]. Inventions such as the erbium doped fiber amplifier (EDFA) [25, 26] and the wavelength selective switch [27] have played crucial roles by efficiently amplifying in-line optical signals and rerouting them with great flexibility. Furthermore, comprehensive theoretical models of nonlinear effects in optical fibers caused by the interaction of a strong optical fields with the glass has allowed for the development of Raman amplifiers [28] and an understanding of nonlinear distortions, which can limit signal quality [29, 30].

In parallel with the deployment of optical fibers for telecommunication, the need for reliable monitoring of critical infrastructure such as hydrocarbon pipelines, highway tunnels, chemical plants and hydroelectric dams has given rise to the field of fiber optical sensing. By exploiting the fact that changes in the surroundings of an optical fiber can alter the intensity, phase, frequency and polarization of light propagating within, an assortment of optical sensing approaches have been developed, which for certain applications compare favorably to electrically based sensors. In particular, the chemical and electrical inertness of silica glass along with the durability and small size of fiber sensors make them ideal in harsh environments, where traditional sensors would be too bulky, degrade or have their readings disturbed by electromagnetic interference [31]. Techniques such as optical time domain reflectometry (OTDR) and optical frequency domain reflectometry (OFDR) allow users to record the properties of a fiber along its entire length and relate these measurements to changes in the environment through a calibration. Applications involve utilizing existing telecommunication fibers as geophones to monitor traffic and seismic activity, locating leaks in pipelines and detecting fires in highway tunnels and industrial assembly lines [32]. For measuring particular locations with high sensitivity, sensors relying on fiber Bragg gratings (FBG) and Fabry-Pérot (FP) cavities have been developed[1, 33]. The best possible performance of such sensing schemes in terms of resolution, sensitivity and range is fundamentally determined by the physical properties of light. For example, the ability to determine shifts in the central frequency of a spectral line of an FP cav-

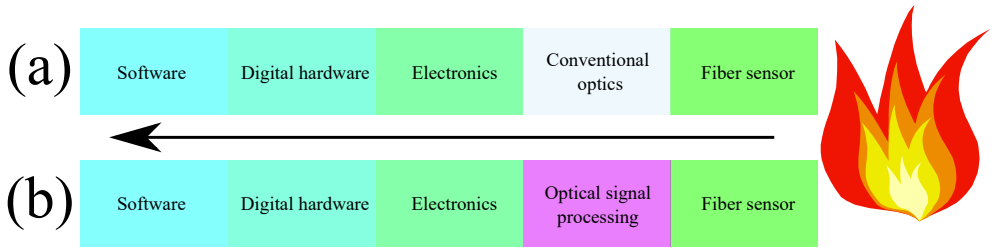

Figure 1.1: (a) Conventional fiber optical sensing "pipeline", where each step imposes certain restrictions on sensor performance when detecting an environmental change. (b) Sensing pipeline utilized in this work, where processing of sensor signals using exotic optical effects in fibers mitigates limitations caused by the other steps.

ity is limited by the spectral width of the line, which is governed by the fundamental physics of light reflecting off two closely spaced surfaces. Similarly, the performance of conventional optical devices is limited by fundamental physics and associated engineering constraints. For example, if a beam of light containing two wavelengths, λ_1 and λ_2 with $\lambda_1 > \lambda_2$, is incident upon N lines of a diffraction grating and the m^{th} diffraction order is considered, their respective interference peaks can be distinguished if $\lambda_1/(\lambda_1 - \lambda_2) \leq mN$ [34]. Thus, the achievable frequency bandwidth of a grating-based optical filter is determined by the wave-like nature of light, which in turn places demands on the practical design of the filter. In addition, the electronics used to control, modulate and detect the laser light used in fiber optical sensing imposes further limitations on sensor performance. For instance, most commercially available signal generators, photodiodes and oscilloscopes are constrained to operation below 100 GHz, which reduces the range of possible measurements. Furthermore, a detected sensor signal is typically digitized and processed by an electronic computer, making CPU clock speed, which is currently limited to approximately 5 GHz in commercially available systems, as well as algorithmic performance additional limiting factors when doing real-time measurements or processing large amounts of data.

To supersede these fundamental, electronic and digital limitations and enhance the performance of sensors monitoring crucial infrastructure that the modern world depends on, one must seemingly engineer more refined physical sensors, electronic components and computers. Alternatively, one can deploy optical signal processing techniques [35, 36, 37], which exploit exotic effects in optical fibers to reshape sensor signals before electronic detection while they are still in the optical domain as visualized in Fig. 1.1.

Utilizing a "thesis by paper" format, where four published articles are presented, this publication contributes to previous research into strategies for using the Kerr effect to optically process signals from fiber optical sensors and enhance their perfor-

mance beyond the limitations imposed by conventional approaches [38, 39]. Chapter 2 provides an overview of the conventional fiber optical sensing techniques deployed in this thesis and highlight limitations that can be overcome using all-optical signal processing. Chapter 3 derives the Nonlinear Schrödinger Equatuon (NLSE) from first principles and presents a novel analytical model describing the generation of frequency sidebands in a nonlinear medium while taking the effect of optical polarization into account. The practical implications of this model for enhancing the methods described in Chapter 2 are then discussed. Chapter 4 contains the paper titled "Nonlinear resolution enhancement of an FBG based temperature sensor using the Kerr effect" and a further discussion of its results. Chapter 5 contains the paper titled "Frequency sweep extension using the Kerr effect for static temperature measurement range enhancement in Chirped Pulse ϕ-OTDR" written in close collaboration with Yuan Wang, along with a clarification of the contributions of each author and a discussion of the paper. Chapter 6 contains the paper titled "Sensitivity enhancement of fiber optical polarimetric sensors using self-induced nonlinear phase modulation via the Kerr effect", which presents a practical application of the novel model in Chapter 3 for taking optical polarization into account when describing sideband generation. Chapter 7 contains the paper titled "All-optical polarimeter for laser Stokes vector measurement using self-induced nonlinear phase modulation", showing how the dependence of sideband power on optical polarization can be exploited to construct an all-optical polarimeter. Finally, Chapter 8 summarizes the contributions of this thesis and presents avenues for future research.

Chapter 2

Fiber optical sensing

The sense of sight allows light from the surrounding environment to be collected by photoreceptors in the retina and converted to electrical signals interpreted by the brain. Changes in the brightness of light or shifts in its colour can convey vital information over large distances such as the ripeness of food sources or the presence of predators. In scientific applications, John Mitchell's torsion balance allowed Henry Cavendish and Charles-Augustin de Coulomb to investigate the strengths of gravitational and electrical forces respectively by observing changes in the orientation of a ray of sunshine reflected by a rotatable mirror [40]. Additionally, lunar retro-reflectors allowing terrestrial lasers to measure changes in the orbit of the Moon [41], is another example of light being applied to encode information about physical systems.

This chapter explains the principles underlying the fiber optical environmental sensing techniques utilized in this thesis, including FBG based sensors, chirped pulse OTDR (CP-OTDR) and polarimetric sensing. The factors determining the performance of these sensing techniques are discussed and the potential benefits of overcoming their limitations are highlighted.

2.1 FBG based sensors

A person gazing through a window will both see light transmitted through the glass from the outside and a reflection of themselves. The reflection occurs when light from the person's body encounters the discrete change in the refractive index that occurs at the interface between air and glass. A full description of a single reflection taking the effects of incident angle and optical polarization into account was first produced by Augustin-Jean Fresnel [42] by modelling light as longitudinal waves, while modern descriptions based on Maxwell's equations (MWE) model light as transverse waves [43]. The advanced case of multiple reflections from a large number of interfaces with spac-

ings close to the wavelength of light is highly relevant to fiber optical sensing. An FBG consists of a fiber segment whose refractive index changes periodically due to exposure to interfering ultraviolet light or high power laser pulses, causing light at a particular range of wavelengths to be strongly reflected as shown in Fig. 2.1 [1]. This section explores the fundamental physics of FBGs, and how they are typically employed in environmental sensing.

2.1.1 Theoretical FBG model

The following explanation of the properties of an FBG is based on the one presented in [44]. In the frequency domain, Maxwell's equations in a uniform, linear dielectric can be expressed as

$$\nabla^2 \tilde{\boldsymbol{E}} + \frac{\omega^2}{c^2}\tilde{\boldsymbol{E}} + \mu_0 \omega^2 \tilde{\boldsymbol{P}} = 0, \tag{2.1}$$

where $\tilde{\boldsymbol{E}}$ and $\tilde{\boldsymbol{P}}$ are the frequency domain representations of the electric field and material polarization density respectively. Introducing a small non-uniformity in the dielectric, the polarization of the material can be written as the sum of its unperturbed polarization, $\tilde{\boldsymbol{P}}_{\boldsymbol{0}}$, and a perturbation, $\tilde{\boldsymbol{P}}_{\boldsymbol{p}}$, according to

$$\nabla^2 \tilde{\boldsymbol{E}} + \frac{\omega^2}{c^2}\tilde{\boldsymbol{E}} + \mu_0 \omega^2 \tilde{\boldsymbol{P}}_0 = -\mu_0 \omega^2 \tilde{\boldsymbol{P}}_p. \tag{2.2}$$

Exploiting that $\tilde{\boldsymbol{P}}_0 = \epsilon_0(n^2 - 1)\tilde{\boldsymbol{E}}$ yields

$$\nabla^2 \tilde{\boldsymbol{E}} + k_0^2 n^2 \tilde{\boldsymbol{E}} = -\mu_0 \omega^2 \tilde{\boldsymbol{P}}_p, \tag{2.3}$$

where $k_0 = \omega/c = 2\pi/\lambda_0$ with λ_0 being the vacuum wavelength of the light and n being the refractive index. A similar differential equation for $\tilde{\boldsymbol{B}}(\boldsymbol{r}, \omega)$ can be derived. A solution can be obtained in cylindrical coordinates using separation of variables if the perturbation in Eq. 2.3 is ignored. Specifically, the solution to Maxwell's equations in a cylindrical waveguide, such as an optical fiber, implies that the radial and angular parts of the electric field can be expressed in terms of the longitudinal part, which can be described using the ansatz,

$$\tilde{E}_z(\boldsymbol{r}, \omega) = A(\omega)G(\rho)\exp(im\phi)\exp(i\beta(\omega)z), \tag{2.4}$$

with an analogous ansatz for $\tilde{B}_z(\boldsymbol{r}, \omega)$. In Eq. 2.4, $A(\omega)$ is the amplitude of the electric field component oscillating with an angular frequency, ω, $G(\rho)$ is the transverse envelope of the field, while m is an integer and $\beta(\omega)$ is the propagation constant for

a field with an angular frequency of ω. Substituting Eq. 2.4 into Eq. 2.3 with $\tilde{\boldsymbol{P}}_p = 0$ produces the differential equation

$$\partial_\rho^2 G + \rho^{-1}\partial_\rho G + \left(n^2(\omega)k_0^2 - \beta^2(\omega) - \rho^{-2}m^2\right) G = 0, \tag{2.5}$$

which is the differential equation defining Bessel functions [45]. Assuming that the fiber consists of a core of radius a with a refractive index of n_{co} surrounded by a cladding with a refractive index of n_{cl}, which is slightly smaller than n_{co} ensures single mode propagation for a certain range of wavelengths [46]. The propagation constant of a mode, $\beta(\omega)$, satisfies $n_{cl}^2 k_0^2 \leq \beta^2(\omega) \leq n_{co}^2 k_0^2$ and its dependence on the angular frequency of the field causes light at different frequencies to experience different phase- and group velocities, leading to dispersion. Assuming constant linear polarization and a monochromatic field, the electric field amplitude in region of the fiber where the perturbation is located can be written as a linear combination of fields moving in the forward (F) and backward (B) directions,

$$\tilde{E} = \tilde{F}(z)\varepsilon(x,y)e^{-i\beta z} + \tilde{B}(z)\varepsilon(x,y)e^{i\beta z}, \tag{2.6}$$

where $\int \epsilon(x,y)\epsilon^*(x,y)dxdy = 2\omega\mu_0/\beta$. Substituting Eq. 2.6 into Eq. 2.3, integrating over the transverse direction and assuming a slowly varying envelope as well as a perturbation to the refractive index, δn, which is small compared to the refractive index of the core, yields the following differential equation,

$$e^{-i\beta z}\partial_z \tilde{F} - e^{i\beta z}\partial_z \tilde{B} = -i\frac{k_0^2}{\beta} n_0 \delta n (\tilde{F}e^{-i\beta z} + \tilde{B}e^{i\beta z}), \tag{2.7}$$

which describes how the perturbation causes coupling between the forward and backward propagating fields. The periodic perturbation to the refractive index is now modelled as

$$\delta n = n_a + n_a \nu(z)\cos(Kz) = n_a + n_a \nu(z)\frac{1}{2}(e^{iKz} + e^{-iKz}), \tag{2.8}$$

where n_a is the amplitude of the variation of the refractive index, $K = 2\pi/\Lambda$ with Λ being the distance between two maxima in the refractive index, and $0 \leq \nu(z) \leq 1$ is the envelope or "apodization" of the periodic perturbation. Substituting Eq. 2.8 into Eq. 2.7 and noting that only terms with no exponential factor or ones containing exponentials of $K - 2\beta \approx 0$ will vary slowly enough to contribute yields two coupled

equations for $\tilde{F}'$ and $\tilde{B}'$,

$$\tilde{F}' = -iM\tilde{F} - i\kappa e^{i(K-2\beta)z}\tilde{B} \tag{2.9}$$

$$\tilde{B}' = iM\tilde{B} + i\kappa e^{-i(K-2\beta)z}\tilde{F}, \tag{2.10}$$

where $M = k_0^2 n_0 n_a/\beta$ determines the propagation of each field through the grating and $\kappa = k_0^2 n_0 n_a \nu(z)/2\beta$ determines how field strength is transferred between the forward propagating and backward propagating modes. Further rewriting these equations, one can solve them in the "weak grating limit", where the perturbation is so small that the magnitude of $\tilde{F}$ is unchanged at the end of the grating. In this case, one can further assume that no light is launched backward from the end of the grating and obtain its reflection coefficient,

$$r = -i\mathfrak{F}(\kappa(z))\{2\delta\}, \tag{2.11}$$

where $\mathfrak{F}$ is the Fourier transform and $\delta = \beta - K/2 + M$. The fact that the reflection coefficient of a weak grating is related to the Fourier transform of the grating profile implies, for example, that a weak, uniform grating of finite length will have a reflection spectrum shaped like the *sinc* function as visualized in 2.1(b) centered at the so-called "Bragg wavelength",

$$\lambda_B = 2n_{av}\Lambda, \tag{2.12}$$

where n_{av} is the average refractive index along the grating. Conversely, a weak grating with a *sinc*-shaped envelope will have a uniform, square-shaped reflection spectrum. While derived for the simplified situation, where the field propagating in the forward direction remains unchanged, the intuition that the grating profile and its reflection spectrum are related by the Fourier transform remains useful for the general case. Assuming a weak, uniform grating of finite length, the width of the central peak is approximately

$$\Delta\lambda \approx \frac{\lambda_B^2}{n_{av}L} = \frac{4n_{av}\Lambda^2}{L}. \tag{2.13}$$

2.1.2 FBG sensing

To conduct environmental sensing using FBGs, it is necessary to measure the light they reflect. If a small change in the temperature of the grating occurs, its central

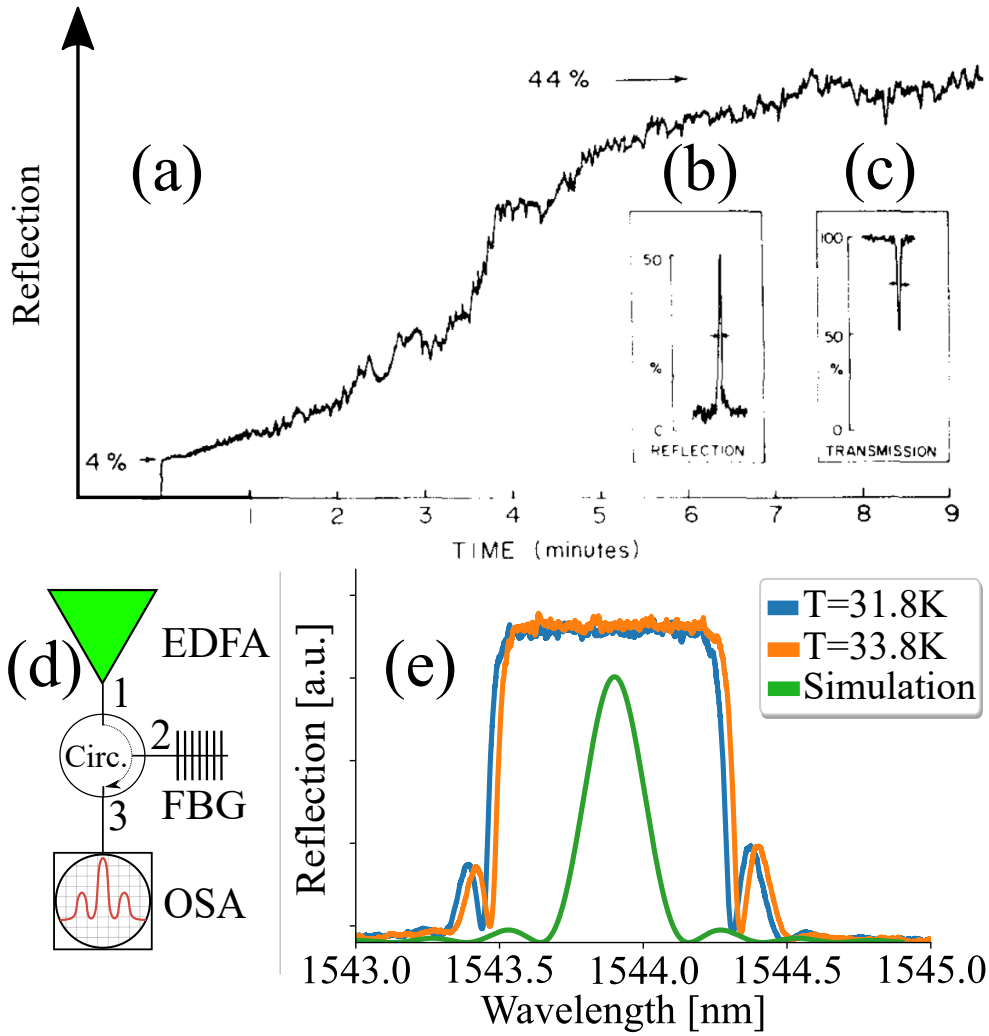

Figure 2.1: (a) Figure modified from [1] showing increased peak reflection over time as the grating is etched by exposure to interfering laser beams. (b) Reflection spectrum of a grating. (c) transmission spectrum of the same grating as in (b). (d) Experimental setup used for measuring the reflection spectrum of an FBG to reproduce the results in [1]. (e) Experimental data collected using the setup in (d), showing reflection spectra for a strong grating at two different temperatures and the theoretical reflection spectrum for a weak, uniform grating calculated using Eq. 2.11 for comparison. A temperature change of 2 K is discernible from the shift in the central wavelength.

wavelength described by Eq. 2.12 will shift according to

$$\Delta\lambda_B = 2\left(\Lambda\frac{\partial n_{av}}{\partial T} + n_{av}\frac{\partial\Lambda}{\partial T}\right)\Delta T, \tag{2.14}$$

with a similar expression applying for the case of strain. By recording the central wavelength for a range of known temperatures, a calibration allows the grating to be used as a thermometer. According to Eq. 2.14, the sensitivity of an FBG based thermometer is determined by how much the refractive index and the grating period change when the temperature is altered, while the resolution is limited by the spectral width of the grating given by Eq. 2.13. To achieve higher resolutions, one must either manufacture gratings with novel structures that minimize the bandwidth, such as π-shifted gratings [47] or develop a nonlinear interrogation method that can more accurately measure changes in the central wavelength.

2.2 Distributed measurements with Phase-OTDR

Echolocation refers to an approach for remote sensing, where reflections of a short emitted pulse are measured over time. Examples include radar, which uses microwave bursts to determine the location and speed of aircraft [48], and animals using short acoustic emissions to detect prey [49, 50]. With the rise of consumer telephony leading to the installation of increasingly large networks of copper cables, the ability to remotely inspect them for damage and cuts became crucial for ensuring reliable performance. To this end, time domain reflectometry (TDR) [51] was developed, where electrical pulses are launched into a wire and reflections caused by changes in impedance are detected. Similarly, the rise of fiber optical networks motivated the development of optical time domain reflectometry (OTDR), where light back-scattered by optical pulses launched into a fiber can reveal the presence of faults or changes in the environment surrounding the fiber. If a square pulse with a duration, D, and peak power, P_0, is launched at a time $t_0 = 0$ into a medium, where it propagates with a group velocity, v_g, the backscattered power measured at a time $t > t_0$ stems from a location, $z = v_g t/2$ in the medium, as light measured at, say, $t = 20\mu$s must have spent 10μs reaching the location from which it was scattered and an identical 10μs travelling back through the medium to the detector. Consequently, since the beginning and end of the pulse are separated by a time duration, D, the spatial resolution of the sensing system is $\Delta z = v_g D/2$. In the simplest case, where the coherence time of the light source is much shorter than the pulse duration, and a uniform power attenuation coefficient, α, along with a uniform field reflection coefficient, r, can be

assumed, the measured back-scattered power as a function of distance is

$$P_{bs} = \frac{r^2 D v_g P_0 e^{-2\alpha z}}{2}. \tag{2.15}$$

This approach to OTDR is typically used to inspect long fiber spans in telecommunication networks for cuts, bending loss and other sources of excess attenuation. A more sophisticated approach uses a laser, whose coherence time exceeds the duration of the pulse [2]. This allows light scattered from segments within the pulse width to form an interference pattern, which is sensitive to changes in the phase of the scattered light caused by changes in the environment surrounding the fiber. To model the interference, a fiber of length, L, can be divided into a large number of discrete segments of length, ΔL, where each of these contain M scattering centers [52, 53]. If j indicates the j^{th} fiber segment and m indicates the m^{th} scattering center within that segment, the electric field received from the j^{th} segment is

$$E_{bs}^{j} = E_0 r e^{-\alpha \Delta L j} \sum_{m=1}^{M} e^{i\phi_m}, \tag{2.16}$$

where E_0 is the launched electric field and ϕ_m is the phase of the light reflected from the m^{th} scattering center within the j^{th} fiber segment as visualized in Fig. 2.2(a). Assuming uniform reflection and attenuation coefficients for all fiber segments, the optical power received from a given segment is proportional to the absolute square of the backscattered field, yielding

$$P_{bs}^{j} \propto |E_{bs}^{j}|^2 = |E_0|^2 r^2 e^{-2\alpha \Delta L j} \cdot \left[M + 2 \sum_{(m=1)}^{M} \sum_{(m'=m+1)}^{M} \cos(\phi_m - \phi_{m'}) \right]. \tag{2.17}$$

Equation 2.17 should be interpreted as a toy model of the measured Phase-OTDR traces, consisting of a constant offset and an oscillatory term, both of which become exponentially weaker with increasing distance from the launch end. If a local environmental change affects the j^{th} fiber segment, the phase shifts, ϕ_m, experienced by the incident light as it is reflected from each of the M scattering sites will change, causing the measured power to vary [2, 54].

Figure 2.2(a) presents a diagram of a setup used to conduct Phase-OTDR, while Fig. 2.2(b) shows a full Phase-OTDR trace generated using a pulse duration of 10 ns and Fig. 2.2(c) presents three traces for the same fiber segment to illustrate the effect of pulse duration on Phase-OTDR resolution.

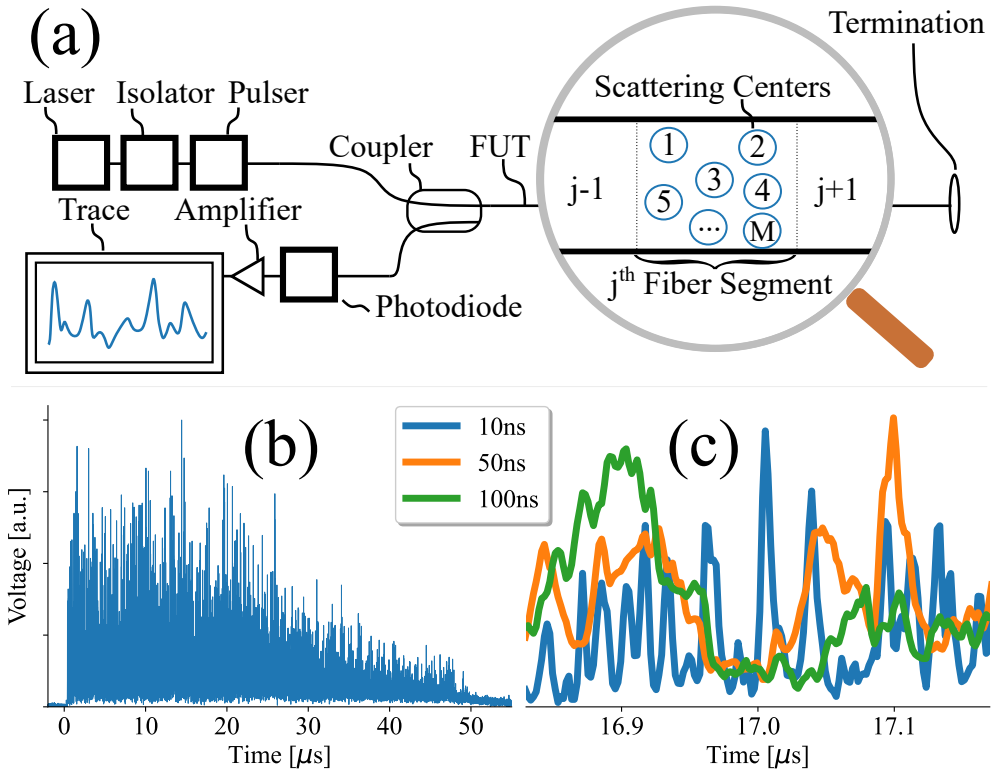

Figure 2.2: (a) Diagram modified from [2] showing a setup used for conducting Phase-OTDR. A laser is pulsed by mechanical, electro-optical or acousto-optical means and sent through a coupler to the fiber under test (FUT), which can be modelled in accordance with Eq. 2.17 as consisting of discrete, concatenated fiber segments containing M scattering centers each. The back-reflected light is passed to a photodiode, where it is detected and displayed on an oscilloscope. (b) Reproduced Phase-OTDR trace created using a setup similar to (a) utilizing pulses with a duration of 10 ns. (c) Comparison of Phase-OTDR traces for the same fiber segment created using pulses with durations of 10 ns, 50 ns, and 100 ns demonstrating increased resolution for shorter pulses.

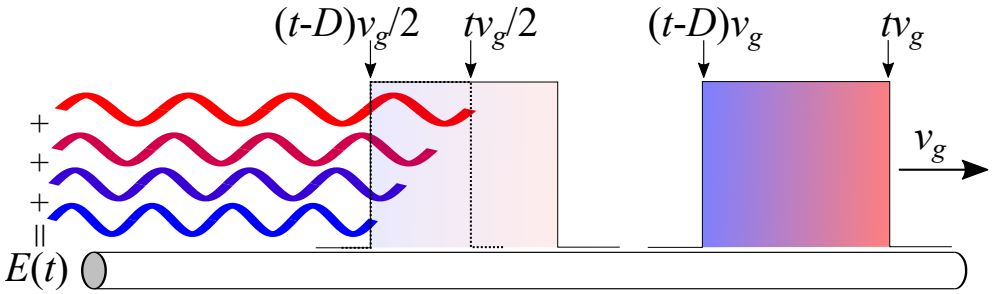

Figure 2.3: Visualization of the working principle of CP-OTDR. At a time, t, after entering a fiber, the front of a chirped pulse is located at $z = tv_g$, while the backscattered electric field at the input consists of frequencies scattered from a width $\Delta z = Dv_g/2$ at a time $t/2$.

2.2.1 Chirped Pulse Phase-OTDR

While the strong dependence on local phase changes provides Phase-OTDR with high sensitivity, the random nature of the phase between scattering centers and the unpredictable way these phases respond to an external perturbation necessitates sophisticated modulation of the pulse or equally advanced demodulation of the detected signal to calibrate the magnitude of the disturbance [55, 56, 57]. Ideally, a linear relationship between the magnitude of the environmental variation and the impact on some property of the Phase-OTDR trace would make calibration of the system easy. Such a linear dependence can be obtained by replacing the monochromatic Phase-OTDR pulses with chirped pulses, where the instantaneous frequency of the optical pulse changes across its duration as originally explained in [3], on which the following derivation is based.

Ignoring attenuation, a chirped pulse with a duration, D, a starting frequency, ν_0, a chirping range, $\Delta\nu_c$, and amplitude E_0 launched at $t = 0$ into a fiber with a refractive index, n, where the light has a group velocity of $v_g = c/n_g$, produces a back-scattered electric field at the fiber input, which can be measured at a time $t > 0$ to be

$$E(t) = \int_{\frac{(t-D)v_g}{2}}^{\frac{tv_g}{2}} E_0 r(Z) \exp\left(i\phi(Z)\right) dZ, \tag{2.18}$$

where $r(Z)$ is the local reflection coefficient and

$$\phi(Z) = 2\pi \int_0^{t-\frac{2Z}{v_g}} \left(\nu_0 + \frac{\Delta\nu_c}{D}\tau\right) d\tau \tag{2.19}$$

$$= 2\pi\nu_0 \left(t - \frac{2Z}{v_g}\right) + 2\pi \frac{\Delta\nu_c}{2D} \left(t - \frac{2Z}{v_g}\right)^2. \tag{2.20}$$

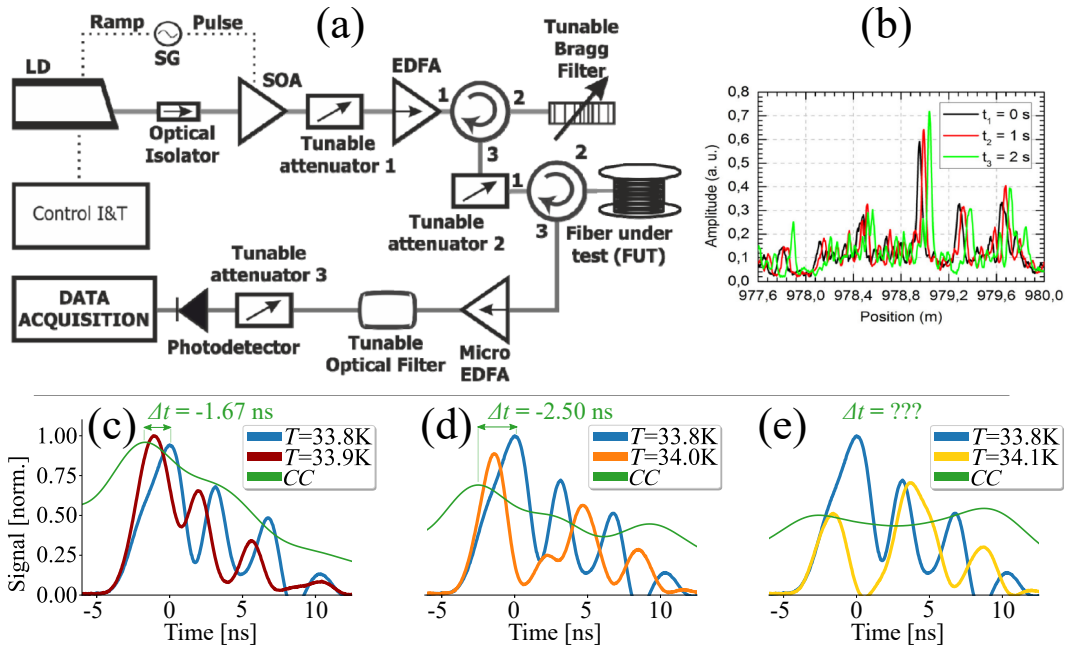

Figure 2.4: (a) Diagram modified from [3] illustrating a setup for conducting CP-OTDR. Chirped pulses generated using a current modulated DFB laser and a triggered solid state optical amplifier are launched into a FUT and the back-reflected signal is detected using a photodiode and a data acquisition system. (b) CP-OTDR interference patterns from [3] collected at three different times for the same fiber segment undergoing a temperature change. (c-e) Comparison of interference patterns measured in the experiment presented in Chapter 6 for the same fiber segment at different temperatures. The normalized cross-correlation reveals the time shift in Eq. 2.26 caused by a temperature change. For large temperature changes, where the underlying assumptions of Eq. 2.26 are no longer valid, the cross-correlation becomes too small for accurate determination of the temperature change from the time shift.

The generation of $E(t)$ in Eq. 2.18 is visualized in Fig. 2.3, where at a time t after entering the fiber, the front of the chirped pulse is located at tv_g, while Fig. 2.4(a) contains an illustration of an experimental setup for conducting CP-OTDR. Using a pulsed, frequency-swept laser, a chirped pulse is generated and launched into a FUT. The backscattered light is detected by a photodiode connected to an oscilloscope. The electric field at the photodiode at a time, t, consists of frequencies that were emitted from a fiber segment of length $Dv_g/2$ at a time $t/2$. To understand how Eq. 2.18 leads to a linear relationship between an applied temperature change and a shift in the detected interference pattern, one can assume that $r(Z) = r_0(\delta(Z - Z_1) + \delta(Z - Z_2))$, implying that only two scattering centers located at Z_1 and Z_2, where $(t - D)v_g/2 < Z_1 < Z_2 < tv_g/2$, contribute to the back-scattered electric field. Using this simplification,

$$\frac{E(t)}{E_0 r_0} = \exp\left(i2\pi\left[\nu_0\left(t - \frac{2Z_1}{v_g}\right) + \frac{\Delta\nu_c}{2D}\left(t - \frac{2Z_1}{v_g}\right)^2\right]\right) + \ldots \exp\left(i2\pi\left[\nu_0\left(t - \frac{2Z_2}{v_g}\right) + \frac{\Delta\nu_c}{2D}\left(t - \frac{2Z_2}{v_g}\right)^2\right]\right). \tag{2.21}$$

Noting that $|\exp(ia) + \exp(ib)|^2 = |2\cos((b-a)/2)|^2$, Eq. 2.21 implies that the measured power is proportional to

$$P(t) \propto \cos^2\left(\pi\left[\nu_0\left(t - \frac{2Z_2}{v_g}\right) + \frac{\Delta\nu_c}{2D}\left(t - \frac{2Z_2}{v_g}\right)^2\right] - \ldots \pi\left[\nu_0\left(t - \frac{2Z_1}{v_g}\right) + \frac{\Delta\nu_c}{2D}\left(t - \frac{2Z_1}{v_g}\right)^2\right]\right). \tag{2.22}$$

Rearranging the terms in Eq. 2.22 yields

$$P(t) \propto \cos^2\left(\pi\frac{2(Z_2 - Z_1)}{v_g}\left[-\nu_0 + \frac{\Delta\nu_c}{D}\left[\frac{Z_2 + Z_1}{v_g} - t\right]\right]\right). \tag{2.23}$$

Defining the optical path difference (OPD) to be $l_0 = n(Z_2 - Z_1)$ implies that a temperature change, ΔT, will alter the refractive index and thus change the OPD by $\Delta l = l_0 K \Delta T$. Temperature changes also affect $Z_2 - Z_1$, but this can be ignored as $(Z_2 - Z_1) \cdot (\partial_T n) \gg n \cdot \partial_T (Z_2 - Z_1)$. The phase term inside the squared cosine function in Eq. 2.23 can now be expressed as

$$\Phi_{2,1}(t) = \pi\frac{2l_0}{c}\left[-\nu_0 + \frac{\Delta\nu_c}{D}\left[\frac{Z_2 + Z_1}{v_g} - t\right]\right]. \tag{2.24}$$

If a small temperature change occurs, the phase at time t will be

$$\Phi'_{2,1}(t) = \pi \frac{2(l_0 + \Delta l)}{c} \left[-\nu_0 + \frac{\Delta \nu_c}{D} \left[\frac{Z_2 + Z_1}{v_g} - t \right] \right]. \tag{2.25}$$

Assuming that the temperature change is sufficiently small, $\Phi'_{2,1}(t)$ will be equal to $\Phi_{2,1}(t + \Delta t)$, implying that the power at a time, t, of the interference pattern after a temperature change occurs will be identical to the power of the interference pattern before the change at a time $t + \Delta t$. In other words, a temperature change will under ideal circumstances effectively shift the interference pattern displayed on the oscilloscope by Δt as shown in Fig. 2.4(b). Setting Eq. 2.24 with $t + \Delta t$ as the argument equal to Eq. 2.25 allows an expression for the time shift in the interference pattern, Δt, caused by a temperature change, ΔT, to be determined. Then, using the approximation $Z_1 \approx Z_2 \approx v_g t/2$ allows the expression for Δt to be written as

$$\Delta t \approx D \frac{\nu_0}{\Delta \nu_c} K \Delta T. \tag{2.26}$$

The time shift Δt between two interference patterns measured before and after a temperature change can be determined by calculating their cross-correlation as illustrated in Fig. 2.4(c). The subfigure shows an interference pattern, I_1, detected from a fiber segment at a temperature of $T_1 = 33.8\text{K}$ and an interference pattern, I_2, from the same segment at a temperature of $T_2 = T_1 + 0.1\text{K} = 33.9\text{K}$. By computing the cross-correlation, CC, between I_1 and I_2 normalized to the largest of their respective maximum auto-correlations, one can determine the time delay, $\Delta t = -1.67\text{ns}$ caused by the temperature change.

The derivation that led to Eq. 2.26 suggests that an applied temperature change will only cause a time shift, but in reality, where more than 2 scattering centers contribute to the interference pattern and where a random phase change sensitive to environmental factors occurs at each center, the shape of the interference pattern will be severely distorted when Δt gets too large, thus making accurate calculation of the correlation difficult. In practice the distortion typically becomes critical when Δt exceeds approximately 10% of the pulse duration.

Figure 2.4(d) shows I_1 along with I_3 corresponding to a temperature of $T_3 = T_1 + 0.2\text{K} = 34.0\text{K}$, where the cross-correlation reveals a time delay of $\Delta t = -2.50\text{ns}$. Note that the larger time shift causes a lower peak value of the cross-correlation compared to Fig. 2.4(c) as the traces become partially decorrelated. In Fig. 2.4(e), where I_1 is compared with I_4 corresponding to $T_4 = T_1 + 0.3\text{K} = 34.1\text{K}$, the correlation is too low for the time shift to be unambiguously determined. The maximum temperature change for which two consecutive measurements remain correlated is referred to as

the "shot-to-shot sensing range". Equation 2.26 implies a trade-off between the shot-to-shot sensing range and the sensitivity, as the former is proportional to $\Delta\nu_c$, while the latter is proportional to $1/\Delta\nu_c$. Thus, high sensitivity with low shot-to-shot sensing range can easily be achieved by lowering the chirping range of the pulse, but achieving low sensitivity with extended shot-to-shot range for detecting sudden, large temperature fluctuations in applications such as monitoring chemical- or nuclear reactors is limited by the ability to generate large chirps.

To generate a chirped optical pulse, a variety of methods summarized in Tab. 2.1 can be used. Pulsing a typical, commercially available frequency-swept tunable laser can produce chirps on the order of 1-10 kHz/ns, while letting monochromatic light through a phase modulator driven with a swept RF electrical signal from a typical, commercially available, legacy function generator affordable for most research groups can provide similar chirps on the order of 1-10 kHz/ns. Note that state of the art (SOTA) function generators can produce maximum chirps on the scale of 0.1-1 GHz/ns, though their unit cost may be prohibitively high for many applications. Using a tunable laser or an RF sweep makes adjusting the chirping rate easy but limits the maximum achievable chirping rate. Alternatively, the current supplied to a DFB laser can be varied over time, changing the carrier density in its gain medium, thereby altering its refractive index and thus the frequency of the emitted light, yielding chirps on the scale of 1-10 MHz/ns. Such an approach allows for a higher chirping rate, but achieving a wide chirping range requires increasingly high currents, which also increase the output power and can cause distortions to the pulse envelope. A different approach launches a short, Gaussian pulse into a dispersive fiber whose length is equal to the dispersion length, $L_{Disp} = D^2/\beta_2$, thereby producing a maximum chirp on the order of $\partial_T(\Delta\nu_c) = 1/(2D^2)$, which for a 1 ns pulse is 500 MHz/ns. Using a passive effect, such as dispersion, ensures good reproducibility of the chirping rate, but prevents its magnitude from being adjusted without altering the duration of the pulse. Launching a Gaussian pulse with a peak power, P_0, into a highly nonlinear fiber allows self-phase modulation (SPM) to produce a maximum chirp of $\partial_T(\Delta\nu_c) = 2\gamma P_0 L/D^2$, which for realistic values of γ =10 $\mathrm{W^{-1}km^{-1}}$, D = 1 ns, P_0 = 1 W and L = 1 km yields a chirp on the order of 5 GHz/ns if dispersion effects and attenuation are neglected. The SPM approach allows for appreciable chirping rates, which can be adjusted by changing P_0, though this also implies that unwanted power fluctuations will alter the chirping rate. Finally, by modifying Eq. 2.8 so the grating period, K, changes linearly with distance, one can create a chirped FBG, where different frequencies are reflected from different positions along the grating [58, 59, 60], causing the wide range of frequencies constituting

Method	Min. Chirp	Max. Chirp	Unit	Source
Tunable laser	1	10	kHz/ns	[61]
RF sweep (legacy)	1	10	kHz/ns	[62]
DFB current ramp	1	10	MHz/ns	[3]
Dispersive fiber	10	500	MHz/ns	[63]
RF sweep (SOTA)	0.1	1	GHz/ns	[64]
SPM	1	10	GHz/ns	[65]
Chirped FBG	0.1	50	THz/ns	[66]

Table 2.1: Summary of typical chirping rate ranges achievable using different methods. For commercially available equipment, datasheets for representative devices are provided.

a short optical pulse to experience a relative time delay. The achievable chirping rate depends on the design of the grating and can reach values on the scale of 50 THz/ns, though this can only be adjusted by manipulating the grating. Whichever method is used for generating chirped optical pulses for a given application, a flexible technique for increasing the chirping rate which does not rely on engineering more sophisticated electronics or fiber structures with special properties would be valuable.

2.3 Polarization sensing

Apart from amplitude, frequency and phase, optical polarization is another property, which can be affected by environmental changes. As the experiments conducted in this thesis involve detecting changes in the optical polarization, a review of the real-, Jones- and Stokes formalisms for describing this property of light is presented. Note that these formalisms were originally developed to describe the polarization of plane, transverse waves propagating in free space, where the electric field vectors are always perpendicular to the direction of propagation. Inside a waveguide, such as an optical fiber, the electric field will have a nonzero component along the propagation axis, but since this component is usually small compared to the transverse components, using these formalisms to describe the polarization of light in a fiber is a valid approximation.

2.3.1 The real electric field

Using the real formalism, the electric field vector, $\boldsymbol{E'}$, for a transverse plane wave wave propagating in the z-direction can be expressed as

$$\boldsymbol{E'} = E_0 \begin{pmatrix} \cos(\theta)\cos(kz - \omega t) \\ \sin(\theta)\cos(kz - \omega t + \phi) \end{pmatrix}, \tag{2.27}$$

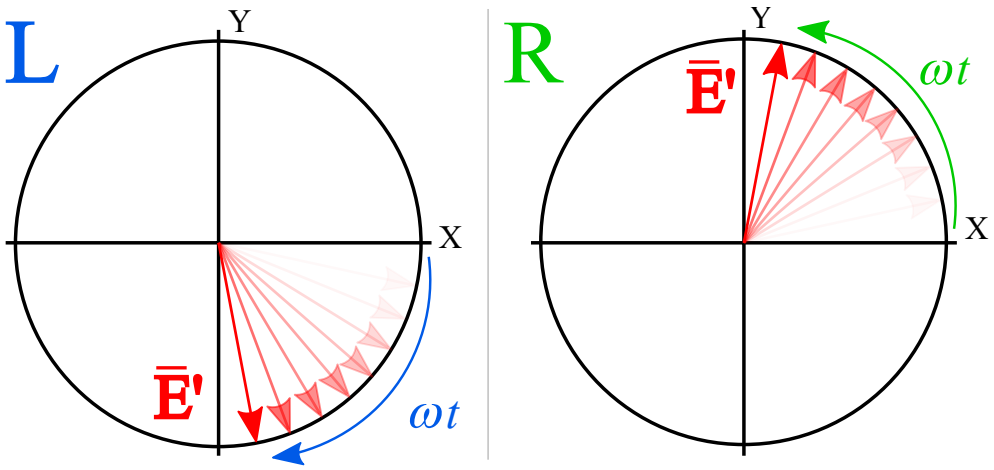

Figure 2.5: Visualization of the definitions of left-hand circular and right-hand circular polarization used in this thesis. Light moving towards the viewer is considered L-polarized if its electric field vector rotates clockwise over time, which happens when $\phi = -\pi/2$ in Eq. 2.27. Similarly, light whose electric field vector rotates counter-clockwise over time, which happens when $\phi = \pi/2$ in Eq. 2.27, is considered R-polarized.

where k is the wave vector, $E_0 \cos(\theta)$ is the amplitude of the field along the x-axis, $E_0 \sin(\theta)$ is the maximum amplitude of the field along the y-axis, ω is the angular frequency, t is the time and ϕ is a phase delay between the x- and y-components of the field. If $\theta = 0°$, the field is polarized along the x-direction, while $\theta = 45°$ and $\phi = 0°$ implies that the field is polarized along the xy diagonal. For $\theta = 45°$ and $\phi = 90°$, the electric field vector at any z location rotates counter-clockwise around the z-axis over time when looking against the direction of propagation and is said to have right-hand circular polarization as visualized in Fig. 2.5. Note that this thesis lets the "handedness" of circular polarization refer to the temporal rotation of the electric field vector at a certain location when looking towards the source, which is the convention used by the Institute of Electrical and Electronics Engineers (IEEE) [67]. Some authors let "handedness" refer to the spatial rotation of the electric field vector around the z-axis at a particular instance in time when looking towards the source [43], in which case the choice of $\phi = 90°$ cause a clockwise spatial rotation.

2.3.2 The Jones formalism

Using Eq. 2.27 has the advantage of providing the exact orientation of the electric field at any time and place, but the disadvantage that mathematically accounting for effects such as the interference between two fields or the impact of phase shifts introduced by various optical components is tedious. Instead, one can perform calculations using

a complex electric field $\boldsymbol{E}$ from which the real field can be recovered according to

$$\boldsymbol{E'} = \mathfrak{Re}\left\{\boldsymbol{E}\right\} \tag{2.28}$$
$$\boldsymbol{E'} = \mathfrak{Re}\left\{E_0 \begin{pmatrix} \cos(\theta) \\ \sin(\theta)\exp(i\phi) \end{pmatrix} \cdot \exp(i(kz-\omega t))\right\}.$$

The complex unit vector, $\boldsymbol{e} = (\cos(\theta), \sin(\theta)\exp(i\phi))^T$, is referred to as the "Jones vector". Furthermore, note that the squared magnitude of the field averaged over one cycle is

$$\langle \boldsymbol{E'}^2 \rangle_T = \langle \mathfrak{Re}\left\{\boldsymbol{E}\right\}^2 \rangle_T = \frac{1}{4}\langle (\boldsymbol{E} + \boldsymbol{E^*})^2 \rangle_T \tag{2.29}$$
$$= \frac{1}{4}\langle \boldsymbol{E}^2 + \boldsymbol{E}^{*2} + 2|\boldsymbol{E}|^2 \rangle_T = \frac{1}{2}\langle |\boldsymbol{E}|^2 \rangle_T = \frac{1}{2}|\boldsymbol{E}|^2, \tag{2.30}$$

which shows that the absolute square of the complex electric field is twice the squared magnitude of the real field averaged over one optical cycle. Because optical sensors such as photodiodes effectively respond to the power of the incident field averaged over many optical cycles, the ability to compute the average power with the multiplication of two complex numbers instead of an integral is another advantage of the Jones formalism. Additionally, two complex electric fields, $\boldsymbol{E_1}$ and $\boldsymbol{E_2}$, are orthogonal if

$$\boldsymbol{E_1}^* \cdot \boldsymbol{E_2} = 0 \tag{2.31}$$

2.3.3 The Stokes formalism

The Jones formalism expresses the polarization of light in terms of the electric field amplitudes along the x- and y-directions as well as their relative phase. However, measurements of optical polarization do not detect the electric field but rather the average power of the field along a particular axis. Furthermore, the Jones formalism cannot model cases where changes in the state of polarization (SOP) occur on a time scale shorter than the response time of the equipment, in which case the light will appear depolarized. To quantify the polarization of light in terms of optical power, the Stokes vector can be introduced,

$$\hat{S}' = \begin{pmatrix} S'_0 \\ S'_1 \\ S'_2 \\ S'_3 \end{pmatrix} = \begin{pmatrix} |E_X|^2 + |E_Y|^2 \\ |E_X|^2 - |E_Y|^2 \\ |E_D|^2 - |E_A|^2 \\ |E_R|^2 - |E_L|^2 \end{pmatrix} = \begin{pmatrix} |E_X|^2 + |E_Y|^2 \\ |E_X|^2 - |E_Y|^2 \\ 2\mathfrak{Re}(E_x E_y^*) \\ -2\mathfrak{Im}(E_x E_y^*) \end{pmatrix}. \tag{2.32}$$

The entry, S_0' is proportional to the total power of the light, while S_1' encodes the difference in the power of the electric field when projected onto the x- and y-axes. Similarly, S_2' encodes the power difference when the field is projected onto the $+45°$ diagonal (D) and the $-45°$ anti-diagonal (A). Finally, S_3' encodes the difference in power between the right-hand circular field component (R) and the left-hand circular field component (L). It can be shown that

$$S_0'^2 \geq S_1'^2 + S_2'^2 + S_3'^2. \tag{2.33}$$

Because Eq. 2.33 is equivalent to the equation defining a solid ball with a radius, S_0', the SOP of a laser can be represented on the so-called "Poincaré sphere" [68] as visualized in Fig. 2.6. The equality in Eq. 2.33 holds for purely polarized light, while the inequality holds for depolarized light, where changes in the SOP occur faster than the detection equipment can measure. The experiments conducted in this thesis involve purely polarized light, which allows a normalized Stokes vector, $\hat{S} = \hat{S}'/S_0'$, to be expressed in terms of the parameters θ and ϕ from the Jones formalism according to

$$\hat{S} = \begin{pmatrix} S_1 \\ S_2 \\ S_3 \end{pmatrix} = \begin{pmatrix} (|E_X|^2 - |E_Y|^2)/S_0' \\ (|E_D|^2 - |E_A|^2)/S_0' \\ (|E_R|^2 - |E_L|^2)/S_0' \end{pmatrix} = \begin{pmatrix} \cos(2\theta) \\ \sin(2\theta)\cos(\phi) \\ \sin(2\theta)\sin(\phi) \end{pmatrix}, \tag{2.34}$$

where $1 = S_1^2 + S_2^2 + S_3^2$, which is the equation for points located on the surface of the Poincaré sphere.

2.3.4 Conventional measurement of Stokes vector

To determine the SOP of a laser in the Stokes formalism, the powers of each polarization component must be measured. Expressing the complex electric field amplitude as

$$\boldsymbol{A} = \boldsymbol{E} \cdot \exp(-i(kz - \omega t)) = E_0 \boldsymbol{e} = E_0 \begin{pmatrix} \cos(\theta) \\ \sin(\theta)\exp(i\phi) \end{pmatrix}, \tag{2.35}$$

the Stokes vector of a laser beam can be determined by launching the light into the four configurations of polarizers and waveplates presented in Fig. 2.7 in parallel. The configuration in Figs. 2.7(a) extracts the electric field component parallel to the x-direction using a polarizer and detects the power,

$$P_1 \propto |E_X|^2 = \left| \begin{pmatrix} 1 & 0 \\ 0 & 0 \end{pmatrix} \boldsymbol{A} \right|^2 = |E_0|^2 \cos^2(\theta) \tag{2.36}$$

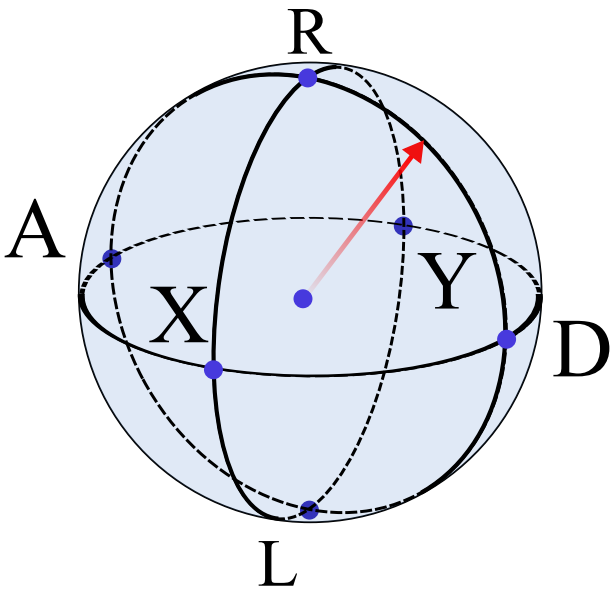

Figure 2.6: Illustration of the Poincaré sphere, which encodes the possible SOPs of a laser. Note that two SOPs, which are orthogonal according to Eq. 2.31, correspond to points on the sphere separated by 180°.

using a photodiode, while the configuration labelled (b) does the same thing for the y-direction to detects P_2,

$$P_2 \propto |E_Y|^2 = \left| \begin{pmatrix} 0 & 0 \\ 0 & 1 \end{pmatrix} \boldsymbol{A} \right|^2 = |E_0|^2 \sin^2(\theta). \tag{2.37}$$

The stokes components S_0' and S_1' can then be determined from $S_0' = P_1 + P_2 \propto |E_0|^2$ and $S_1' = P_1 - P_2 \propto |E_0|^2 \cos(2\theta)$. Similarly, the configuration labelled (c) has a polarizer aligned with the +45° diagonal, yielding

$$P_3 \propto |E_D|^2 = \left| \frac{1}{2} \begin{pmatrix} 1 & 1 \\ 1 & 1 \end{pmatrix} \boldsymbol{A} \right|^2 = \frac{1}{2} |E_0|^2 (1 + \sin(2\theta)\cos(\phi)), \tag{2.38}$$

allowing S_2' to be calculated from $S_2' = 2P_3 - S_0' \propto |E_0|^2 \sin(2\theta)\cos(\phi)$. Finally the configuration labelled (d) introduces a $-\pi/2$ phase shift between the x- and y-components of the electric field using a quarterwave plate, which in effect makes the E_D component of the field after the plate proportional to E_R before the plate. The power of the E_D component, P_4, is then detected and S_3' is calculated from

$S_3' = 2P_4 - S_0' \propto |E_0|^2 \sin(2\theta)\sin(\phi)$. In summary,

$$\hat{S}' = \begin{pmatrix} S_0' \\ S_1' \\ S_2' \\ S_3' \end{pmatrix} = \begin{pmatrix} P_1 + P_2 \\ P_1 - P_2 \\ 2P_3 - (P_1 + P_2) \\ 2P_4 - (P_1 + P_2) \end{pmatrix}. \tag{2.39}$$

2.3.5 Polarimetric sensing

Conventional approaches to fiber optical polarimetric sensing shine light from the sensing fiber onto a polarizer, causing the detected power to follow Eq. 2.36, which is also referred to as "Malus' law" [69]. The formula, $P_{\text{measured}} = P_{\max}\cos^2(\theta)$, relates changes in the SOP to changes in measured optical power. Taking the derivative with respect to θ yields $dP_{\text{measured}}/d\theta = -2P_{\max}\sin(2\theta)$, showing that maximum sensitivity to small variations is achieved when $\theta = 45°$. In applications such as fusion reactor monitoring [70], detecting small variations in optical polarization caused by changing magnetic fields is crucial, making enhanced sensitivity desirable. The ability to increase sensitivity by boosting the optical power is limited by the onset of nonlinear effects in the sensing fiber and the cost of amplifiers and filters before the polarizer. Alternatively, one can devise a nonlinear measurement scheme, where the measured power is proportional to a function of θ, which is more sensitive to changes in the polarization angle than $\cos^2(\theta)$.

2.3.6 Polarimetry

To determine the SOP of a laser, an experimental setup similar to the one presented in Fig. 2.7 is required. Essentially, the orientations of the electric field of the laser must be measured relative to fixed waveplates and polarizers. When comparing the SOPs of two lasers using the conventional, polarizer-based approach, they must either be directed into the same polarimeter in turn, or into two separate polarimeters measuring in parallel. Instead of relying on physical polarizers, a signal processing scheme could be devised, where the SOPs of the lasers are compared to each other directly.

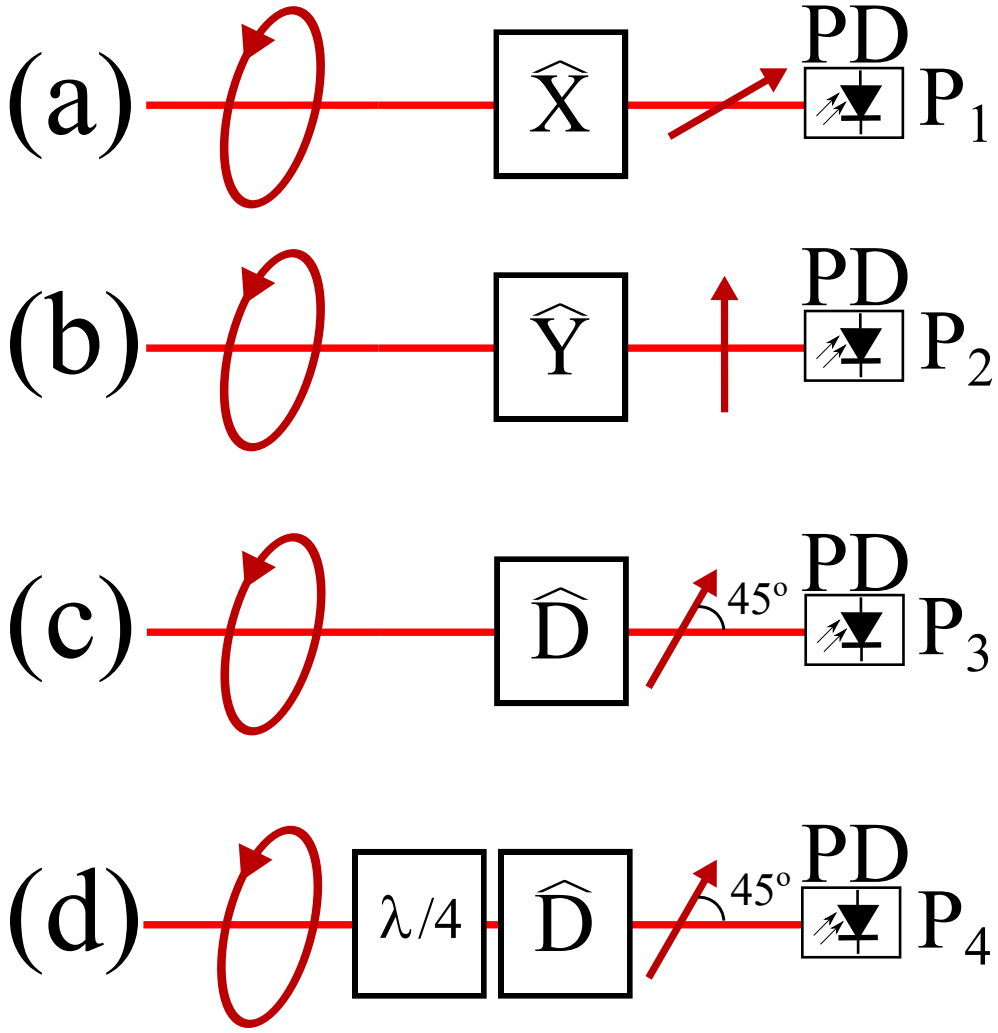

Figure 2.7: (a-d) Configurations of polarizers and waveplates needed to measure four optical powers from which the Stokes vector of the incident light can be determined. (a) A polarizer along the x-direction enables the measurement of $P_1 \propto |E_X|^2$. (b) A polarizer along the y-direction enables the measurement of $P_2 \propto |E_Y|^2$. (c) A polarizer aligned with the $+45°$ diagonal enables the measurement of $P_3 \propto P_D$ from which the Stokes parameter S_2' can be calculated. (d) After a quarter wave plate, which introduces a phase shift of $-\pi/2$ between the X and Y components of the incident field, the field strength along the $+45°$ diagonal is proportional to E_R of the incident field. A polarizer aligned with the $+45°$ diagonal then enables the measurement of $P_4 \propto |E_R|^2$.

Chapter 3

Nonlinear Optics Theory

Weak electromagnetic waves passing through glass will have their phases and amplitudes modified in a way that only depends on the characteristics of the glass as well as the frequency and polarization of the light. Slightly increasing the amplitude of the waves simply yields additional light with the same altered characteristics but does not change the way they are modified. Such behavior is called "linear", because the output obtained by launching two waves of light into the medium simultaneously is identical to the one acquired by launching them into the medium individually and subsequently adding up the outputs. However, this is no longer the case if the light waves are coherent and their combined electric fields are large enough to constitute a significant fraction of the field binding electrons in the glass molecules to their nuclei. Intense fields modify the refractive index of the material in which they propagate, which in turn alters the properties of the propagating light. Such intensity dependent effects are called "nonlinear" because they prevent two lightwaves propagating through the medium independently from producing the same result as two lightwaves propagating simultaneously. Therefore, nonlinear effects can dramatically change the properties of light propagating in glass, for example by generating new colors from otherwise monochromatic optical inputs.

This chapter explains how the behavior of light subject to nonlinear effects in optical fibers can be modelled starting from Maxwell's equations. By assuming an off-resonant, sinusoidal electric field, which is intense enough for the lowest order nonlinearity of the medium to be significant, the nonlinear Schrödinger equation (NLSE), describing how electric fields propagate in the fiber subject to dispersion, attenuation and non-linearities associated with power dependent changes in the refractive index of glass is derived. Methods for solving the equation numerically are discussed and an analytical solution for the special case of scalar fields consisting of two frequencies experiencing no dispersion or attenuation is presented. Finally, a vectorial version

of the scalar model is derived and its implications for environmental sensing are discussed.

3.1 From Maxwell's equations to the NLSE

The NLSE was first derived heuristically in [71] for optical beams propagating in bulk glass, while the derivation from first principles for an optical fiber waveguide presented in this section follows the one in [72]. The behavior of electromagnetic fields is governed by Maxwell's equations,

$$\nabla \times \boldsymbol{E} = -\partial_t \boldsymbol{B} \tag{3.1}$$

$$\nabla \times (\boldsymbol{B}/\mu_0 - \boldsymbol{M}) = \boldsymbol{J} + \partial_t \left(\epsilon_0 \boldsymbol{E} + \boldsymbol{P}\right) \tag{3.2}$$

$$\nabla \cdot (\epsilon_0 \boldsymbol{E} + \boldsymbol{P}) = \rho_f \tag{3.3}$$

$$\nabla \cdot \boldsymbol{B} = 0, \tag{3.4}$$

where $\boldsymbol{E}$ is the electric field, $\boldsymbol{B}$ is the magnetic field, $\boldsymbol{M}$ is the magnetization, $\boldsymbol{J}$ is the current density, $\boldsymbol{P}$ is the polarization of the material, ρ_f is the free charge density, μ_0 is the vacuum permeability and ϵ_0 is the vacuum permittivity. The operator, ∂_t, is the time derivative, while $(\nabla\times)$ yields the curl of the vector field and $(\nabla\cdot)$ yields its divergence. Optical fibers are made from dielectrics, such as glass or plastic, and therefore have no magnetization, currents or free charges,

$$\nabla \times \boldsymbol{E} = -\partial_t \boldsymbol{B} \tag{3.5}$$

$$\nabla \times \boldsymbol{B}/\mu_0 = \partial_t \left(\epsilon_0 \boldsymbol{E} + \boldsymbol{P}\right) \tag{3.6}$$

$$\nabla \cdot (\epsilon_0 \boldsymbol{E} + \boldsymbol{P}) = 0 \tag{3.7}$$

$$\nabla \cdot \boldsymbol{B} = 0, \tag{3.8}$$

Taking the curl of the first equation, substituting in the second equation, exploiting the identity, $\nabla \times \nabla \times \boldsymbol{F} = \nabla(\nabla \cdot \boldsymbol{F}) - \nabla^2 \boldsymbol{F}$ and that $\nabla \cdot \boldsymbol{E} = 0$ in a region without free charges yields

$$\nabla \times \nabla \times \boldsymbol{E} = -\partial_t \nabla \times \boldsymbol{B} \tag{3.9}$$

$$-\nabla^2 \boldsymbol{E} = -\partial_t^2 \left(c^{-2} \boldsymbol{E} + \mu_0 \boldsymbol{P}\right), \tag{3.10}$$

where $c = (\epsilon_0 \mu_0)^{-1/2}$ is the speed of light in vacuum. Rearranging yields

$$\nabla^2 \boldsymbol{E} - c^{-2} \partial_t^2 \boldsymbol{E} = \mu_0 \partial_t^2 \boldsymbol{P}. \tag{3.11}$$

The vector field $\boldsymbol{P}$ encodes how the dielectric material responds to the applied electric field, which for sinusoidal electric field far from any resonance in the material can be expressed as $\boldsymbol{P} = \epsilon_0 \left(\chi^{(1)}\boldsymbol{E} + \chi^{(2)} : \boldsymbol{EE} + \chi^{(3)} : \boldsymbol{EEE} + ...\right)$, where $\chi^{(n)}$ is the n^{th} order susceptibility tensor and the operator, " : ", is the tensor product. As detailed in [73], for centrosymmetric silica fibers, whose crystal structures are amorpheous, symmetry considerations ensure that $\chi^{(2)} = 0$. Furthermore, using electric fields that are small but non-negligible compared to the ones binding electrons in the material to the atoms in the lattice ensures that terms higher than $n = 3$ can be neglected. Using these simplifying assumptions for the material polarization, it can be expressed as $\boldsymbol{P} = \boldsymbol{P}_L + \boldsymbol{P}_{NL}$ where

$$\boldsymbol{P}_L = \epsilon_0 \int_{-\infty}^{t} \chi^{(1)}(t - t')\boldsymbol{E}(\boldsymbol{r}, t)dt' \tag{3.12}$$

is the linear response to the applied electric field and

$$\boldsymbol{P}_{NL} = \epsilon_0 \int_{-\infty}^{t}\int_{-\infty}^{t}\int_{-\infty}^{t} \chi^{(3)}(t - t_1, t - t_2, t - t_3) : \boldsymbol{E}(\boldsymbol{r}, t_1)\boldsymbol{E}(\boldsymbol{r}, t_2)\boldsymbol{E}(\boldsymbol{r}, t_3)dt_1dt_2dt_3, \tag{3.13}$$

is the nonlinear response.

3.1.1 The transverse mode

To determine the transverse electric field, the nonlinear contribution is neglected and the Fourier transform is taken on both sides of Eq. 3.11, which yields the Helmholtz equation

$$\nabla^2\tilde{\boldsymbol{E}}(\boldsymbol{r}, \omega) = -\epsilon(\omega)\frac{\omega^2}{c^2}\tilde{\boldsymbol{E}}(\boldsymbol{r}, \omega), \tag{3.14}$$

where $\epsilon(\omega) = 1 + \tilde{\chi}^{(1)}(\omega)$ is the permeability of the material and

$$\tilde{\boldsymbol{E}}(\boldsymbol{r}, \omega) = \int_{-\infty}^{\infty} \boldsymbol{E}(\boldsymbol{r}, t) \exp(i\omega t)\, dt. \tag{3.15}$$

The permeability of the material can be expressed as $\epsilon(\omega) = (n(\omega) + i\alpha(\omega)c/2\omega)^2$ where $n(\omega)$ is the refractive index and $\alpha(\omega)$ is the attenuation coefficient for the power of the field. Neglecting the attenuation allows Eq. 3.14 to be written as

$$\nabla^2\tilde{\boldsymbol{E}}(\boldsymbol{r}, \omega) + n^2(\omega)\frac{\omega^2}{c^2}\tilde{\boldsymbol{E}}(\boldsymbol{r}, \omega) = 0, \tag{3.16}$$

which is identical to Eq. 2.3 without the periodic perturbation of the refractive index. Because the change in the refractive index due to nonlinear effects is small compared

to the linear refractive index, the propagation constant, $\beta(\omega)$, calculated from Eq. 2.5 remains valid in the present case.

3.1.2 Pulse evolution

Assuming that the frequency bandwidths of the fields inside the fiber are much smaller than the carrier frequency, ω_0, the real electric field, real linear polarization and real nonlinear polarization can be expressed as products of a slowly varying envelope and a quickly varying complex exponential,

$$\boldsymbol{E'}(\boldsymbol{r},t) = \frac{1}{2}\hat{x}[E(\boldsymbol{r},t)\exp(-i\omega_0 t) + c.c.] \tag{3.17}$$

$$\boldsymbol{P'_L}(\boldsymbol{r},t) = \frac{1}{2}\hat{x}[P_L(\boldsymbol{r},t)\exp(-i\omega_0 t) + c.c.] \tag{3.18}$$

$$\boldsymbol{P'_{NL}}(\boldsymbol{r},t) = \frac{1}{2}\hat{x}[P_{NL}(\boldsymbol{r},t)\exp(-i\omega_0 t) + c.c.]. \tag{3.19}$$

The prime symbol associated with these three fields indicates that they are purely real and distinguishes them from the unprimed fields, which are complex. For simplicity, it is assumed that all three fields remain polarized along the $\hat{x}$ direction. Substituting these expressions into Eq. 3.12 and Eq. 3.13 under the assumption that $\chi^{(3)}$ responds instantly to changes in the applied field implies that $P_{NL}(\boldsymbol{r},t) = 3\epsilon_0\chi^{(3)}_{xxxx}|E(\boldsymbol{r},t)|^2E(\boldsymbol{r},t)/4$, where $\chi^{(3)}_{xxxx}$ is the tensor component that governs the response of the material to applied electric fields that are all oriented in the x-direction. Because $|E(\boldsymbol{r},t)|^2$, which according to Eq. 2.29 is proportional to the time-averaged power of the electric field, varies slowly compared to ω_0, it can be shown that $\tilde{E}(\boldsymbol{r},\omega)$, which is the Fourier transform of the electric field, solves the Helmholtz equation,

$$\nabla^2\tilde{E}(\boldsymbol{r},\omega) + \epsilon(\omega)\frac{\omega^2}{c^2}\tilde{E}(\boldsymbol{r},\omega) = 0, \tag{3.20}$$

where the electric permittivity, $\epsilon(\omega)$, will depend on $|E(\boldsymbol{r},t)|^2$ according to the formula $\epsilon(\omega) = 1 + \tilde{\chi}^{(1)}(\omega) + 3\chi^{(3)}_{xxxx}|E(\boldsymbol{r},t)|^2/4 = (\tilde{n}(\omega) + i\alpha(\omega)c/2\omega)^2$. Here, $\tilde{n}(\omega) = n(\omega) + 3\Re(\chi^{(3)}_{xxxx})|E(\boldsymbol{r},t)|^2/8n(\omega)$ is the total refractive index, which depends on the absolute square of the electric field through the real part of the third order susceptibility. To reiterate, including the time-dependent quantity, $|E(\boldsymbol{r},t)|^2$, in the expression for $\epsilon(\omega)$, which is represented in the frequency domain, is a justified approximation because $|E(\boldsymbol{r},t)|^2$ is assumed to vary so slowly compared to ω_0 that it can be considered constant. When comparing the nonlinearity of different materials, it is customary to refer to the nonlinear refractive index, $n_2 = 3\Re(\chi^{(3)}_{xxxx})/4\epsilon_0 n^2(\omega)c$. The imaginary part of the third order susceptibility, which governs intensity dependent absorption

is ignored as it is typically negligible compared to the linear attenuation coefficient, $\alpha(\omega)$. Using these definitions, Eq. 3.20 can be solved using the ansatz,

$$\tilde{E}(\boldsymbol{r}, \omega - \omega_0) = G(x, y)\tilde{A}(z, \omega - \omega_0)\exp(i\beta_0 z), \tag{3.21}$$

producing separate differential equations for the transverse and longitudinal parts of the field:

$$\left[\partial_x^2 + \partial_y^2 + \partial_z^2\right]\tilde{E} = -\epsilon(\omega)\frac{\omega^2}{c^2}\tilde{E} \tag{3.22}$$

$$\left[\partial_x^2 + \partial_y^2 + \partial_z^2\right]GA\exp(i\beta_0 z) = -\epsilon(\omega)\frac{\omega^2}{c^2}GA\exp(i\beta_0 z) \tag{3.23}$$

$$A\exp(i\beta_0 z)\left[\partial_x^2 G + \partial_y^2 G\right] + G\partial_z^2\left[A\exp(i\beta_0 z)\right] = -\epsilon(\omega)\frac{\omega^2}{c^2}GA\exp(i\beta_0 z) \tag{3.24}$$

$$-A^{-1}\exp(-i\beta_0 z)\partial_z^2\left[A\exp(i\beta_0 z)\right] = G^{-1}\left[\partial_x^2 G + \partial_y^2 G\right] + \epsilon(\omega)\frac{\omega^2}{c^2}. \tag{3.25}$$

The left hand side of Eq. 3.25 only depends on z, while the right hand side only depends on x and y. Because the equality must be satisfied regardless of how the three spatial coordinates are varied, both sides must be equal to the same constant, which for convenience will be labelled as $\tilde{\beta}^2$. Because the expression on the left hand side is equal to $\tilde{\beta}^2$, its solution can be found from

$$-A^{-1}\exp(-i\beta_0 z)\partial_z^2\left[A\exp(i\beta_0 z)\right] = \tilde{\beta}^2 \tag{3.26}$$

$$\partial_z^2\left[A\exp(i\beta_0 z)\right] = -A\exp(i\beta_0 z)\tilde{\beta}^2 \tag{3.27}$$

$$\left[\partial_z^2 A + 2i\beta_0\partial_z A - \beta_0^2 A\right] = -A\tilde{\beta}^2. \tag{3.28}$$

By assuming that spatial variations in the envelope, A, of the electric field of the light occur over distances much larger than the wavelength of that light in the medium, the term $\partial_z^2 A$ in Eq. 3.28 can be neglected, leading to the following set of differential equations,

$$\partial_x^2 G + \partial_y^2 G + [\epsilon(\omega)\omega^2/c^2 - \tilde{\beta}^2]G = 0 \tag{3.29}$$

$$2i\beta_0\partial_z\tilde{A} + (\tilde{\beta}^2 - \beta_0^2)\tilde{A} = 0. \tag{3.30}$$

Here, $\tilde{\beta}$ is the propagation constant of the field obtained by treating the non-linearity as a perturbation and solving Eq. 3.29 to obtain $\tilde{\beta} = \beta(\omega) + \Delta\beta(\omega)$, where $\beta(\omega)$ is the propagation constant obatined from Eq. 2.5 and $\Delta\beta(\omega)$ is the change to the propagation constant due to the nonlinear perturbation. Exploiting that $(\tilde{\beta}^2 - \beta_0^2) \approx$

$2\beta_0(\tilde{\beta} - \beta_0)$, Eq. 3.30 yields

$$\partial_z \tilde{A} = i[\beta(\omega) + \Delta\beta(\omega) - \beta_0]\tilde{A}. \tag{3.31}$$

Both $\beta(\omega)$ and $\Delta\beta(\omega)$ are highly nontrivial functions of the angular frequency of the light in the fiber, but one can expand them in a Taylor series around the carrier frequency to obtain

$$\beta(\omega) = \quad \beta_0 + \quad \beta_1(\omega - \omega_0) + \frac{\beta_2}{2}(\omega - \omega_0)^2 + ... \tag{3.32}$$

$$\Delta\beta(\omega) = \Delta\beta_0 + \Delta\beta_1(\omega - \omega_0) + \frac{\Delta\beta_2}{2}(\omega - \omega_0)^2 + ... \tag{3.33}$$

Terms in Eq. 3.32 of higher order than 2 can typically be neglected for pulses that satisfy the slowly varying envelope approximation. Furthermore, because the perturbation is small, one can approximate $\Delta\beta \approx \Delta\beta_0$ and express Eq. 3.31 as

$$\partial_z \tilde{A} = i\left[\beta_1(\omega - \omega_0) + \frac{\beta_2}{2}(\omega - \omega_0)^2 + \Delta\beta_0\right]\tilde{A}. \tag{3.34}$$

Taking the inverse Fourier transform of Eq. 3.34 replaces factors of $\omega - \omega_0$ with the operator $i\partial_t$ and yields

$$\partial_z A + \beta_1 \partial_t A + i\frac{\beta_2}{2}\partial_t^2 A = i\Delta\beta_0 A. \tag{3.35}$$

Because $\Delta\beta_0 = i\alpha/2 + \gamma|A|^2$, where $\gamma = \omega_0 n_2/cA_{eff}$ and A_{eff} is the effective cross-sectional area of the mode, Eq. 3.35 becomes

$$\partial_z A + \beta_1 \partial_t A + i\frac{\beta_2}{2}\partial_t^2 A + \frac{\alpha}{2}A = i\gamma|A|^2 A. \tag{3.36}$$

The shifted time variable, $T = t - \beta_1 z$, where $v_g = 1/\beta_1$ is the group velocity of the light, measures time relative to the arrival time at a distance of z for a pulse with a carrier frequency of ω_0. Replacing t by T in Eq. 3.36 and exploiting that $\partial_z A(z, T(z)) = \partial_z A + (\partial_z T)\partial_T A = \partial_z A - \beta_1 \partial_T A$ yields the nonlinear Schrödinger equation,

$$\partial_z A + i\frac{\beta_2}{2}\partial_T^2 A + \frac{\alpha}{2}A = i\gamma|A|^2 A, \tag{3.37}$$

which shows how the phase and envelope of a pulse of light is altered by dispersion, attenuation and third order nonlinear effects as it propagates through an optical fiber. Apart from switching around the dependence on time and position, Eq. 3.37 is mathematically identical to the one dimensional version of the Schrödinger equation [74] describing non-relativistic quantum mechanical particles. More precisely, the nonlin-

ear term, $i\gamma|A|^2A$, makes Eq. 3.37 equivalent to the Gross-Pitaevskii equation [75, 76], which describes the behavior of ultra-cold bosons subject to self-interaction.

Note that multiple simplifications and approximations were introduced to derive Eq. 3.37. While more general versions taking multi-mode propagation, higher order dispersion and Raman effects into account can be derived, Eq. 3.37 suffices for the purpose of this thesis.

3.2 The Split-Step Fourier Method

Given an initial field $A(z = 0, T)$ and values of β_2, α and γ, the output field at the end of the fiber, $A(z = L, T)$, can be calculated by numerically solving Eq. 3.37 using the Split-Step Fourier Method (SSFM) [77]. Ignoring the attenuation, α, Eq. 3.37 contains a term accounting for dispersion and a nonlinear term. In the frequency domain, Eq. 3.34 without the nonlinearity implies that the effect of the dispersion term is to multiply the frequency components of the pulse by a complex exponential, thus imparting a phase shift proportional to the propagation distance and the square of the frequency separation from the carrier, without altering the amplitude of individual frequencies. Similarly, Eq. 3.37 without the dispersive term implies that the effect of the nonlinear term is to multiply the field at each instant by a complex exponential, whose phase is proportional to the propagation distance and the local pulse power, while leaving the envelope unaffected. In an actual fiber, the dispersive and nonlinear effects act upon the field simultaneously, changing the envelope as well as the spectrum of the pulse at the same time as z increases. However, if a fiber of length, L, is divided into a sufficiently large number of small segments of length, Δz, one can assume that the dispersion and the nonlinearity are applied sequentially and independently [72]. In this case, one can propagate the pulse forward by Δz by first applying the nonlinearity in the time domain via multiplication with a complex exponential, and then applying the Fast Fourier Transform (FFT) algorithm to obtain the pulse spectrum. Subsequently, applying the dispersion through multiplication by another complex exponential, computing the inverse FFT to return to the time domain yields

$$A(z + \Delta z, T) = \mathfrak{F}^{-1}\left\{\exp\left(i\frac{\beta_2}{2}(\omega - \omega_0)^2\Delta z\right)\mathfrak{F}\left\{\exp(i\gamma|A(z,T)|^2\Delta z)A(z,T)\right\}\right\}. \tag{3.38}$$

Using Eq. 3.38, the task of numerically solving the nonlinear differential equation in Eq. 3.37 given $A(z = 0, T)$, which would otherwise involve adaptive step-size algorithms, is replaced with the tasks of computing the FTT and multiplying by

complex exponentials. Using the SSFM, the field at the end of the fiber can be obtained with good accuracy and a significant speed-up compared to other numerical methods [78]. Additional terms accounting for higher order dispersive- and nonlinear effects can be introduced to simulate their impact on the propagation of optical pulses. Furthermore, the scalar model represented by Eq. 3.38 can be extended to include the effects of optical polarization by introducing separate equations for A_x and A_y as well as terms accounting for their interaction. For example, the effect of randomly varying birefringence in the fiber, which alters the SOP of the light as z increases, can be modelled by applying a complex rotation matrix to the field after every step [79],

$$\begin{pmatrix} A'_x \\ A'_y \end{pmatrix} = \begin{pmatrix} \cos(\theta') & \sin(\theta)\exp(i\phi') \\ -\sin(\theta')\exp(-i\phi') & \cos(\theta') \end{pmatrix} \begin{pmatrix} A_x \\ A_y \end{pmatrix}. \tag{3.39}$$

Here, $-\pi \leq \theta' \leq \pi$ and $-\pi/2 \leq \phi' \leq \pi/2$ are angles chosen randomly at each step to simulate the impact of random birefringence on the polarization of the field, while A'_x and A'_y are the new field components after the rotation matrix is applied.

As part of the work done in this thesis, an implementation of the Split-Step Fourier method, which can take polarization and randomly varying birefringence into account was written from scratch in python [4] with inspiration from the scalar MATLAB implementation presented in [80]. The python code was applied to verify experimental results and analytical calculations in the papers presented in Chapter 6 and Chapter 7.

3.3 Scalar solution of the NLSE

Solving Eq. 3.37 numerically using the SSFM implies a trade-off between speed and accuracy. For a fixed fiber length, increasing the number of steps enhances accuracy but performing a larger number of steps increases computation time. Using numerical methods to model the propagation of a field through a fiber has the disadvantage that the impact of each simulation parameter on the output field is not immediately obvious and can only be determined by running the simulation multiple times using different values. Fortunately, certain special cases allow for analytical solutions to Eq. 3.37, which are computationally simple to evaluate and provide direct physical insight. This thesis is concerned with such an analytically solvable case first treated in [81], where two frequencies of light are launched into a highly nonlinear fiber with negligible dispersion. The analysis begins by choosing $\beta_2 = 0$ and $\alpha = 0$ in Eq. 3.37,

noting that $\partial_z |A(z,T)|^2 = 0$ and solving the resulting differential equation,

$$\partial_z A = i\gamma |A|^2 A \tag{3.40}$$

$$A(z) = A(0)\exp(i\gamma |A|^2 z) \tag{3.41}$$

$$A_{out} = A_{in}\exp(i\gamma L|A|^2), \tag{3.42}$$

where $A(z = L) = A_{out}$ and $A(z = 0) = A_{in}$. Next, a field with two angular frequency components labelled with subscripts r and s spaced ω_d apart and having amplitudes of $\sqrt{P_r}$ and $\sqrt{P_s}$ is defined by

$$A_{in} = \sqrt{P_r}\exp(-0.5\omega_d t) + \sqrt{P_s}\exp(0.5\omega_d t). \tag{3.43}$$

The power of the field is $|A|^2 = |A_{in}|^2 = P_r + P_s + 2\sqrt{P_r P_s}\cos(\omega_d t)$, which is substituted into Eq. 3.42, yielding

$$A_{out} = A_{in}\exp(i\gamma L(P_r + P_s))\exp(i2\gamma L\sqrt{P_r P_s}\cos(\omega_d t)). \tag{3.44}$$

Defining $Q = \exp(i\gamma L(P_r + P_s))$ and $\phi'_{NL} = 2\gamma L\sqrt{P_r P_s}$ produces the expression

$$A_{out} = QA_{in}\exp(i\phi'_{NL}\cos(\omega_d t)). \tag{3.45}$$

A sinusoidally varying function inside a complex exponential can be expressed as an infinite sum of frequency sidebands using the Jacobi-Anger expansion [82],

$$\exp(iM\cos(\Omega t)) = \sum_{n=-\infty}^{\infty} i^n J_n(M)\exp(in\Omega t), \tag{3.46}$$

where J_n is the n^{th} order Bessel function of the the 1st kind. Applying the Jacobi-Anger expansion to Eq. 3.45 produces

$$A_{out}Q^{-1} = A_{in}\sum_{n=-\infty}^{\infty} i^n J_n(\phi'_{NL})\exp(in\omega_d t) \tag{3.47}$$

$$= \sqrt{P_r}\sum_{n=-\infty}^{\infty} i^n J_n(\phi'_{NL})\exp(i(n-0.5)\omega_d t) + ... \\ \sqrt{P_s}\sum_{n=-\infty}^{\infty} i^n J_n(\phi'_{NL})\exp(i(n+0.5)\omega_d t) \tag{3.48}$$

$$= \sqrt{P_r}\sum_{n=-\infty}^{\infty} i^{n+1} J_{n+1}(\phi'_{NL})\exp(i(n+0.5)\omega_d t) + ... \\ \sqrt{P_s}\sum_{n=-\infty}^{\infty} i^n J_n(\phi'_{NL})\exp(i(n+0.5)\omega_d t) \tag{3.49}$$

$$= \sum_{n=-\infty}^{\infty} i^n \exp(i(n+0.5)\omega_d t)\left[i\sqrt{P_r}J_{n+1}(\phi'_{NL}) + \sqrt{P_s}J_n(\phi'_{NL})\right] \tag{3.50}$$

$$A_{out} = Q\sum_{n=-\infty}^{\infty} i^n \exp(i(n+0.5)\omega_d t)A_n, \tag{3.51}$$

where

$$|A_n|^2 = P_r J_{n+1}^2(\phi'_{NL}) + P_s J_n^2(\phi'_{NL}) \tag{3.52}$$

is the power of the n^{th} order sideband. Note that $n = -1$ corresponds to the input frequency labelled r, while $n = 0$ corresponds to the input frequency labelled s.

3.4 Implications of the Scalar model

If $0 < \phi'_{NL} < \sqrt{1+n}$ for $n \geq 0$, the Bessel functions in Eq. 3.52 can be approximated by the first terms in their Taylor expansion [83],

$$J_n(\phi'_{NL}) \approx \frac{1}{n!}\left(\frac{\phi'_{NL}}{2}\right)^n \tag{3.53}$$

$$= \frac{1}{n!}\left(\gamma L\sqrt{P_r P_s}\right)^n \tag{3.54}$$

$$= \frac{1}{n!}(xy)^{n/2}, \tag{3.55}$$

where the normalizations $x = \gamma LP_r$ and $y = \gamma LP_s$ have been introduced. Utilizing Eq. 3.55 and the normalization $z_n = \gamma L|A_n|^2$ allows Eq. 3.52 to be rewritten as

$$z_n \approx \frac{1}{[(n+1)!]^2} x^{n+1} y^n + \frac{1}{[n!]^2} x^n y^{n+1} \tag{3.56}$$

$$= \frac{1}{[n!]^2} \left(\frac{1}{(n+1)^2} x^{n+1} y^n + x^n y^{n+1} \right). \tag{3.57}$$

For the case where $x \ll y$, Eq. 3.57 can be approximated by

$$z_n \approx \frac{1}{[n!]^2} x^n y^{n+1}, \tag{3.58}$$

which shows that the power of the n^{th} order sideband is proportional to integer exponents of the powers of the input lasers.

3.4.1 Applications in FBG sensing

Equation 3.58 predicts that the power extracted from the n^{th} order sideband will be proportional to the input power raised to the n^{th} exponent. Figure 3.1 demonstrates that this potentiation effect causes peaks in time dependent signals to become more narrow for large values of n, which in turn makes small time shifts easier to detect. Therefore, if the frequency of a tunable laser is swept across an FBG and the signal generated from the reflected light is launched into a highly nonlinear fiber along with a pump laser, the signal detected from the n^{th} order sideband will be a potentiated and thus more narrow version of the FBG spectrum. By effectively reducing the FBG bandwidth, the resolution of an FBG based sensor can thus be increased as shown in the paper presented in Chapter 4.

3.4.2 Applications in CP-OTDR

The results presented in Eq. 3.51 implies that increasing ω_d to $\omega_d + \Delta\omega$ causes the n^{th} order sideband to change its frequency by $n\Delta\omega$ as illustrated in Fig. 3.2. Thus, if a chirped pulse with a duration, D, a chirping range $\Delta\nu_c$ and a square-shaped envelope is launched into a highly nonlinear fiber along with a pump laser, the n^{th} order sideband will produce a chirped pulse with the same duration and a chirping rate

$$\frac{\partial f}{\partial t} = n\frac{\Delta\nu_c}{D}. \tag{3.59}$$

Using these pulses for CP-OTDR can thus increase the shot-to-shot sensing range by a factor of n while decreasing the sensitivity by $1/n$ in accordance with Eq. 2.26. Previously, the increased frequency shift of higher order sidebands was exploited to

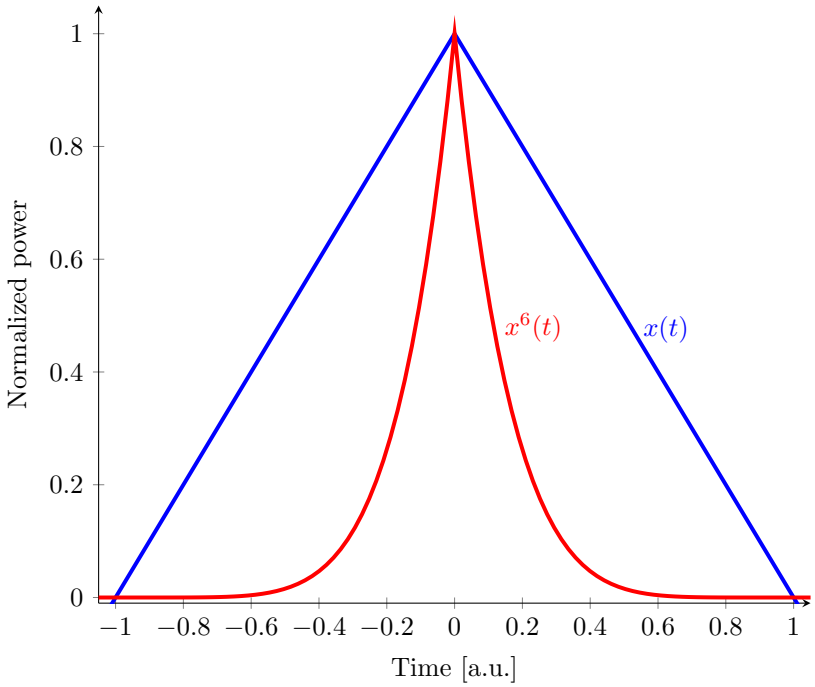

Figure 3.1: Illustration of a signal, $x(t)$, launched into a highly nonlinear fiber and the signal extracted by filtering out the 6th order sideband, $x^6(t)$. Note that potentiation reduces the duration of the signal, making small shifts in the horizontal location of the peak easier to detect.

enhance the resolution of OFDR measurements by extending the range of a frequency sweep taking place on the scale of seconds and the sensitivity of an FBG based temperature sensor [84, 85]. The realization that the same extension would also take place for nanosecond chirped pulses enabled the enhanced shot-to-shot sensing range described in the paper presented Chapter 5.

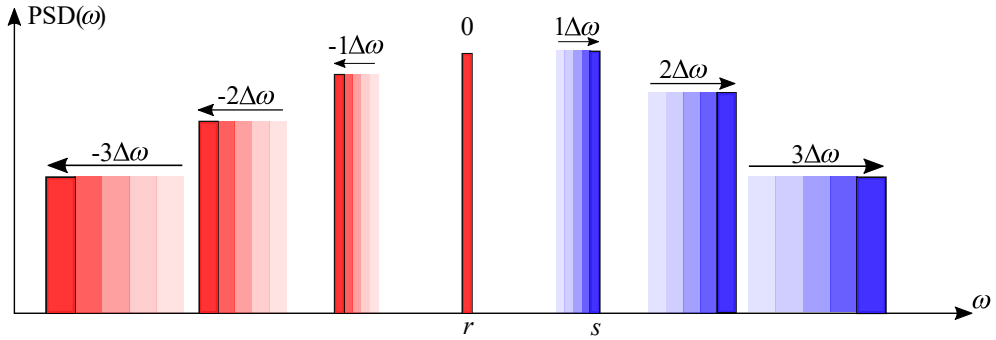

Figure 3.2: Illustration of chirp rate enhancement. If the angular frequency of the signal laser is swept by $\Delta\omega$, the n^{th} order sideband will shift by $n\Delta\omega$.

3.5 Vector model

The scalar model of frequency sideband generation is valid if the input lasers are co-polarized. Experimental measurements indicated that sidebands were still produced if the two lasers are only partially co-polarized and that sideband generation could be completely extinguished for orthogonal states of polarization. Because mechanical vibrations and changes in ambient temperature can change the birefringence of fibers and thus affect the polarization of light propagating within, understanding the exact way sideband power depends on the polarizations of the two input lasers was investigated with the hope of either determining how to stabilize sideband power against fluctuations induced by polarization drifts or exploiting the dependence for new polarimetric sensing schemes. A central contribution of this thesis is the development of a vector model for sideband generation, which provides an analytical expression for the power of the sideband depending on the choice of input polarizations. In the following, an abbreviated derivation of the vector model is presented. A complete derivation is available in Section 6.1, which contains the supplementary material for the paper in Chapter 6.

First, the vector-NLSE without dispersion or attenuation is written as

$$\partial_z |A(z)\rangle = i\gamma \langle A|A\rangle |A(z)\rangle, \tag{3.60}$$

where $|A\rangle = (A_x, A_y)^T$ describes the field amplitude in the x- and y-directions and $\langle A|A\rangle = (A_x^*, A_y^*)(A_x, A_y)^T = |A_x|^2 + |A_y|^2$ is the power of the field. Solving Eq. 3.60 yields

$$|A_{out}\rangle = |A_{in}\rangle \exp(i\gamma L \langle A|A\rangle). \tag{3.61}$$

To obtain the most general possible model for the impact of initial polarization on sideband power, the following input field is defined using the Jones formalism,

$$|A_{in}\rangle = \sqrt{P_r} \begin{pmatrix} \cos\theta \\ \sin\theta e^{i\phi} \end{pmatrix} e^{-i0.5\omega_d t} + \sqrt{P_s} \begin{pmatrix} \cos\beta \\ \sin\beta e^{i\xi} \end{pmatrix} e^{i0.5\omega_d t}. \tag{3.62}$$

Respectively, the parameters θ and β are the angles of the polarization vectors relative to the x-axis for the two lasers, while ϕ and ξ are the respective phase differences between the orthogonal polarization components for the two lasers. Note that the scalar input field in Eq. 3.43 is recovered when $\theta = 0°$. By exploiting the harmonic addition theorem [86], it can be shown that

$$\langle A|A\rangle = P_r + P_s + 2\sqrt{P_r P_s}\sqrt{V}\cos(\omega_d t + \kappa), \tag{3.63}$$

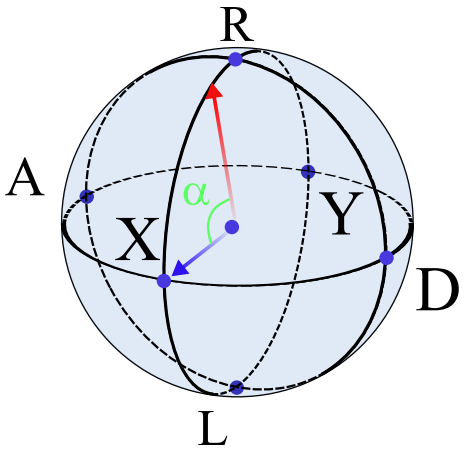

Figure 3.3: Visualization of the Stokes vectors on the Poincaré sphere representing the SOPs of two lasers. The angle, α, can be calculated from their dot product using Eq. 3.65.

where $V = 0.5(1 + \cos(2\theta - 2\beta)\cos^2(0.5(\phi - \xi)) + \cos(2\theta + 2\beta)\sin^2(0.5(\phi - \xi)))$ and κ is a phase factor depending on θ, β, ϕ, and ξ. Through V, the power of the field seemingly depends on the choice of input polarization in a highly nontrivial way, but the expression for V can be greatly simplified by considering the SOPs of the two lasers as normalized Stokes vectors on the Poincaré sphere,

$$\hat{S}_r = \begin{pmatrix} \cos(2\theta) \\ \sin(2\theta)\cos(\phi) \\ \sin(2\theta)\sin(\phi) \end{pmatrix}, \quad \hat{S}_s = \begin{pmatrix} \cos(2\beta) \\ \sin(2\beta)\cos(\xi) \\ \sin(2\beta)\sin(\xi) \end{pmatrix}, \tag{3.64}$$

as visualized in Fig. 3.3 and computing their dot product,

$$\begin{aligned} \cos(\alpha) &= \hat{S}_r \cdot \hat{S}_s \\ &= \cos(2\theta - 2\beta)\cos^2(0.5(\phi - \xi)) + \cos(2\theta + 2\beta)\sin^2(0.5(\phi - \xi)) \\ &= 2V - 1. \end{aligned} \tag{3.65}$$

Rearranging shows that $\sqrt{V} = \cos(\alpha/2)$ and allows Eq. 3.63 to be rewritten as

$$\langle A|A\rangle = P_r + P_s + 2\sqrt{P_r P_s}\cos(\alpha/2)\cos(\omega_d t + \kappa). \tag{3.66}$$

By inserting this expression for the power of the field into Eq. 3.61 and applying the Jacobi-Anger expansion, an expression for the amplitude of the output field can be derived,

$$|A_{out}\rangle = Q \sum_{n=-\infty}^{\infty} i^n e^{in\kappa} e^{i(n+0.5)\omega_d t} |A_n\rangle, \tag{3.67}$$

where Q is defined as in Eq. 3.45 and

$$|A_n\rangle = \left[\begin{pmatrix} iJ_{n+1}(\phi_{NL})\sqrt{P_r}\cos\theta e^{i\kappa} + J_n(\phi_{NL})\sqrt{P_s}\cos\beta \\ iJ_{n+1}(\phi_{NL})\sqrt{P_r}\sin\theta e^{i\phi}e^{i\kappa} + J_n(\phi_{NL})\sqrt{P_s}\sin\beta e^{i\xi} \end{pmatrix}\right] \tag{3.68}$$

with $\phi_{NL} = 2\gamma L\sqrt{P_r P_s}\cos(\alpha/2)$. Proceeding to calculate the power of the n^{th} order sideband yields

$$\langle A_n|A_n\rangle = P_r J_{n+1}^2(\phi_{NL}) + P_s J_n^2(\phi_{NL}) + 2\sqrt{P_r P_s}J_{n+1}(\phi_{NL})J_n(\phi_{NL})B, \tag{3.69}$$

where

$$B = [-\cos\theta\cos\beta\sin(\kappa) - \sin\theta\sin\beta\sin(\kappa + \phi\text{-}\xi)]. \tag{3.70}$$

Using a number of trigonometric identities as explained in Section 6.1, it can be shown that B is always equal to zero, implying that the power of the n^{th} order sideband can be calculated from

$$\langle A_n|A_n\rangle = P_r J_{n+1}^2(\phi_{NL}) + P_s J_n^2(\phi_{NL}). \tag{3.71}$$

3.6 Implications of the vector model

Applying the Taylor expansion of the Bessel functions in Eq. 3.71 for $0 < \phi_{NL} < \sqrt{1+n}$ and $n \geq 0$ yields

$$z_n \approx \frac{1}{[n!]^2}x^n y^{n+1}\cos^{2n}(\alpha/2), \tag{3.72}$$

with the normalizations $x = \gamma L P_r$, $y = \gamma L P_s$ and $z_n = \gamma L\langle A_n|A_n\rangle$ in the limit where $x \ll y$. Equation 3.72 implies that the power of the n^{th} order sideband does not depend on the phases or absolute states of polarization of the two lasers. Only the angle between the Stokes vectors of the input lasers affects the power of the sidebands.

3.6.1 Applications in polarimetric sensing

Equation 3.72 shows that the intensity of the n^{th} order sideband is proportional to $\cos^{2n}(\alpha/2)$, where α is the angle between the SOPs of the signal and reference lasers expressed on the Poincaré sphere. This implies a derivative of

$$\frac{dI}{d\alpha} = -2nI_0\cos^{2n-1}(\alpha)\sin(\alpha), \tag{3.73}$$

which for $n > 1$ has a larger maximum value compared to the one obtained from Eq. 2.36, leading to higher sensitivity to changes in polarization as shown in the paper presented in Chapter 6.

3.6.2 Applications in polarimetry

It is a conceptual novelty that Eq. 3.72 relates measured power to the angle between the SOPs of two lasers expressed as Stokes vectors on the Poincaré sphere without referencing them to physical polarizers. To determine if two lasers are co-polarized using a conventional polarimeter, it is either necessary to launch them into two devices in parallel or into the same device one at a time, apply Eq. 2.39 and subsequently determine how similar their SOPs are. In contrast, Eq. 3.72 allows the total optical power of a sideband to encode the degree of co-polarization of two lasers. Choosing an arbitrary normalized Stokes vector, $\hat{S} = (a, b, c)^T$, for the signal laser and an SOP of the reference laser, $\hat{X} = (1, 0, 0)^T$, the angle between them on the Poincaré sphere is $\alpha_X = \arccos(\hat{S} \cdot \hat{X}) = \arccos(a)$. According to Eq. 3.72, the power of the 1st order sideband is then $P_X = P_{\max} \cos^2(\alpha_X/2)$. Solving for α_X in both expressions shows that $a = 2P_X/P_{\max} - 1$. Doing the same analysis for $\hat{Y} = (-1, 0, 0)^T$ shows that $P_{\max} = P_X + P_Y$ and thus, $a = 2P_X/(P_X + P_Y) - 1$. Repeating this procedure for $\hat{D} = (0, 1, 0)^T$ and $\hat{A} = (0, -1, 0)^T$ along with $\hat{R} = (0, 0, 1)^T$ and $\hat{L} = (0, 0, -1)^T$ shows that

$$\hat{S}^{(\text{measured})} = \begin{pmatrix} 2\frac{P_X}{P_X+P_Y} - 1 \\ 2\frac{P_D}{P_D+P_A} - 1 \\ 2\frac{P_R}{P_R+P_L} - 1 \end{pmatrix}. \tag{3.74}$$

In other words, the SOP of the signal laser can be determined if different SOPs of the reference laser are chosen and the power of the 1st order sideband is measured. This technique was exploited in the paper presented in Chapter 7 to develop a method for all-optical measurement of the SOP of a laser.

Chapter 4

Resolution Enhancement

The contributions of the four listed authors to this paper, titled "Nonlinear Resolution Enhancement of an FBG based temperature sensor using the Kerr effect", published in Optics Express [87], are as follows. The present author built the setup, collected, analyzed and graphed the data and wrote the bulk of the paper. Dr. Chams Baker helped develop the idea for the experiment, suggested using high power pump pulses to "sample" the signal and was instrumental in editing the text of the paper. Prof. Liang Chen and prof. Xiaoyi Bao provided critiques of initial drafts and numerous suggestions for improving the presentation and discussion of the results.

The paper describes an approach for effectively reducing the measured bandwidth of an FBG without modifying the physical characteristics of the grating. Instead of obtaining a narrower spectral width by reducing the average refractive index or increasing the length of the grating as suggested by Eq. 2.13, a tunable laser frequency sweep first maps the grating spectrum to the time domain, subsequently raising it to an integer exponent using the Kerr effect in accordance with Eq. 3.58 and effectively reducing its width. Note that the inherent reflection spectrum of the grating does not change. Rather, the nonlinear processing method accentuates sharp features in the signal by reducing the power of low intensity regions much more than high power regions similar to the approach used in [88] to regenerate data signals. This effect has also been exploited to increase the extinction ratio of optical pulses used for Phase-OTDR, thereby extending the effective sensing range, and for magnifying small signal fluctuations [39].

An FBG used as a temperature sensor was utilized in this experiment because it constitutes a simple, well-understood system that makes it easy to highlight the impact of the resolution enhancement effect. Having established the mechanism for a basic, point-like temperature sensor opens the door to applying the same method to distributed sensors detecting changes in other environmental variables as discussed

in Section 8.2. For simplicity, "resolution" was defined using the Taylor criterion, which considers two spectral lines distinguishable if their separation exceeds their full width at half maximum (FWHM). An alternative definition frequently used in imaging is the Rayleigh criterion, originally defined as the separation in the imaging plane between two point-spread-functions when the maximum of one overlaps with the first zero of the other [89]. Compared to using an amplified continuous wave laser as a pump, using a train of amplified laser pulses allows for greater peak powers, which in turn allows for the generation of higher order sidebands with sufficient intensity. As the power of the input lasers is the primary factor determining the maximum sideband order that can be utilized, pulsing the signal, amplifying it and temporally overlapping it with the high power pump pulses could allow much higher sideband orders to be exploited.

Research Article | Vol. 28, No. 26 / 21 December 2020 / Optics Express 39181
Optics EXPRESS

Nonlinear resolution enhancement of an FBG based temperature sensor using the Kerr effect

OLE KRARUP,* CHAMS BAKER, LIANG CHEN, AND XIAOYI BAO

Fiber Optics Group, Department of Physics, University of Ottawa, Ottawa K1N 6N5, Canada
*okrarup@uottawa.ca

Abstract: We demonstrate the enhancement of the resolution of a fiber optical sensor using all-optical signal processing. By sweeping the frequency of a tunable laser across a fiber Bragg grating, a signal corresponding to the reflection spectrum of the FBG is generated. If another laser with fixed power and frequency is launched into a highly nonlinear fiber along with the FBG-shaped signal, the Kerr effect gives rise to a number of frequency sidebands, where the power in each of the sidebands is proportional an integer exponent of the signal and pump powers. By filtering out particular sidebands, this potentiation effect reduces the width of the FBG-shaped signal, making shifts in its central wavelength easier to distinguish. We report a maximum resolution enhancement factor of 3.35 obtained by extracting the $n = -4$ order sideband, and apply resolution enhancement to improve the resolution of an FBG based temperature sensor. The method described in this paper can be applied to existing fiber based sensors and optical systems to enhance their resolution.

1. Introduction

In high speed telecommunication, optical fibers have become ubiquitous due to their bandwidth and immunity to electromagnetic interference. Light guided by total internal reflection in a silica core can travel dozens of kilometers without significant loss of intensity. Moreover, novel techniques have been developed to allow optical fibers to measure temperature, strain, vibration and other critical information about their surrounding environment [1]. A simple example involves shining broadband light onto a Fiber Bragg Grating (FBG) and measuring the reflected spectrum. Because a change in temperature will change the spatial period of the grating, thereby altering the resonantly reflected wavelength, a careful calibration against a known temperature change yields a reliable thermometer. The resolution of such a measuring scheme depends on the ability to determine small changes in the central reflected wavelength. Ideally, an infinitely narrow reflection spectrum would allow detection of minuscule temperature changes, because smaller changes in the central wavelength of the grating can be distinguished. State of the art, commercially available π-shifted gratings have spectral widths of a few picometers, allowing high resolution measurements to be conducted [2]. Further reduction in spectral width requires either new fabrication techniques or novel methods for processing the signals from existing gratings.

The Kerr effect enables a number of techniques for manipulating signals by all-optical means. One such technique utilizes the power-dependent nature of the Kerr effect to improve the extinction ratio of signals and to magnify small signal fluctuations [3,4]. Another technique to sensitivity enhancement using the Kerr effect exploits the fact that a change in the frequency difference between two signals entering the Kerr medium causes the generated sidebands to shift by the same frequency change multiplied by an order-dependent integer [5].

In this paper, we present a novel technique for enhancing the resolution of FBG-based temperature sensors via all-optical signal processing based on the Kerr effect. First, theory shows that propagation of light composed of two different frequencies, a "pump" and a "signal", in a Kerr medium leads to the generation of sidebands. The power of the sidebands is proportional to integer exponents of the input power and the implications of this potentiation effect to the

#411179 https://doi.org/10.1364/OE.411179
Journal © 2020 Received 30 Sep 2020; revised 16 Nov 2020; accepted 20 Nov 2020; published 11 Dec 2020

Optics EXPRESS

measurement of optical signals are discussed. The potentiation dependence of the sideband power on the input signal is demonstrated experimentally by extracting sidebands up to the $n = -4$ order and applied to enhance the resolution of an FBG based temperature sensor. Subsequently, further applications of the resolution enhancement effect to existing optical sensing systems are discussed.

2. Theory

The following description of the generation of sidebads in a Kerr medium is based on the approach used in [6]. Launching laser light with two different angular fequencies, a signal ω_s and a pump ω_p with $\omega_s<\omega_p$, into a Kerr medium consisting of a Highly-Nonlinear-Fiber (HNLF), the total electric field amplitude is given by $A_{in} = \left[\sqrt{P_s}\exp\left(-0.5i\omega_d t\right) + \sqrt{P_p}\exp\left(0.5i\omega_d t\right)\right]$, where $P_{s/p}$ is the power of the signal/pump fields, $\omega_d = \omega_p - \omega_s$, and the power of this input field is $|A_{in}|^2 = \left[P_s + P_p + 2\sqrt{P_s P_p}\cos\left(\omega_d t\right)\right]$. Neglecting dispersion, loss and polarization effects, this incident field evolves according to the Non-linear Schrödinger Equation, $dA/dz = i\gamma|A|^2$ [7]. Solving this differential equation, the field at the output of the fiber is $A_{out} = A_{in}\exp\left[i\gamma L\left(P_s + P_p\right)\right]\exp\left[i\gamma L\cdot 2\sqrt{P_s P_p}\cos\left(\omega_d t\right)\right]$. The exponential factor $\exp\left[i\gamma L\left(P_s + P_p\right)\right]$ is neglected as it does not affect the power of the output field. The Jacobi-Anger expansion, $\exp\left[iM\cos\left(\Omega t\right)\right] = \sum_{n=-\infty}^{\infty} i^n J_n(M)\exp\left(in\Omega t\right)$ [8], is applied to the factor $\exp\left[i\gamma L\cdot 2\sqrt{P_s P_p}\cos\left(\omega_d t\right)\right]$, allowing the output field to be expressed as the sum of a number of frequency sidebands spaced ω_d apart:

$$A_{out} = \sum_{n=-\infty}^{\infty} i^n e^{i\omega_d\left(n+\frac{1}{2}\right)t}\left[i\cdot J_{n+1}\left(2\gamma L\sqrt{P_s P_p}\right)\sqrt{P_s} + J_n\left(2\gamma L\sqrt{P_s P_p}\right)\sqrt{P_p}\right], \tag{1}$$

where J_n is the n^{th} order Bessel function of the first kind. The sideband $n = 0$ corresponds to ω_p, while $n = -1$ corresponds to ω_s. The power of the n^{th} order sideband is $|A_n|^2 = J^2_{|n+1|}\left(2\gamma L\sqrt{P_s P_p}\right)P_s + J^2_{|n|}\left(2\gamma L\sqrt{P_s P_p}\right)P_p$, and introducing the normalization $x = \gamma L P_s$, $y = \gamma L P_p$, $z_n = \gamma L|A_n|^2$ yields $z_n = xJ^2_{|n+1|}\left(2\sqrt{xy}\right) + yJ^2_{|n|}\left(2\sqrt{xy}\right)$. The Bessel function $J_n(\mathrm{M})$ can be approximated by $1/n!\,(M/2)^n$ under the condition $0<M<\sqrt{1+n}$ [9]. Using this approximation, the power in the n^{th} order sideband becomes

$$z_n \approx x^{|n+1|+1}y^{|n+1|}\frac{1}{((|n+1|)!)^2} + x^{|n|}y^{|n|+1}\frac{1}{(|n|!)^2}. \tag{2}$$

Eq. (2) shows that the normalized output power is proportional to the normalized input power raised to an integer exponent. As an example, filtering out the $n = -2$ sideband yields $z_{-2} \approx x^2\left(y + y^3/4\right)$, so an input signal, x, leads to an output signal proportional to x^2. This potentiation effect is utilized to enhance the resolution of fiber optical sensors. Consider a generic sub/super-Gaussian spectrum with Full Width Half Maximum (FWHM)= 2Λ. The input signal, $x_{in}(\lambda) \propto \exp\left(-\ln(2)\cdot\lambda^m/\Lambda^m\right)$, yields the output signal, $x_{out} \propto \exp\left(-\ln(2)\cdot\lambda^m/(\Lambda_n)^m\right)$, where $2\Lambda_n = 2\Lambda/n^{1/m}<2\Lambda$ is the FWHM of the output signal. If $x_{in}(\lambda)$ is generated by sweeping the wavelength of a laser at a constant rate across an FBG, time dependence can be converted to wavelength dependence and the output signal will be a narrower version of the FBG spectrum. The theoretical decrease in width for various sub/super-Gaussian signals is shown in Fig. 1(a), while Fig. 1(b-d) illustrates that signals with sharp peaks benefit more from resolution enhancement than signals with flat tops.

Optics EXPRESS

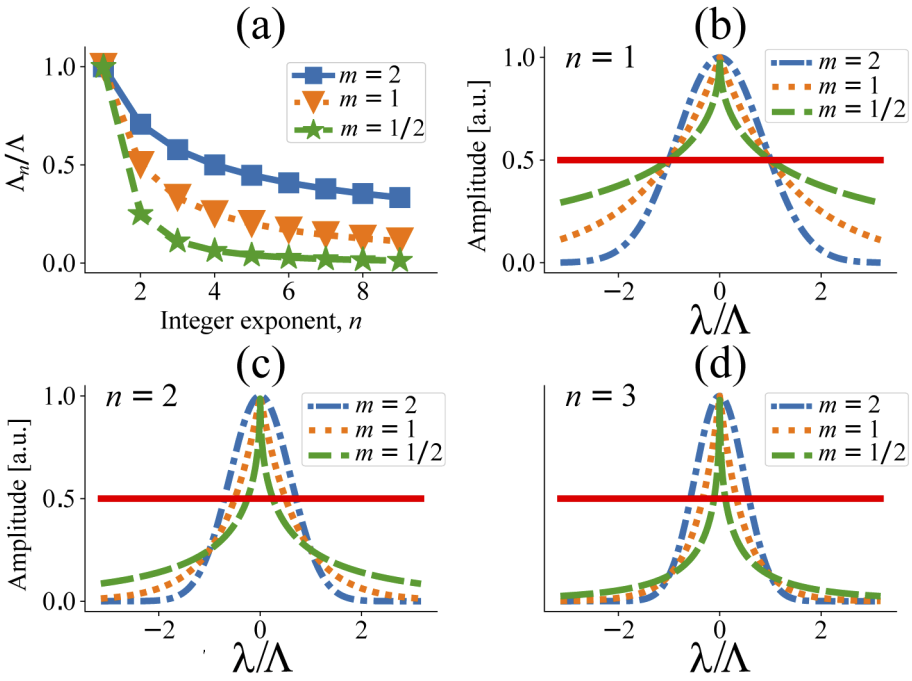

Fig. 1. (a) Decreasing FWHM for different sub/super-Gaussian spectra as the sideband order increases. (b-d) Examples of narrowing for different spectrum types and sideband orders normalized to the peak value for $n = 1, 2, 3$. Such signals can be generated by sweeping the wavelength of a tunable laser across an FBG and converting time dependence to wavelength dependence by using the sweeprate of the laser.

3. Experimental setup

An illustration of the experimental setup utilized for resolution enhancement with the Kerr effect is presented in Fig. 2(a). The signal is generated by a tunable laser (Agilent 81940A) that is swept at a rate of 50 nm/s across 60 pm from 1550.08 nm to 1550.14 nm. Using a 1:99 coupler, 1 % of this light is sent through an auxillary filter (TeraXion C095381 30 pm PSG 1550.12 nm) that is used as a reference and passed directly to a photodiode (Thorlabs PDB130C-AC) connected to an oscilloscope (Agilent infiniium DSO81204B 12 GHz) sampling at 2 GSa/s. The arrival times of all other signals are measured relative to the reference. Any change in arrival time is converted into a wavelength shift by using the sweeprate of the tunable laser. The remaining 99 % of the light from the tunable laser is reflected off an FBG (TeraXion custom 24 pm grating) located inside an oven (Yamato DX300). By changing the temperature inside the oven, the central wavelength of the FBG can be changed. When the wavelength of the light from the tunable laser is swept across the reflection spectrum of the FBG, a signal referred to as the "raw" signal is obtained because the reflected power as a function of time is identical to the reflection spectrum of the FBG. The raw signal is visualized in Fig. 2(b). Using another 1:99 coupler, 1 % of the raw signal is extracted and passed to a photodiode connected to the oscilloscope. The remaining 99 % of the raw signal is combined with high power pump pulses and sent into the Kerr medium (Draka Comteq 418SG 04611A).

To generate the high power pump pulses, a Distributed Feedback (DFB) laser (Lucent M-E2566H) centered at 1549.60 nm is driven by a function generator (Agilent 33250A) using 10 ns pulses with a 100 ns period. The experiment can be conducted with a CW pump laser, but pulses are utilized to achieve higher peak powers and supress Stimulated Brillouin Scattering (SBS). The

Optics EXPRESS

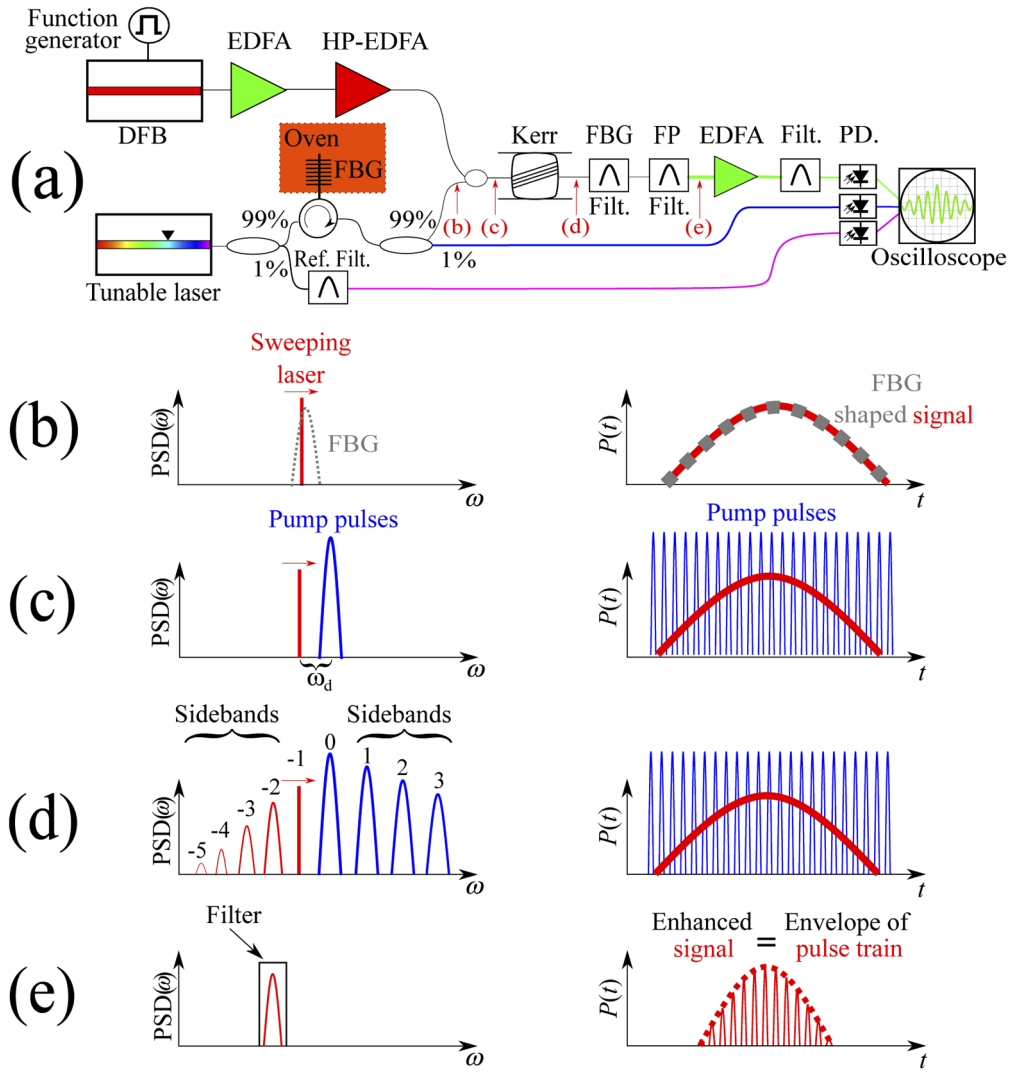

Fig. 2. (a) Experimental setup. The magenta fiber contains the reference signal, while the blue fiber contains the raw signal from the FBG. The green fiber contains the resolution enhanced signal obtained by extracting the n^{th} order sideband. (b-e) The spectrum and signal at successive stages of the experiment.

Optics EXPRESS

generated laser pulses are amplified using a conventional Erbium Doped Fiber Amplifier (EDFA) (GN Nettest fiberamp BT 17) followed by a High Power EDFA (Amonics AEDFA-33-B-FA). The combination of the high power pump pulses with the signal is visualized in Fig. 2(c). The Kerr effect giving rise to sidebands is illustrated in Fig. 2(d). A measurement of the spectrum immediately after the Kerr medium is presented in Fig. 3 showing the signal, the pump and the sidebands generated by the Kerr effect.

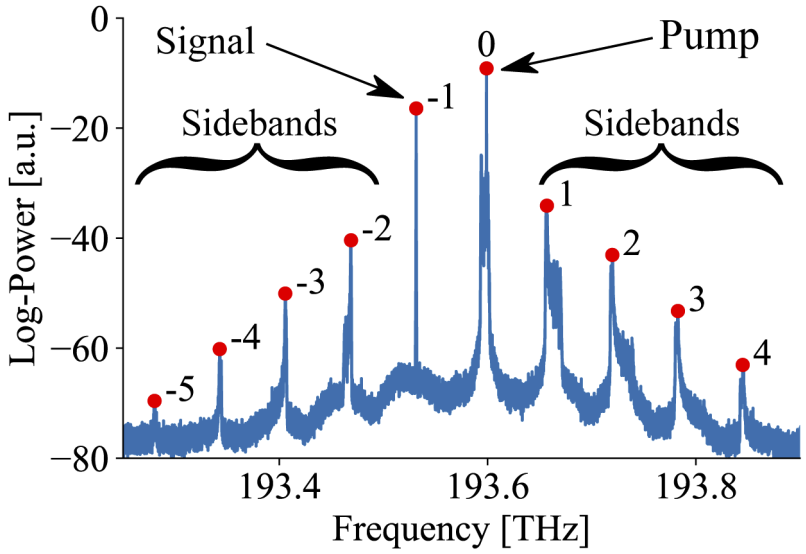

Fig. 3. Spectrum after the Kerr medium with sideband orders labelled. The $n = 0$ peak corresponds to the high power pump pulses, while the $n = -1$ peak is the frequency of the tunable laser that sweeps across the FBG to generate the signal. The sidebands $n = -2, -3, -4, \ldots$ can be extracted to obtain outputs that are proportional to integer powers of the input signal.

Individual sidebands are extracted using two filters (AlnairLabs WTF-200 100 pm, and JDS Uniphase TB25MI+1FP Tunable 215 pm Etalon Filter) to ensure that the signal in the sidebands is extracted without the high power pump pulses leaking through and distorting the measurement. At this stage, the extracted sideband consists of a train of pulses, whose envelope is proportional to an integer power of the raw signal as visualized in Fig. 2(e). The signal is amplified by an EDFA (Amonics AEDFA-PA-25-B-FA), passed through a bandpass filter (JDS FITEL TB45B+1SC 500 pm Tunable Filter) to remove ASE noise, and detected by a photodiode connected to the oscilloscope. From the trace detected by the oscilloscope, the peaks of the pulse train can be digitally extracted to obtain the envelope, which is referred to as the "sideband" signal. The measured traces corresponding to the reference, the raw signal, and the sideband signal are presented in Fig. 4(a). Examples of three sideband signals for $n = -2, -3, -4$ are presented in Fig. 4(b-d). The FWHM of the raw signal is 8.81 pm, while the FWHM of the sideband signals are 4.78 pm, 3.91 pm and 2.63 pm respectively. This corresponds to reductions in width by factors of 1.84, 2.25 and 3.35 respectively in agreement with the theory in Sec. 2.

The oven is heated to 40 °C, turned off and allowed to cool gradually. The internal temperature of the oven is measured with a thermocouple thermometer (TES 1310 TYPE-K). The raw- and sideband-traces produced by the orders $n = -2$ and $n = -4$ are measured for temperatures between 32 °C and 40 °C. The changing arrival time relative to the reference trace is determined and converted into a wavelength shift using the sweeprate of the tunable laser. The result is shown in Fig. 5. The Taylor Criterion states that two spectral peaks can be distinguished if they

Optics EXPRESS

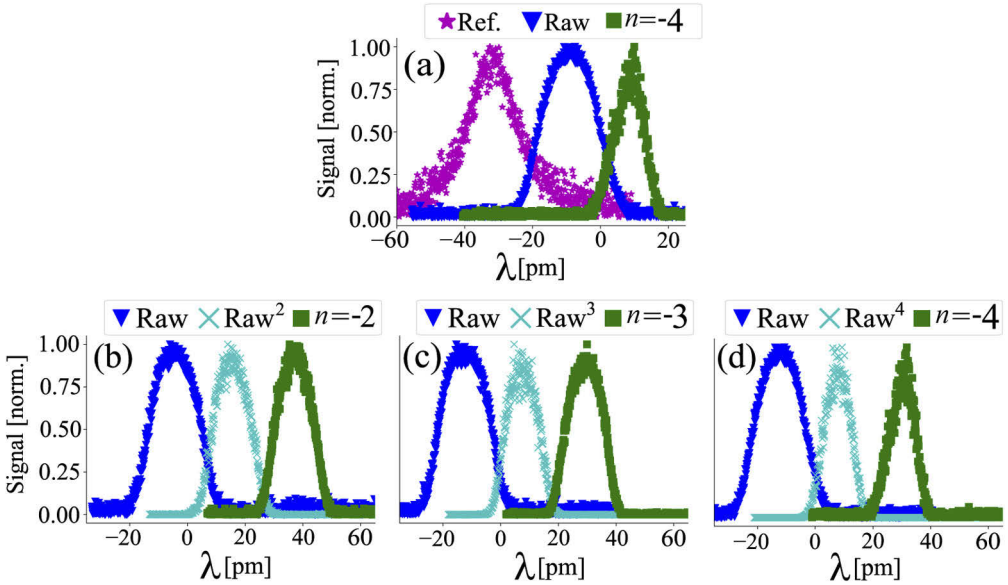

Fig. 4. (a) Example of the signal collected from the auxillary filter used as a reference (magenta), the raw signal (blue) and the sideband signal (green). (b-d) Raw signals (blue) and sideband signals (green) for different sideband orders. The raw signal raised to the appropriate integer power (light blue) is included for comparison with the sideband signal. Traces are horizontally offset for clarity.

are more than one FWHM apart [10]. Applying the Taylor Criterion and using the fitted slopes from Fig. 5, the smallest discernable temperature difference is 8.81 pm · 0.092 °C/pm= 0.81°C for the raw signal. For the $n = -2$ and $n = -4$ sideband traces, the temperature resolutions according to the Taylor Criterion are 0.45 °C and 0.24 °C respectively.

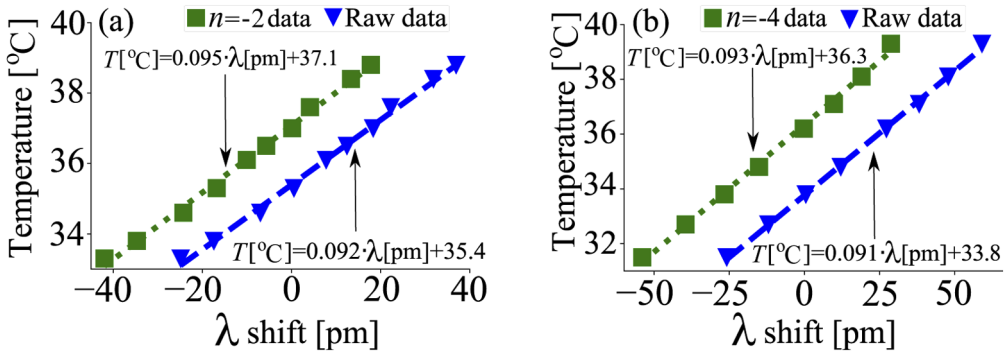

Fig. 5. (a) Temperature calibration done with the $n = -2$ order sideband. (b) Temperature calibration done with the $n = -4$ order sideband. Data has been horizontally offset for clarity.

4. Discussion

A number of simplifying assumptions are used in the derivation in Sec. 2. It is assumed that both the signal and the pump pulses can be considered quasi-CW. For the quasi-CW assumption

Optics EXPRESS

to be applicable, the sinusoidal modulation created by the beat of the distinct pump and signal frequencies must have a period significantly shorter than the duration of the signal or pulse. In other words, the spectral width of the raw signal and the pump in Fig. 3 must be smaller than the frequency spacing between them, which in the present case is 62.4 GHz leading to a beat period of 16 ps. Because the beat period of 16 ps is much shorter than the pump pulse duration of 10 ns, the quasi-CW assumption is valid. Dispersion and loss are also assumed to be negligible and polarization effects are ignored. A model that takes dispersion, loss and polarization into account will be investigated in future works.

The resolution enhancement effect is greater for higher order sidebands, but according to Eq. (2), the power in the sidebands decreases as $1/(n!)^2$ for higher orders. Thus, while the magnitude of the resolution enhancement does not depend on the sideband power, extraction of higher order sidebands requires high input power, making the ability of the optical components to handle such levels of power a limiting factor. Cascading multiple resolution enhancement systems could allow for further resolution enhancement without risking damage due to high power.

The resolution enhancement effect studied in this work was only applied to a single FBG, but could be generalized to distributed gratings. Also, atomic and molecular transition lines studied via Tunable Diode Laser Absorption Spectroscopy (TDLAS) could be measured more accurately if resolution enhancement were applied [11]. Another potential application is to more precisely determine the transmission spectra of Fabry-Pérot (FP) cavities. A recent work determined that if the ends of an FP cavity have reflectivities R_1 and R_2, where their geometric mean, $\sqrt{R_1R_2}$, is greater than or equal to 17.2 %, individual Lorentzian lines of the cavity's transmission spectrum can be distingished subject to the Taylor Criterion [12]. For geometric means of the reflectivities below 17.2 %, measuring the transmission as a function of frequency yields a spectrum that never drops below 0.5, violating the Taylor Criterion. Applying the resolution enhancement technique, the smallest geometric mean of the reflectivities that produces a transmission spectrum obeying the Taylor Criterion will be $\left[\sqrt{R_1R_2}\right]_n = (2^{1/2n} - 1)^2/(2^{1/n} - 1)$ yielding values of 8.64 %, 5.77 % and 4.35 % for the sidebands $n = -2, -3$, and -4, respectively.

Another possibility is enhancement of the resolution of diffraction limited imaging systems used in astronomy and condensed matter physics [13–15]. If a light-emitting point is imaged by an ideal lens onto a screen in the focal plane of the lens, an Airy pattern consisting of a central, bright spot surrounded by alternating dark and bright rings will appear on the screen as determined by the principles of Fourier optics [16]. The width of the smeared out central spot of the Airy pattern on the screen limits the ability to detect changes in the position of the light emitting point. If one images the point onto a collection of optical fibers in the focal plane and subsequently applies the resolution enhancement technique, it would be possible to reduce the FWHM of the detected spot by factors 1.39, 1.69 and 1.96 for sidebands $n = -2, -3$, and -4 respectively.

5. Conclusion

Resolution enhancement based on the Kerr effect is demonstrated for sideband orders up to $n = -4$. The effect allows the measured width of the reflection spectrum of an FBG to be reduced by purely optical means, thereby improving the resolution of a temperature sensing system by a factor 3.35 in accordance with theoretical predictions. The resolution enhancement effect can be applied to a wide range of existing optical sensing systems to improve their resolutions.

Funding

Natural Sciences and Engineering Research Council of Canada (RGPIN-2015-06071, STPGP 506628); Canada Research Chairs (950231352).

Optics EXPRESS

Disclosures

The authors declare no conflicts of interest.

References

1. W. W. Morey, G. Meltz, and W. H. Glenn, "Fiber Optic Bragg Grating Sensors," Fiber Opt. and Laser Sens. VII **1169**, 98–107 (1990).
2. G. P. Agrawal and S. Radic, "Phase-shifted fiber bragg gratings and their application for wavelength demultiplexing," IEEE Photonics Technol. Lett. **6**(8), 995–997 (1994).
3. C. Baker, B. Vanus, M. Wuilpart, L. Chen, and X. Bao, "Enhancement of optical pulse extinction-ratio using the nonlinear kerr effect for phase-otdr," Opt. Express **24**(17), 19424–19434 (2016).
4. B. Vanus, C. Baker, L. Chen, and X. Bao, "All-optical intensity fluctuation magnification using kerr effect," Opt. Express **28**(3), 3789–3794 (2020).
5. J. Du, L. Li, X. Fan, Q. Liu, and Z. He, "Sensitivity enhancement for fiber bragg grating sensors by four wave mixing," Photonics **2**(2), 426–439 (2015).
6. A. Boskovic, S. V. Chernikov, J. R. Taylor, L. Gruner-Nielsen, and O. A. Levring, "Direct continuous-wave measurement of n2 in various types of telecommunication fiber at 1.55 μm," Opt. Lett. **21**(24), 1966–1968 (1996).
7. G. Agrawal, "Chapter 4 - self-phase modulation," in "Nonlinear Fiber Optics (Fifth Edition)," G. Agrawal, ed. (Academic Press, Boston, 2013), Optics and Photonics, pp. 87–128, fifth edition ed.
8. "NIST Digital Library of Mathematical Functions," http://dlmf.nist.gov/, Release 1.0.27 of 2020-06-15. F. W. J. Olver, A. B. Olde Daalhuis, D. W. Lozier, B. I. Schneider, R. F. Boisvert, C. W. Clark, B. R. Miller, B. V. Saunders, H. S. Cohl, and M. A. McClain, eds.
9. G. Watson, *A Treatise on the Theory of Bessel Functions*, Cambridge Mathematical Library (Cambridge University Press, 1995).
10. M. Francon, *Optical Interferometry: By m. Francon* (Academic Press, New York, 1966).
11. D. T. Cassidy and J. Reid, "Atmospheric pressure monitoring of trace gases using tunable diode lasers," Appl. Opt. **21**(7), 1185–1190 (1982).
12. M. Pollnau and M. Eichhorn, "Spectral coherence, Part I: Passive-resonator linewidth, fundamental laser linewidth, and Schawlow-Townes approximation," Prog. Quantum Electron. **72**, 100255 (2020).
13. S. Saha, *Diffraction-Limited Imaging with Large and Moderate Telescopes* (Singapore ; Hackensack, NJ, 2007).
14. J. H. Denschlag, J. Simsarian, H. Häffner, C. McKenzie, A. Browaeys, D. Cho, K. Helmerson, S. Rolston, and W. D. Phillips, "A bose-einstein condensate in an optical lattice," J. Phys. B: At., Mol. Opt. Phys. **35**(14), 3095 (2002).
15. E. Betzig, "Excitation strategies for optical lattice microscopy," Opt. Express **13**(8), 3021–3036 (2005).
16. E. Hecht, *Optics* (Pearson Education, Incorporated, 2017).

Chapter 5

Frequency sweep extension

The contributions of the four authors listed in this paper, titled "Frequency sweep extension using the Kerr effect for static temperature measurement range enhancement in Chirped Pulse ϕ-OTDR", published in Optics Express [90], are as follows. The present author's theoretical work on frequency sideband generation via the Kerr effect provided the inspiration for increasing the chirping rate of a nanosecond optical pulse. The idea of simultaneously using "pure pulses" and "Kerr pulses" to ensure an accurate characterization of the improvement in shot-to-shot sensing range, along with the writing of the introduction, the theory section on the Kerr effect, the section on the experimental setup and the discussion section are also attributable to the present author. Yuan Wang, who is the main collaborator and a fellow PhD student in the Fiber Optics Research Group at the University of Ottawa, had practical experience with CP-OTDR and, when asked about the implications of an increased chirping rate, noted that it would extend the shot-to-shot sensing range. He had previously constructed the part of the setup labelled "Chirped Pulse Generator" presented in Fig. 1 including a custom circuit board for using the solid state optical amplifier (SOA) to pulse the DFB laser, which was reused in the present experiment. Yuan Wang also wrote the section explaining the theory of CP-OTDR, conducted the data analysis, and produced the graphs in a state of continuous discussion and feedback with the present author. The construction of the experimental setup and the data collection was done collaboratively by the present author and Yuan Wang. Prof. Liang Chen and prof. Xiaoyi Bao provided advice on the presentation of the data as well as comments on the main text of the paper.

The purpose of this paper is to increase the chirping rate of a laser pulse by all-optical means and use it to detect larger temperature changes in a fiber. The CP-OTDR technique was first explored in [3], while frequency sweep extension via the Kerr effect has been utilized to enhance the sensitivity of FBG based temperature-

and strain sensors [85], and to increase the frequency sweeping rate of a laser used in OFDR to improve measurement resolution [84]. The present author's realization that the increase in the frequency sweeping rate would also apply to short pulses with durations on the scale of nanoseconds, and the subsequent discussion with Yuan Wang about the implication of this increase for CP-OTDR provided inspiration for the presented experiment. Subsequently, Yuan Wang wrote a paper without contributions from the present author, where the chirp extension method is further improved by using both a chirped reference laser and a chirped signal laser [91].

If a weak signal generated by Rayleigh back-scattering in an ordinary fiber enters an EDFA placed before the photodetector, the noise power added by the amplifier risks being so large compared to the signal power after amplification that reliable detection is not possible. The paper presented in this chapter utilizes a so-called random fiber grating array (RFGA) to back-scatter chirped pulses, instead of relying on inherent Rayleigh back-scattering [92]. An RFGA can be viewed as an FBG with randomly spaced increases in the refractive index, which yields a reflection spectrum with a broad envelope containing many resonances of varying strength. For the purpose of modelling the reflection of a chirped pulse, the RFGA can simply be treated as a segment with a much higher Rayleigh scattering coefficient than the rest of the fiber. The effective increase in the reflection coefficient provided by the RFGA yields a signal, which is strong enough for optical amplification before detection to be unnecessary.

The ability to increase the chirping range according to Eq. 3.59 is theoretically limited by the response time of the Kerr effect, which depends on how fast the electron clouds in the glass react to changes in an applied electric field. Since this reaction time is on the scale of femtoseconds, it is theoretically possible to enhance chirps on the scale of THz. In practice, the nonlinear model from which Eq. 3.59 is derived is only valid when dispersion can be neglected. To ensure that the spectra of different sideband pulses do not overlap, the reference- and signal lasers must have a frequency difference that is sufficiently large. However, a large frequency difference moves at least one of the lasers further from the zero-dispersion wavelength of the Kerr medium, which reduces sideband generation efficiency and makes extracting a sufficiently strong enhanced pulse difficult.

As implied by Eq. 2.26, a trade-off exists between high sensitivity and high shot-to-shot sensing range for CP-OTDR. An interesting solution to this issue is to utilize time-division multiplexing to interrogate the RFGA with a series of pulses stemming from different sideband orders. Thus, lower order pulses can detect small temperature changes with high sensitivity, while higher order pulses can capture sudden spikes

in temperature that would otherwise cause the lower order pulses to decorrelate. Alternatively, because the frequency bandwidth of the RFGA is typically much greater than bandwidth of individual sideband pulses and since it can be ensured that their frequency ranges do not overlap, it should be possible to send the output of the Kerr medium directly to the RFGA, split the signal into a number of branches with appropriate bandpass filters and detect the reflected signals corresponding to each sideband in parallel.

Research Article | Vol. 29, No. 15 / 19 July 2021 / Optics Express 23202
Optics EXPRESS

Frequency sweep extension using the Kerr effect for static temperature measurement range enhancement in Chirped Pulse φ-OTDR

YUAN WANG,[1,3] OLE KRARUP,[2,3,*] LIANG CHEN,[2] AND XIAOYI BAO[1,2]

[1] School of Electrical Engineering and Computer Science, University of Ottawa, Ontario K1N 6N5, Canada
[2] Department of Physics, University of Ottawa, 25 Templeton Street, Ottawa, Ontario K1N 6N5, Canada
[3] These authors contributed equally to this paper
[*] okrarup@uottawa.ca

Abstract: In Chirped Pulse φ-OTDR systems used for sensing temperature or strain along an optical fiber, the largest disturbance between two single-shot measurements that can reliably be detected depends on the range of frequencies swept by the chirped pulse. If electrical modulation is used to generate the laser frequency sweep, the achievable sweeping range is limited by the electrical components, leading to a narrow measurement range for static measurements. In this work, we demonstrate the extension of the frequency range of a chirped laser pulse by all-optical means using evenly spaced frequency sidebands generated via the Kerr effect to improve the Chirped Pulse φ-OTDR measurement range. We report chirp extensions by factors up to 13 and apply the effect to achieve a sixfold increase in the measurement range of a Chirped Pulse φ-OTDR system measuring the temperature of a random fiber grating array. The method described in this paper can be applied to other optical systems utilizing chirped laser pulses and allow for variable extension of their chirping range.

1. Introduction

Compared to devices based on electrical signals, environmental sensors utilizing optical fibers have a number of advantages. Apart from durability and immunity to electromagnetic interference, optical fibers allow for distributed sensing, where information is recorded along their entire length. To measure a quantity of interest, such as local temperature, strain or vibration, a technique referred to as phase sensitive Optical Time Domain Reflectometry (φ-OTDR) is often employed. By launching a monochromatic pulse of light into a fiber and measuring the Rayleigh back-scattered intensity as a function of time, one can determine the state of the fiber along its length in a continuous manner [1]. However, since the relationship between the magnitude of an applied disturbance and the change in the intensity of the back-scattered Rayleigh traces is not linear, conventional amplitude demodulation cannot be used in φ-OTDR to measure the magnitude of the disturbance [2] [3] [4]. Measuring the magnitude of disturbances requires the use of various phase demodulation techniques. These involve comparing the relative phase change of two different segments of fiber [5], utilizing 90° optical hybrid based homodyne detection [6], dual-pulse phase modulation [7], or the phase-generated carrier demodulation algorithm [8]. One drawback of phase demodulation techniques is their reliance on optical interferometers, which are limited by phase recovery range and fringe contrast.

To obtain accurate, single-shot measurements of the magnitudes of applied disturbances based on back-scattered Rayleigh traces, one can instead utilize chirped pulses, where the instantaneous frequency of the pulse is linearly increased or decreased within pulse duration. This technique called Chirped Pulse φ-OTDR (CP φ-OTDR) relies on the interference of a range of frequencies back-scattered by different parts of the fiber due to the Rayleigh effect. By calculating the cross

#430682 https://doi.org/10.1364/OE.430682
Journal © 2021 Received 4 May 2021; revised 17 Jun 2021; accepted 27 Jun 2021; published 7 Jul 2021

Optics EXPRESS

correlation between subsequent Rayleigh traces, such sensing systems have achieved resolutions of 1 mK for temperature and 4 $n\varepsilon$ for strain [9]. When using Rayleigh traces from chirped pulses scattered by a random fiber grating array (RFGA), lower pulse powers are required and a spatial resolution of 1.2 m can be achieved [10]. Since CP φ-OTDR with an RFGA is a single-shot system which does not require heterodyne detection, one section of the sensor without disturbance could be utilized for compensating time delay errors induced by laser frequency drifts. This technique enables the detection of ultra-low frequency vibrations [11]. While CP φ-OTDR is highly sensitive because the Rayleigh traces undergo large changes from small applied disturbances, the static measurement range is limited because subsequent traces become decorrelated if the external perturbation is too large. In practice, two Rayleigh traces recorded before and after a disturbance is applied will be approximately identical (with high correlation coefficient) apart from a time delay, Δt, if this delay is smaller than 10% of the pulse duration. To conduct dynamic measurements, large perturbations could be detected by oversampling using a high repetition rate for the pulses. However, in distributed sensing systems, there is a trade off between pulse repetition rate and sensor length. To extend the limited measurement range, one method based on multi-frequency database demodulation has been implemented [12]. By establishing a database consisting of Rayleigh traces collected from chirped pulses with different initial optical frequencies, the time delays Δt due to large strains can be partially compensated by the initial frequency difference of the chirped pulses, thereby extending the static measurement range by a factor of 3. Additional extension of the measurement range using this method requires building a database for a larger number of frequencies, which is time consuming. Another direct way to extend the measurement range is to increase the range of frequencies swept by each chirped pulse.

When two frequencies of light are launched into a fiber with a large nonlinear parameter, γ, the Kerr effect causes frequency sidebands to be generated. Since the output power of these sidebands depends on the input power, the Kerr effect has been used to enhance the extinction ratio of optical pulses for OTDR by all-optical means [13], and to enhance the resolution of fiber optical sensors [14]. Furthermore, changing the frequency spacing between the input lasers causes the central frequencies of the higher order sidebands to shift by integer multiples of this change. When used in Optical Frequency Domain Reflectometry (OFDR), this method can extend the range of a laser frequency sweep taking place on the scale of seconds, thereby improving the resolution of an OFDR measurement [15]. This frequency chirp magnification (FCM) induced by the Kerr effect has also been used for magnifying the wavelength drift of an FBG sensor subject to strain and temperature changes, thereby enhancing its sensitivity [16]. Because the Kerr effect is fundamentally caused by the reaction of bound electrons in the glass fiber to variations in the power of an external optical field, the smallest duration of a sweep extendable using the Kerr effect is determined by the electron response time, which is on the scale of femtoseconds. Therefore, it should be possible to extend frequency sweeps, which are much shorter in duration than ones typically used in OFDR.

In this paper, we apply the method of extending frequency sweeps using the Kerr effect to broaden the chirp range of a nanosecond optical pulse by factors up to 13 through all-optical signal processing. First, the measurement principle behind CP φ-OTDR, its advantages and limitations are discussed. A theoretical model describing sideband generation using the Kerr effect is then presented, showing how the frequency shift of a sideband depends on its order. An experimental setup used for extending the chirping range of a pulse is described, and it is shown how the static temperature measurement range of a system based on an RFGA can be increased by factors up to 6. Finally, the limitations of our model and experiment are discussed along with potential application to other optical techniques relying on chirped pulses.

Optics EXPRESS

2. Theory

2.1. Chirped Pulse φ-OTDR measurement principle

In traditional φ-OTDR, a monochromatic pulse is employed as the interrogation signal to investigate the status of the fiber. The lack of a linear relationship between the applied external disturbance and the intensity of Rayleigh traces means that the magnitude of the disturbance cannot be determined directly. In order to create a linear relationship between applied disturbances and the intensity profile of the Rayleigh traces, a chirped pulse is utilized instead of a monochromatic pulse. The instantaneous optical frequency profile of the chirped pulse is expressed as [12]

$$v(t) = \left(v_0 + \frac{\Delta v}{W} \cdot t\right) \mathrm{Rect}(t/W), \tag{1}$$

where v_0 is the initial laser frequency, Δv is chirping range of the chirped pulse, W is the pulse duration, and Rect is the rectangular function with unit height. When the chirped pulse is sent into the fiber under test, the interference of back-scattered electrical fields occurring in the fiber section corresponding to the half pulse width will form the time domain Rayleigh traces. At the time t, when the interference signal arrives at the detection end, the optical power can be expressed as:

$$I(t)_{AC} = I_0 \int_{(t-W)c/2n}^{tc/2n} \int_{(t-W)c/2n}^{tc/2n} e^{-2\alpha(Z_i+Z_j)} r\left(Z_i\right) \cdot r\left(Z_j\right) \cdot e^{i\left[\Delta\varphi_{ij}(t)\right]} dZ_i dZ_j, \tag{2}$$

where n is the average value of refractive index, c is the speed of light in vacuum, α is the average attenuation of the fiber, Z_i and Z_j are the positions of the i^{th} and j^{th} scattering centers along the fiber, I_0 is the input intensity of the light and $r(Z_i)$ and $r(Z_j)$ are the reflection coefficient of the i^{th} and j^{th} scattering centers respectively. The exponent, $\Delta\varphi_{ij}(t)$, represents the phase difference between two scattering centers and is given by:

$$\Delta\varphi_{ij}(t) = 2\pi \int_{t-2nZ_j/c}^{t-2nZ_i/c} \left(v_0 + \Delta v \cdot t/W\right) dt = 2\pi \left[\left(\frac{2n\left(Z_i - Z_j\right)}{c}\right)\left(v_0 + \frac{\Delta v}{W}\left(t - \frac{n\left(Z_i + Z_j\right)}{c}\right)\right)\right]. \tag{3}$$

Equation (2) shows that the measured optical power depends on the interference of light from all combinations of two scattering centers, while Eq. (3) shows that the relative phase between two scattering centers depends on their relative optical path lengths, their absolute position along the fiber and the range of the frequency sweep. To understand how CP $\varphi-$OTDR enables environmental sensing, consider a simplified picture with only two scattering centers located at Z_a and Z_b being illuminated by a chirped pulse with a fixed chirping rate, $\Delta v/W$, and a spatial width, which is much greater than $Z_b - Z_a$. At a time, t, after the chirped pulse was launched, a certain signal intensity, $I(t, T_1)$, is detected due to the interference of frequencies scattered by the two centers, when the temperature is T_1. If the temperature of the fiber is increased slightly to T_2 so the optical path length between the centers is increases from L to $L + \Delta L$, the intensity value, $I(t, T_1)$, from before the temperature change will now occur at a different time, $I(t + \Delta t, T_2)$. The reason is that the frequencies that gave rise to $I(t, T_1)$ arrive at the scattering centers slightly later. If ΔT is large enough for the arrival time of the frequencies to be different, but small enough for the way they interfere to be unaltered, one can assume that the intensities $I(t, T_1) = I(t + \Delta t, T_2)$ are actually generated by the same segment of fiber being exposed to two different frequency ranges starting at $v(t)$ and $v(t + \Delta t)$ respectively. The relative change in optical path length must then be related to the change in the frequency range by

$$\frac{\Delta L}{L} = \frac{v(t) - v(t + \Delta t)}{v_0} = -\frac{1}{v_0}\frac{\Delta v}{W}\Delta t. \tag{4}$$

Optics EXPRESS

Considering that a change in temperature causes the optical path length ratio to change by $K_T \cdot \Delta T$, where K_T is the coefficient of linear thermal expansion for the fiber, one can determine that:

$$\mathrm{K}_{\Delta \mathrm{T}} \cdot \Delta \mathrm{T} = -\frac{\frac{\Delta v}{W}\Delta t}{v_0} \Rightarrow \Delta t = -\frac{W \cdot v_0 \cdot \mathrm{K}_{\mathrm{T}}}{\Delta v} \cdot \Delta \mathrm{T} \tag{5}$$

This shows that a small applied temperature change causes a time delay, Δt, which is linearly dependent on the magnitude of the disturbance. The time delay between two traces can be found by calculating the correlation between them. Note that if the chirp range, Δv is small, a small change in temperature will cause a large time shift. In this case, the sensitivity of the CP φ-OTDR will be high while its measurement range will be short. If the chirping range is increased, the same change in temperature will cause a smaller time delay, meaning that the static measurement range is increased at the cost of lower sensitivity. In the demodulation process, the maximum detectable time delay is about 10% of pulse duration, W. If the time delay Δt is too large, the integration range in Eq. (2) for I(t) and I (t+Δt) are significantly different. This means that the interference of back-scattered light occurs in different sections of the RFGA, which makes the two traces decorrelate. Therefore, the maximum measurable temperature change only depends on the frequency chirping range Δv according to Eq. (5), since the duration, W, cancels out on both sides if Δt is replaced with $0.1 \cdot W$. In short, a method that allows the chirping range to be extended can increase the static measurement range.

2.2. Sideband generation using the Kerr effect

The following description of the generation of sidebands in a Kerr medium is based on the approach used in [17]. Sending laser light with two different frequencies, ω_p<ω_c into a Kerr medium consisting of an optical fiber of length, L, with a high nonlinear parameter, γ, the normalized electric field amplitude is initially given by $A_{in} = \left[\sqrt{P_p}\exp(-i0.5\omega_d t) + \sqrt{P_c}\exp(i0.5\omega_d t)\right]$. Here, $P_{p/c}$ referes to the power of the pump field/chirped pulses, $\omega_d = \omega_c - \omega_p$, and the power of the field as a function of time is $P_{in} = \left[P_p + P_c + 2\sqrt{P_p P_c}\cos\omega_d t\right]$. Assuming that dispersion, loss, and polarization effects are negligible, the input field evolves according to the Nonlinear Schrödinger Equation, $dA/dz = i\gamma|A|^2 A$ [18]. Solving this differential equation for the field at the output of the Kerr medium yields $A_{out} = A_{in}\exp\left[i\gamma L(P_p + P_c)\right]\exp\left[i\gamma L 2\sqrt{P_p P_c}\cos\omega_d t\right]$. In the following, the exponential factor, $\exp\left[i\gamma L(P_p + P_c)\right]$, is ignored, as it does not affect the output frequency if the input powers remain constant. Chirps induced by self-phase modulation (SPM) are only present near the pulse edges constituting less than 5% of pulse duration and do not contribute significantly to the scattered signal. The Jacobi-Anger expansion [19], $\exp\left[iM\cos Bt\right] = \sum_{n=-\infty}^{\infty} i^n J_n(M)\exp(inBt)$, where J_n indicates the n^{th} order Bessel function of the first kind is then applied to the output field, thereby expressing it as an infinite sum of frequency sidebands spaced ω_d apart:

$$A_{out} = \sum_{n=-\infty}^{\infty} i^n e^{in\omega_d t}\left[J_n\left(2\gamma L\sqrt{P_p P_c}\right)\sqrt{P_p} + i\cdot J_{n-1}\left(2\gamma L\sqrt{P_p P_c}\right)\sqrt{P_c}\right]. \tag{6}$$

Note that $n = 0$ corresponds to the output sideband located at the frequency of the input pump, ω_p, while $n = 1$ corresponds to the output sideband located at the same frequency as the input chirped pulses. The central frequency of the n^{th} order sideband will be $\omega_n = n\omega_d = n(\omega_c - \omega_p)$ away from ω_p. Assuming that ω_c changes linearly with time at a rate of $\Omega[rad/s^2]$, the frequency of the n^{th} order sideband becomes $\omega_n(t) = n(\omega_c(0) + \Omega t - \omega_p) = n\Omega t + n(\omega_c(0) - \omega_p)$. This shows that if the input pulse is chirped at a rate, Ω, filtering out the n^{th} order sideband will produce a pulse with a chirp rate $n\Omega$. Furthermore, if the condition $0<2\gamma L\sqrt{P_c P_c}<\sqrt{1+|n|}$ is satisfied, the intensity profile of the output pulse will be an integer exponent of the input pulse [20]. If the intensity profile of the input pulse is a square, the potentiation effect for higher order

Optics EXPRESS

sidebands does not alter the intensity profile or duration of the output pulse. In this case, filtering out the n^{th} order sideband produces a square pulse with the same duration as the input pulse, but an extended frequency range. Furthermore, filtering out a sideband for which $n<0$ yields a pulse, where the direction of the chirp is reversed.

3. Experimental setup and results

The experimental setup for temperature measurement with chirped pulses is shown in Fig. 1. A distributed feedback laser (DFB) (CQF938/500, JDS Uniphase) with a linewidth of 1MHz emitting at 193506.25 GHz is periodically modulated by a saw-tooth pattern with a rising edge of 20 ns from a signal generator (8130A, Hewlett Packard). The so-called "bias-T structure" converts the applied electrical modulation to a change in the drive current supplied to the DFB. When the saw-tooth signal periodically increases(decreases) the supplied current, the instantaneous frequency emitted by the DFB is increased(decreased). Figure 1(a) depicts the laser signal at the output of the DFB. In the time domain, the laser signal is a continuous wave (CW) and its power is approximately constant because the change in the drive current is small compared to the total current supplied. The spectrum shown in Fig. 2(b) is measured with an optical spectrum analyzer (OSA) (AP201x, APEX) and has a 5dB width of 746 MHz, indicating that the changing drive current causes the central frequency to vary in this range. The signal generator creating the saw-tooth pattern also generates rectangular signals at a rate of 1 MHz activating a custom solid state optical amplifier (SOA) driver circuit board. When activated by a pulse, this circuit board switches on the SOA (SOA-S-OEC-1550, CIP) allowing it to serve as a gate for pulsing the signal from the DFBs with a duration of 6ns. As illustrated in Fig. 1(b), once the modulation of the DFB and the trigger for the SOA are synchronized, a linearly chirped optical pulse is produced.

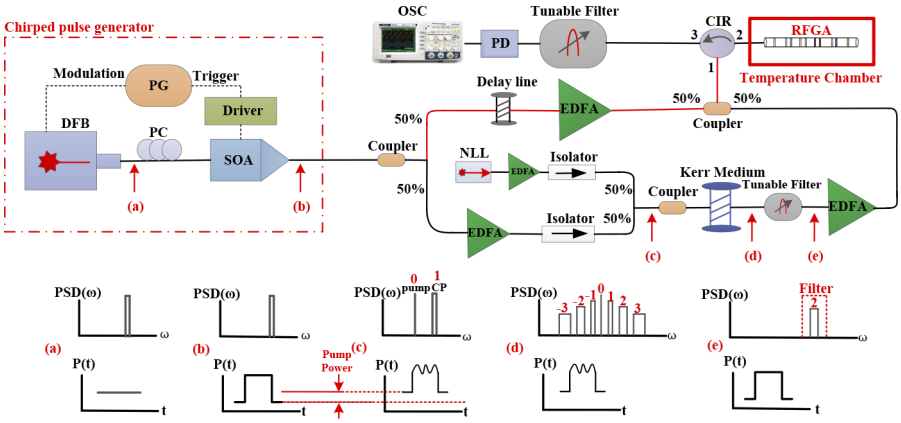

Fig. 1. The experimental setup for applying the Kerr effect to enhance the frequency range of chirped pulses for temperature sensing using CP φ-OTDR. Subfigures (a-e) illustrate the spectrum and signal at successive stages of the setup.

Once generated, the chirped optical pulses are split into two different branches of the setup by a 50:50 coupler. The branch, which sends pulses through a delay line and an erbium doped fiber amplifier (EDFA) (AEDFA-PA-25-B-FA, Amonics) without applying nonlinear chirp extension is marked with a red fiber in Fig. 1. We refer to pulses from this branch as "pure pulses". The delay line ensures that the pure pulses and the pulses generated by the other branch arrive at the RFGA with a 40 ns time delay, allowing for an accurate comparison of their response to changes in temperature.

The pulses in the other branch are first amplified by an EDFA (APEDFA-C-10-B-FA, Amonics) and then sent through an isolator into one input port of a 50:50 coupler. A CW light wave from a

Optics EXPRESS

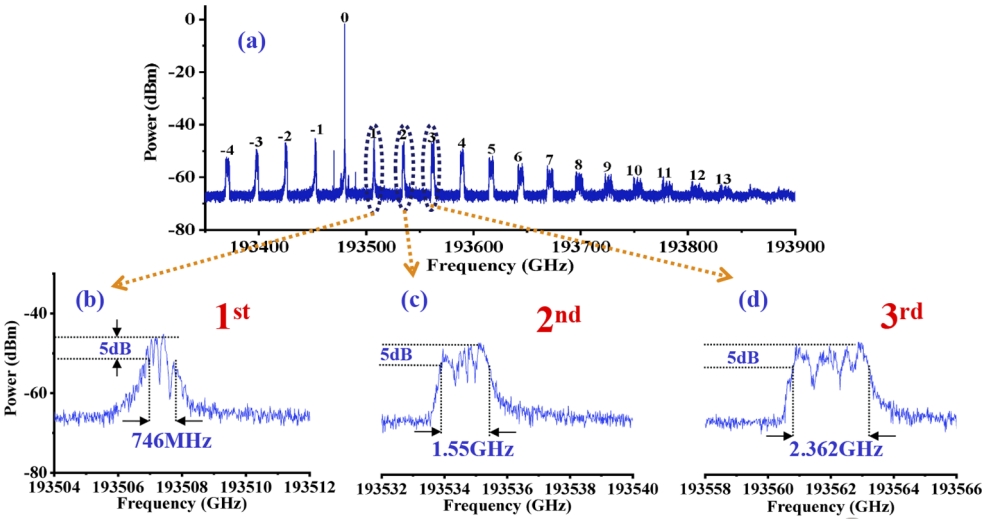

Fig. 2. (a) Measured spectrum after the Kerr medium showing sidebands in the range from $n = -4$ to $n = 13$. Note that $n = 0$ corresponds to the CW pump, while $n = 1$ corresponds to the input chirped pulses. (b-d) Zoom on the first, second and third order sidebands respectively, demonstrating integer scaling of the sweep range.

narrow linewidth laser (NLL) (PS-NLL-1550.12, Teraxion) with a linewidth of 5 kHz emitting at 193480.00 GHz is amplified by an EDFA (AEDFA-33-B-FA, Amonics), passed through an isolator and sent into the other input port of the 50:50 coupler. The chirped pulses and the light from the NLL used as a pump are combined and launched into a highly nonlinear fiber with a non-uniform core referred to as a "Kerr medium" (418SG 04611A, Draka Comteq). The non-uniform core continuously changes the Brillouin frequency of the fiber, which prevents the CW light of the narrow linewidth laser from losing power to Stimulated Brillouin Scattering. The combined spectrum of the chirped pulses and the narrow linewidth laser signal before entering the Kerr medium is visualized in Fig. 1(c). At this stage, the power of the signal in the time domain consists of a constant offset due to CW light from the NLL and a pulse with a sinusoidally varying optical power due to interference. Because of the nonlinear phase modulation caused by the interference of the NLL and the chirped pulses described in Subsection 2.2, frequency sidebands spaced 26.25 GHz apart are generated. Figure 1(d) illustrates three higher order sidebands generated by this process. Figure 2(a) shows a recorded optical spectrum after the Kerr medium with sidebands ranging from -4 to 13. Figures 2(b)-2(d) shows that the chirp range for the n^{th} order sideband is n times the chirp range of the input pulse as predicted in Subsection 2.2. Individual sidebands are extracted using a tunable filter (XTM-50, EXFO). This produces a chirped pulse, referred to as a "Kerr pulse", with a wider chirping range than the pure pulses, but with the same shape and duration.

The extracted Kerr pulses for the n^{th} order sideband are amplified by an EDFA (AEDFA-PA-25-B-FA, Amonics) and recombined with the pure pulses in a 50:50 coupler. They are then launched through a circulator to an RFGA placed inside an insulating, temperature controlled styrofoam box. The RFGA has a reflection coefficient of -30 dB, and a length of 0.8m, which is used to provide a locally enhanced Rayleigh scattering signal. It consists of 8 alternating sub-gratings of lengths 10mm and 5mm respectively. The periods of the sub-gratings are randomly distributed between 0.5180μm and 0.5464μm. The reflected Rayleigh patterns are passed back through the circulator, through a tunable filter (Lambda Commander OSP 9100, Newport) and finally to a

Optics EXPRESS

photodiode (PDB435C, Thorlabs) connected to an oscilloscope (infiniium DSO81204B, Agilent) sampling at 40 GSa/s.

To determine the temperature static measurement range for different Kerr pulses, the heating element inside the styrofoam box is activated, raising the temperature of the RFGA to 40°C. The intensities of the two Rayleigh traces from the pure and Kerr pulses are equalized by adjusting the amplifiers. The heater is then switched off, allowing the RFGA to gradually cool down, causing the Rayleigh traces to shift accordingly. For every 0.1°C step down to 34°C, a Rayleigh trace is recorded. The duration of Rayleigh traces is about 20ns, and the total number of samples for each traces is 800. The oscilloscope is set to average 16 traces to reduce the impact of intensity fluctuation and electrical noise. A custom python script is used to determine the magnitude of the time delays between the traces recorded at different temperatures by numerically calculating the correlation between them. First, pulses for sideband orders from -2 to 6 were used to measure temperature changes in steps of 0.1 °C, demonstrating the feasibility of using higher order sideband pulses. Figure 3 shows the measured time delay as a function of the temperature change for different Kerr pulses in steps of 0.1°C. The slope corresponding to pulses from the n^{th} order sideband is n times smaller than the slope for the pure pulses as predicted in Subsection 2.2. The sign of the slope is negative for sidebands where $n<0$, corresponding to pulses for which the direction of the chirp is reversed.

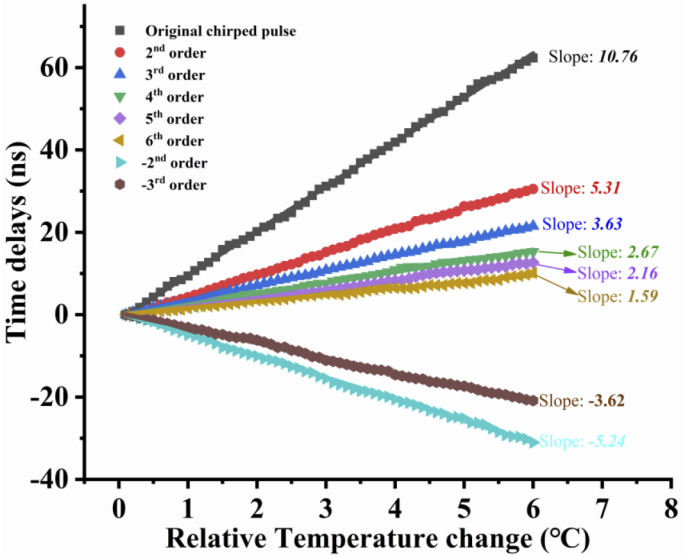

Fig. 3. Time delays of Rayleigh traces corresponding to pure pulses and Kerr pulses for various sideband orders as a function of temperature change. Note that the slope of the n^{th} order sideband is n times smaller than the slope for the pure pulses in agreement with Eq. (5).

Next, the static measurement range of pulses from each sideband order are investigated. Figure 4 depicts the reflected traces from the RFGA before and after the application of a temperature change. For pure pulses with a short chirping range, a temperature change of 0.2°C causes the traces from before and after the change to lose correlation. This is in accordance with Subsection 2.1 where it was predicted, that a short chirping range would imply high sensitivity and low static measurement range. For the 2^{nd} order Kerr pulses, the same temperature change of 0.2°C introduces a smaller time delay due to the extended frequency chirping range. As shown in Fig. 4(f) in which the 6^{th} order Kerr pulses are used, two traces collected before and after a temperature change of 0.6°C remain highly correlated. Recovering the correct time delay between two subsequent traces is not possible for temperature changes that cause the cross correlation

Optics EXPRESS

coefficient to drop below 0.8. For example, when 1^{st} order chirped pulse is used to measure temperature variations of 0.2°C as shown in Fig. 4(b), the coefficient decreases to 0.505. In this case, the demodulation cannot recover the correct time delay, making temperature measurements impossible. Therefore, the largest change in temperature that can be measured between two single shots can be found by determining which temperature shift is required for the traces to decorrelate. The relationship between the cross-correlation coefficient and the temperature variation range for different order Kerr pulses is shown in Fig. 5. Choosing a correlation coefficient of 0.8 as a threshold, it is seen that the static temperature measurement range for the 6^{th} order sideband is improved by a factor 6 compared to the pure pulses.

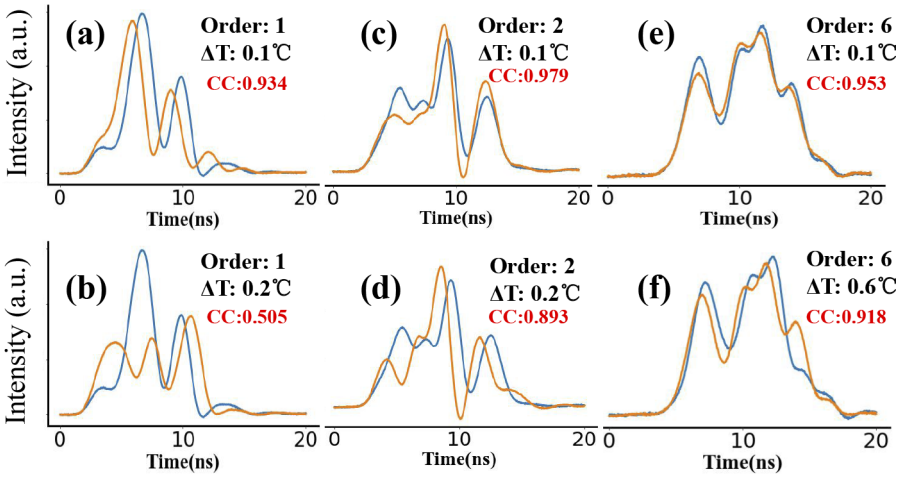

Fig. 4. Measured Rayleigh traces corresponding to various sideband orders before (blue) and after (orange) temperature changes along with their correlation coefficients. (a-b) Traces for pure pulses, (c-d) traces for 2^{nd} order pulses and (e-f) traces for 6^{th} order pulses. CC: Cross-Correlation Coefficient.

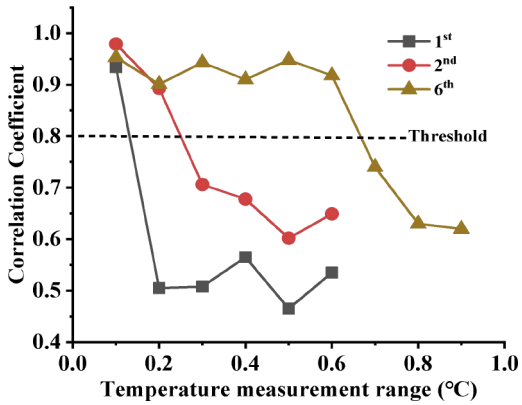

Fig. 5. Cross-Correlation Coefficient of two Rayleigh traces when different temperature changes are applied for sideband orders 1, 2 and 6. Pulses from higher order sidebands remain correlated longer and thus provide enhanced static measurement range.

To investigate how the resolution of the temperature measurements changes when different Kerr pulses are used, 500 Rayleigh traces generated by averaging 16 raw traces are collected at constant room temperature over 0.8s for different orders. Fluctuations in the time delays between

Optics EXPRESS

consecutive pulses are calculated and the equivalent temperature variations are determined using the slopes in Fig. 5. The raw fluctuation data for pure pulses and 6^{th} order Kerr pulses are shown in Fig. 6(a). A histogram of this data is shown in Fig. 6(b). The calculated standard deviation is 2.82 mK for the pure pulses and 25.1 mK for pulses from the 6^{th} order sideband. The temperature measurement precision for different sideband orders is shown in Fig. 6(c). The dashed lines in Fig. 6(c) indicate how the standard deviation of the arrival time and the smallest discernable temperature change should behave in an ideal case. We attribute the discrepancy between the measured resolution and the ideal one to the decreasing Signal to Noise Ratio (SNR) for higher values of n. As mentioned in Subsection 2.2, the power profile of the n^{th} order Kerr pulse will be the power profile of the pure pulse raised to the n^{th} exponent. This potentiation magnifies small power fluctuations and decreases the SNR [21]. Furthermore, the Kerr pulses are affected by power fluctuations for both the input pulses and the amplified NLL used as a pump. The magnified intensity noise causes subsequent traces for higher order sidebands to vary more in shape leading to the larger measured variation in arrival time shown in Fig. 6(c).

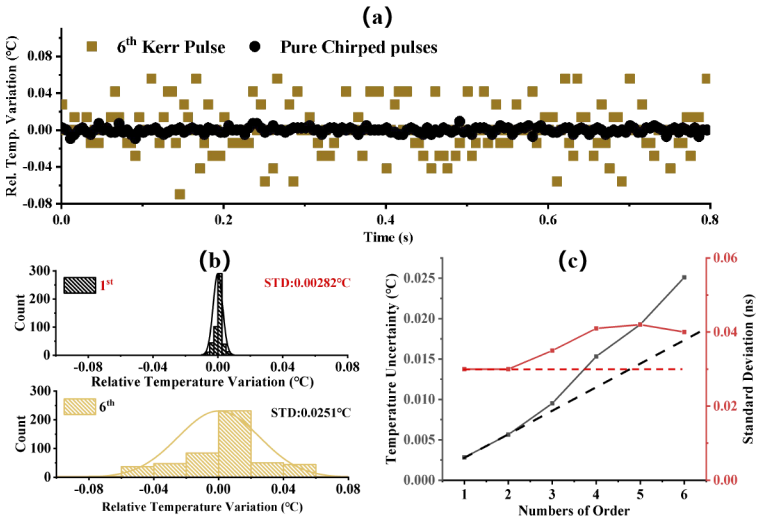

Fig. 6. (a) Temperature measurement uncertainty for pure chirped pulses and 6^{th} order sidebands Kerr pulses within 0.8 seconds when no temperature change is applied.(b) Histogram of the temperature measurement uncertainty for the pure chirped pulses (top) and 6^{th} order Kerr pulses (bottom) and its standard deviation. (c) The standard deviation of measured arrival time and the corresponding uncertainty in measured temperature for sideband orders in the range from 2 to 6. The nonlinear increase in temperature uncertainty for higher orders is attributed to frequency fluctuations in the DFB and NLL being scaled up along with the frequency chirp.

4. Discussion

Several simplifying assumptions are used in modelling the extension of the chirping range. The pure pulses launched into the Kerr medium are assumed to be quasi-CW, which is a valid assumption if the duration of the pulses is much longer than the period of the beat with the CW light from the NLL ($\omega_d \gg 2\pi/W$). In this experiment, the frequency difference of 26.25 GHz implies a beat period of 38 ps, which is much shorter than the pulse duration of 6ns, meaning that the quasi-CW assumption is acceptable. Loss was ignored, and dispersion in the Kerr medium was assumed to be zero. The latter assumption is valid for operation close to the zero-dispersion wavelength, and one can ensure that the sidebands experience similar dispersion

Optics EXPRESS

by making the frequency difference between the input pulses and the CW light from the NLL small. Effects related to the relative polarization of the input pulses and CW light were also ignored. A comprehensive model accounting for all these effects is being researched, but is beyond the scope of this paper.

By calculating the power of each of the sidebands in Eq. (6), and expressing the Bessel functions in terms of their Taylor expansions, it can be shown that their power decreases as $1/(n!)^2$. Thus, utilization of sidebands beyond $n = 6$ is limited by their rapidly decreasing power. Furthermore, because the Kerr effect magnifies power fluctuations, accurately calculating the correlation between traces for sidebands higher than $n = 6$ proved unfeasible. This limitation due to the lasers and amplifiers can be addressed by using more stable devices. To minimize the effect of power fluctuations, one could use a single, highly stable laser to generate both the chirped pulses and the pump. Another way to reduce the impact of intensity fluctuations is to utilize pulse powers that cause the argument of the n^{th} order Bessel function in Eq.(6) to equal its first maximum [22]. In this regime, power fluctuations are attenuated by the Kerr effect. These possibilities will be investigated in future work.

The method described in this paper implies a trade-off between sensitivity and static measurement range for higher order Kerr pulses. However, as the experimental approach demonstrates, it is possible to mitigate this trade-off by using both highly sensitive pure pulses and Kerr pulses with a large static measurement range simultaneously. The extension of chirped pulses described in this work was only applied to a single RFGA, but could be applied to distributed measurements using CP φ-OTDR. More generally, it can be applied to extend the chirping range of pulses in a wide variety of optical systems. For example, the ability to broaden or reverse chirped pulses by all-optical means without altering the pulse duration could be useful in systems relying on Chirped Pulse Amplification [23] or Dispersive Fourier Transforms [24].

5. Conclusion

All-optical chirp extension based on the Kerr effect is demonstrated for sidebands ranging from $n = -3$ to $n = 6$. When applied to a CP φ-OTDR system, the effect allows the measurement range to be scaled up by integer multiples of the sideband number as predicted by theoretical calculations. The chirp extension effect can be applied to existing system relying on chirped pulses to extend their chirping range.

Funding. China Scholarship Council (201808330421); Natural Sciences and Engineering Research Council of Canada (RGPIN-2020-06302, STPGP 506628-17); Canada Research Chairs (950231352).

Disclosures. The authors declare no conflicts of interest.

Data availability. Data underlying the results presented in this paper are not publicly available at this time but may be obtained from the authors upon reasonable request.

References

1. J. P. Dakin, "Distributed optical fiber sensors," in *Distributed and Multiplexed Fiber Optic Sensors II*, vol. 1797 J. P. Dakin and A. D. Kersey, eds., International Society for Optics and Photonics (SPIE, 1993), pp. 76–108.
2. Y. Lu, T. Zhu, L. Chen, and X. Bao, "Distributed vibration sensor based on coherent detection of phase-otdr," J. Lightwave Technol. **28**(22), 3243–3249 (2010).
3. J. C. Juarez, E. W. Maier, K. N. Choi, and H. F. Taylor, "Distributed fiber-optic intrusion sensor system," J. Lightwave Technol. **23**(6), 2081–2087 (2005).
4. S. V. Shatalin, V. N. Treschikov, and A. J. Rogers, "Interferometric optical time-domain reflectometry for distributed optical-fiber sensing," Appl. Opt. **37**(24), 5600–5604 (1998).
5. Y. Dong, X. Chen, E. Liu, C. Fu, H. Zhang, and Z. Lu, "Quantitative measurement of dynamic nanostrain based on a phase-sensitive optical time domain reflectometer," Appl. Opt. **55**(28), 7810–7815 (2016).
6. Z. Wang, L. Zhang, S. Wang, N. Xue, F. Peng, M. Fan, W. Sun, X. Qian, J. Rao, and Y. Rao, "Coherent phase-otdr based on i/q demodulation and homodyne detection," Opt. Express **24**(2), 853–858 (2016).
7. A. E. Alekseev, V. S. Vdovenko, B. G. Gorshkov, V. T. Potapov, and D. E. Simikin, "A phase-sensitive optical time-domain reflectometer with dual-pulse diverse frequency probe signal," Laser Phys. **25**(6), 065101 (2015).

Optics EXPRESS

8. G. Fang, T. Xu, S. Feng, and F. Li, "Phase-sensitive optical time domain reflectometer based on phase-generated carrier algorithm," J. Lightwave Technol. **33**(13), 2811–2816 (2015).
9. J. Pastor-Graells, H. F. Martins, A. Garcia-Ruiz, S. Martin-Lopez, and M. Gonzalez-Herraez, "Single-shot distributed temperature and strain tracking using direct detection phase-sensitive otdr with chirped pulses," Opt. Express **24**(12), 13121–13133 (2016).
10. Y. Wang, P. Lu, S. Mihailov, L. Chen, and X. Bao, "Distributed time delay sensing in a random fiber grating array based on chirped pulse ϕ-otdr," Opt. Lett. **45**(13), 3423–3426 (2020).
11. Y. Wang, P. Lu, S. Mihailov, L. Chen, and X. Bao, "Ultra-low frequency dynamic strain detection with laser frequency drifting compensation based on a random fiber grating array," Opt. Lett. **46**(4), 789–792 (2021).
12. Y. Wang, P. Lu, S. Mihailov, L. Chen, and X. Bao, "Strain measurement range enhanced chirped pulse ϕ-otdr for distributed static and dynamic strain measurement based on random fiber grating array," Opt. Lett. **45**(21), 6110–6113 (2020).
13. B. Vanus, C. Baker, L. Chen, and X. Bao, "High extinction ratio optical pulse characterization method via single-photon counting," Appl. Opt. **60**(1), 20–23 (2021).
14. O. Krarup, C. Baker, L. Chen, and X. Bao, "Nonlinear resolution enhancement of an fbg based temperature sensor using the kerr effect," Opt. Express **28**(26), 39181–39188 (2020).
15. B. Wang, X. Fan, S. Wang, J. Du, and Z. He, "Millimeter-resolution long-range ofdr using ultra-linearly 100 ghz-swept optical source realized by injection-locking technique and cascaded fwm process," Opt. Express **25**(4), 3514–3524 (2017).
16. J. Du and Z. He, "Sensitivity enhanced strain and temperature measurements based on fbg and frequency chirp magnification," Opt. Express **21**(22), 27111–27118 (2013).
17. A. Boskovic, S. V. Chernikov, J. R. Taylor, L. Gruner-Nielsen, and O. A. Levring, "Direct continuous-wave measurement of n2 in various types of telecommunication fiber at 1.55 μm," Opt. Lett. **21**(24), 1966–1968 (1996).
18. G. Agrawal, "Chapter 4 - self-phase modulation," in *Nonlinear Fiber Optics (Fifth Edition)*, G. Agrawal, ed. (Academic Press, Boston, 2013), Optics and Photonics, pp. 87–128, fifth edition ed.
19. "NIST Digital Library of Mathematical Functions," http://dlmf.nist.gov/10.12, Release 1.0.27 of 2020-06-15. F. W. J. Olver, A. B. Olde Daalhuis, D. W. Lozier, B. I. Schneider, R. F. Boisvert, C. W. Clark, B. R. Miller, B. V. Saunders, H. S. Cohl, and M. A. McClain, eds.
20. "NIST Digital Library of Mathematical Functions," http://dlmf.nist.gov/10.7.E3, Release 1.0.27 of 2020-06-15. F. W. J. Olver, A. B. Olde Daalhuis, D. W. Lozier, B. I. Schneider, R. F. Boisvert, C. W. Clark, B. R. Miller, B. V. Saunders, H. S. Cohl, and M. A. McClain, eds.
21. B. Vanus, C. Baker, L. Chen, and X. Bao, "All-optical intensity fluctuation magnification using kerr effect," Opt. Express **28**(3), 3789–3794 (2020).
22. B. Vanus, C. Baker, L. Chen, and X. Bao, "All-optical pulse peak power stabilization and its impact in phase-otdr vibration detection," OSA Continuum **4**(5), 1430–1436 (2021).
23. D. Strickland and G. Mourou, "Compression of amplified chirped optical pulses," Opt. Commun. **56**(3), 219–221 (1985).
24. S. Sanders, "Wavelength-agile fiber laser using group-velocity dispersion of pulsed super-continua and application to broadband absorption spectroscopy," Appl. Phys. B **75**(6-7), 799–802 (2002).

Chapter 6

Sensitivity Enhancement

The contributions of the four authors to the paper titled "Sensitivity enhancement of fiber optical polarimetric sensors using self-induced nonlinear phase modulation via the Kerr effect", published in Optics Express [93], are as follows. The present author derived the model for the dependence of sideband power on the polarization of the input lasers, built the setup, acquired and presented the data and wrote the bulk of the text. Dr. Chams Baker provided advice throughout the experimental process and suggested the use of a metal cantilever as a polarimetric sensor. He, along with prof. Liang Chen and Prof. Xiaoyi Bao, also delivered helpful critique and feedback on what experimental evidence would corroborate the theoretical model and on the writing of the paper.

The two goals of the experiment presented in this paper are respectively to establish the validity of the theoretical analysis presented in Section 3.5 and fully derived in Section 6.1, and to exploit the dependence of higher order sidebands on changes in polarization to enhance the sensitivity of a polarimetric sensor. The first goal of validating the model was achieved by theoretically deriving the ratio of the sideband power measured for a range of input polarizations to the power measured for co-polarized input lasers. The values of this ratio was then measured experimentally and compared to theoretical calculations and a numerical simulation as shown in Fig. 4 of the paper. The second goal was achieved using a sensor, which exploits, that bends in a metal cantilever to which a polarization maintaining fiber is attached, cause changes in the birefringence in the fiber and thus the polarization of light travelling within. This sensor was chosen for its conceptual simplicity and because the signal it produces can easily be interrogated using both the Kerr effect and a conventional polarizer obeying Eq. 2.36.

Practical applications of polarimetric sensing include monitoring magnetic fields produced by prototype fusion reactors [94], and measuring the deformation of air-

craft wings to which the cantilever sensor employed in the present experiment is an analogue [95]. A physical limitation of the method described in this paper is the presence of wavelength dependent randomly varying birefringence in the nonlinear medium, which causes the SOPs of the signal and reference lasers to drift relative to each other as they propagate down the fiber. Thus, sideband power will be observed even if the two SOPs are orthogonal. To mitigate this effect, one can shorten the Kerr medium and compensate for the reduction in ϕ_{NL} by increasing the powers of the signal and reference laser pulses.

Research Article | Vol. 30, No. 9 / 25 Apr 2022 / Optics Express 13985
Optics EXPRESS

Sensitivity enhancement of fiber optical polarimetric sensors using self-induced nonlinear phase modulation via the Kerr effect

OLE KRARUP,* CHAMS BAKER, LIANG CHEN, AND XIAOYI BAO

Fiber Optics Group, Department of Physics, University of Ottawa, Ottawa, Canada K1N 6N5, Canada

Abstract: This work presents an analytical model accounting for the impact of optical polarization on the generation of frequency sidebands by the Kerr effect in a highly nonlinear fiber. Theoretical analysis shows that for a relative polarization angle, α, between two input lasers expressed on the Poincaré sphere, the optical power of the n^{th} order sideband is proportional to $\cos^{2n}(\alpha/2)$. This theoretical result enables a novel all-optical technique for interrogating changes in polarization with higher sensitivity than conventional measurement schemes using linear polarizers. The predicted theoretical relationship between the sideband power and the relative polarization angle is verified experimentally and sensitivity enhancement by a factor of 1.45 compared to a conventional polarimetric sensor is demonstrated for the 3rd order sideband. This novel nonlinear approach, which allows dynamic range to be traded for an enhanced ability to detect small polarization variations, has potential applications in fusion reactor monitoring, instrumentation and material characterization.

1. Introduction

For environmental sensing, systems relying on optical fibers have a number of advantages compared to electrical devices. Apart from speed, durability and immunity to electromagnetic interference, optical fibers allow for novel sensing schemes based on the polarization of light. Various environmental perturbations can be detected as they affect the birefringence in optical fibers, leading to measurable changes in the state of polarization of light propagating within. Examples of such sensing schemes include polarization optical time domain reflectometry (P-OTDR) [1] and magnetic field sensing using the Faraday effect [2], which has been applied to detect electrical current variations on the order of 1 mA [3]. When incident polarized light has an angle θ with the axis of a polarizer, the output intensity follows Malus' law [4], $I = I_0 \cos^2(\theta)$, where I_0 is the incident intensity, and the sensitivity is $dI/d\theta = -I_0 \sin(2\theta)$ with an extremum at $\theta = 45°$. If a hypothetical optical system could cause the detected intensity to follow the relation $I = I_0 \cos^{2n}(\theta)$, the maximum sensitivity is increased by a factor

$$\epsilon_n = \frac{2n}{\sqrt{2n-1} \cdot \left(1 + \frac{1}{(2n-1)}\right)^n} \tag{1}$$

at $\theta = \arctan((2n-1)^{-1/2})$. For example, when $n = 3$, maximum sensitivity is achieved at $\theta = 24.1°$ and is approximately 1.55 times greater than for the $n = 1$ case corresponding to Malus' law.

All-optical signal processing refers to techniques for manipulating the wavelength, polarization, phase and amplitude of signals using nonlinear effects. Such methods have been employed to enhance optical signals used in telecommunication [5], to amplify weak signals [6], and to generate supercontinuum light [7]. Compared to linear processing methods, all-optical signal processing approaches utilizing the Kerr effect enable improved performance of fiber based

#454492 https://doi.org/10.1364/OE.454492
Journal © 2022 Received 23 Jan 2022; revised 28 Mar 2022; accepted 30 Mar 2022; published 11 Apr 2022

Optics EXPRESS

environmental sensors. When two frequencies of light are launched into a highly nonlinear optical fiber, frequency sidebands are generated. The powers of the sidebands are proportional to integer exponents of the input powers, which has been exploited to improve the extinction ratio of pulses in OTDR, resulting in an enhanced signal to noise ratio (SNR) [8]. The power dependence of the sidebands has also been utilized to magnify small power fluctuations [9], stabilize signals to reduce intensity noise [10], and to enhance the resolution of a fiber Bragg grating (FBG) based temperature sensor [11]. Furthermore, if the frequency difference between two lasers launched into a Kerr medium is increased by $\Delta\omega$, the n^{th} order sideband will shift by $n\Delta\omega$, thereby extending the laser sweeping range. This sweep extension has been applied to enhance the resolution of optical frequency domain reflectometry (OFDR) and to improve the sensitivity of an FBG used for strain sensing [12–14]. It has also been used to enhance the frequency sweeping rate of signals used in chirped-pulse phase-OTDR (CP ϕ-OTDR), extending the sensing range of single-shot measurements [15]. None of these models include the effects of polarization on the powers of the generated sidebands and results indicate that ignoring polarization is only valid if the incident lasers are co-polarized. A detailed theoretical model describing how sideband generation via the Kerr effect depends on polarization would lead to a deeper understanding of the underlying physics and enable novel sensing schemes.

In this paper, we propose a fully analytical model for calculating the polarization dependence of the powers of frequency sidebands generated by the Kerr effect. Theoretical and experimental results show that when birefringence in the nonlinear medium can be ignored, the power of the frequency sidebands as a function of incident polarization follows a simple analytical expression. The polarization dependence of the sideband power is experimentally exploited to increase the sensitivity of a polarimetric sensor by a factor of 1.45 for the 3rd order sideband. Finally, limitations of the presented analytical model are discussed along with potential applications to existing polarization based sensors.

2. Theory

A detailed derivation of the following results is presented in Supplement 1. Launching lasers at two different angular frequencies, ω_r and ω_s with $\omega_r<\omega_s$, into an optical fiber with a length, L, and a waveguide nonlinearity parameter, γ, the electric field amplitude at the input is given by

$$|A_{in}\rangle = \sqrt{P_r}\begin{pmatrix}\cos\theta\\ \sin\theta e^{i\phi}\end{pmatrix}e^{i\delta}e^{-i0.5\omega_d t} + \sqrt{P_s}\begin{pmatrix}\cos\beta\\ \sin\beta e^{i\xi}\end{pmatrix}e^{i0.5\omega_d t}, \tag{2}$$

where P_r and P_s are respectively the powers of the reference and the signal, $\omega_d = \omega_s - \omega_r$, θ and β are respectively the angles of the polarization vectors relative to the x-axis for the reference and the signal, ϕ and ξ are respectively the phase differences between the orthogonal polarization components of the fields for the reference and the signal, while δ is a phase delay between the two lasers. Computing the power of the input field yields $\langle A_{in}|A_{in}\rangle = P_r + P_s + 2\sqrt{P_r P_s}\cos(\alpha/2)\cos(\omega_d t + k)$, where k is a phase factor, which depends on the values of θ, β, ϕ, ξ and δ, while α is the angle between the reference and signal fields when represented as vectors on the Poincaré sphere as visualized in Fig. 1(a).

Neglecting dispersion, attenuation and random birefringence along the fiber, the Nonlinear Schrödinger Equation (NLSE) reduces to $\partial_z|A(z)\rangle = i\gamma\langle A|A\rangle|A(z)\rangle$, which is solved analytically to obtain an expression for the field amplitude at the output of the fiber, $|A_{out}\rangle = |A_{in}\rangle \exp(i\gamma L(P_r + P_s))\exp(i2\gamma L\sqrt{P_r P_s}\cos(\alpha/2)\cos(\omega_d t + k))$. Applying the Jacobi-Anger expansion [16,17], the output field is expressed as an infinite sum of frequency sidebands spaced $\omega_d/2\pi$ apart, and is

Optics EXPRESS

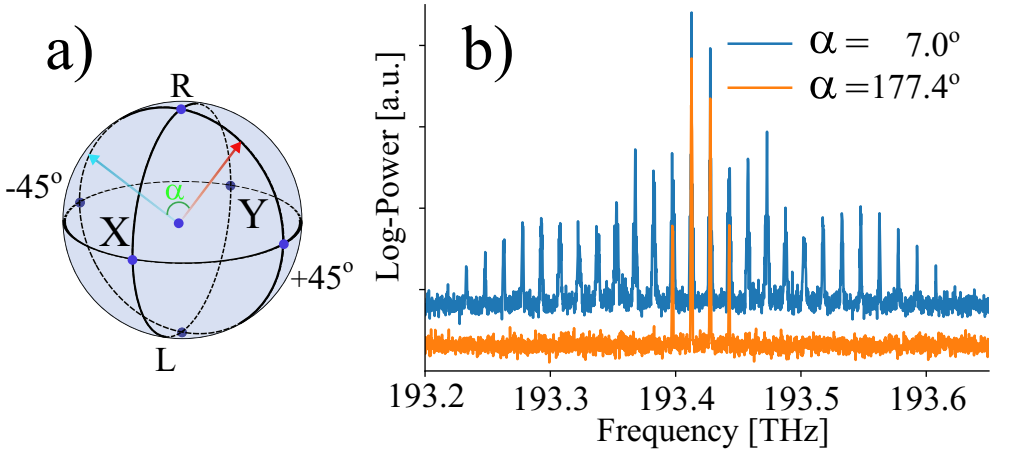

Fig. 1. (a) The polarizations of the lasers in Eq. (2) represented on the Poincaré sphere. If their relative angle, α, is zero, the two lasers are co-polarized. For $\alpha = 180°$, the polarizations of the two lasers are orthogonal, which prevents them from interfering and generating sidebands. (b) Optical spectra recorded after the Kerr medium for reference and signal pulses that are almost completely copolarized (blue) and ones that are almost completely orthogonal (orange). Traces have been vertically offset for clarity.

given by $|A_{out}\rangle = \exp\left(i\gamma L(P_r + P_s)\right) \sum_{n=-\infty}^{\infty} i^n e^{ink} e^{i(n+0.5)\omega_d t} |A_n\rangle$, where

$$|A_n\rangle = \left[\begin{pmatrix} i\sqrt{P_r}\cos\theta e^{i(\delta+k)} J_{n+1}(\phi_{\mathrm{NL}}) + \sqrt{P_s}\cos\beta J_n(\phi_{\mathrm{NL}}) \\ i\sqrt{P_r}\sin\theta e^{i\phi} e^{i(\delta+k)} J_{n+1}(\phi_{\mathrm{NL}}) + \sqrt{P_s}\sin\beta e^{i\xi} J_n(\phi_{\mathrm{NL}}) \end{pmatrix}\right], \tag{3}$$

and $\phi_{\mathrm{NL}} = 2\gamma L\sqrt{P_r P_s}\cos(\alpha/2)$. The subscript $n = -1$ corresponds to the frequency component at $\omega_r/2\pi$, while $n = 0$ corresponds to the frequency component at $\omega_s/2\pi$. The power of the n^{th} order sideband is $\langle A_n|A_n\rangle = P_r J_{n+1}^2(\phi_{\mathrm{NL}}) + P_s J_n^2(\phi_{\mathrm{NL}})$, which implies that the powers of the sidebands at the output of the fiber depend on the initial angle, α. Introducing the normalization, $x = \gamma L P_s$, $y = \gamma L P_r$, $z_n = \gamma L\langle A_n|A_n\rangle$, and applying the asymptotic approximation of the Bessel functions for $n>0$ and $0<\phi_{\mathrm{NL}}<\sqrt{1+n}$, the power of the n^{th} order sideband is

$$z_n \approx \frac{x^n y^{n+1}}{[n!]^2}\cos^{2n}(\alpha/2), \tag{4}$$

implying that the power of the n^{th} order sideband decreases as α increases towards its maximum value of 180°. Defining $z_n^{(max)} = z_n(\alpha = 0)$ and $z_n^{(min)} = z_n(\alpha)$, the ratio of these two quantities for the n^{th} order sideband is

$$r_n(\alpha) = \frac{z_n^{(min)}}{z_n^{(max)}} = \cos^{2n}(\alpha/2) = r_1^n(\alpha). \tag{5}$$

Thus, if the angle between the reference and signal is changed from 0 to α, the ratio of minimum power to maximum power will be smaller for higher order sidebands.

3. Experimental setup and results

The experimental setup used for investigating the enhanced response to variations in relative polarization is presented in Fig. 2(a). The temporal power and the power spectral density

Optics EXPRESS

(PSD) of the light at different points along the optical path are illustrated in Figs. 2(b-e). A laser (NLL:PS-NLL-1550.12, Teraxion) with a linewidth of 5 kHz emitting at 193412.72 GHz (1550.014 nm) is aligned to a linear polarizer (POL1) ensuring light propagation in only one of the polarization axes of an electro-optical modulator (EOM1, MXPE-LN-10, Photline) that is driven by an arbitrary waveform generator (AFG 3252, Tektronix) to obtain optical pulses with a duration of 4 ns. Nanosecond pulses are utilized instead of a continuous wave laser to suppress the effect of stimulated Brillouin scattering (SBS) on subsequent all-optical signal processing and measurements. Using a 50:50 coupler, the laser pulses are split into two branches: the signal branch and the reference branch. Pulses in the signal branch are polarized by POL2 and amplified using a polarization maintaining erbium doped fiber amplifier (PM-EDFA, EDFA100P, THORLABS). The signal is then sinusoidally modulated using EOM2 (OC-192, JDS UNIPHASE) driven at a frequency of 12 GHz by an electronic radio frequency source (83752A, Hewlett Packard) to generate two new frequency components located at 193400.72 GHz (1550.110 nm) and 193424.72 GHz (1549.918 nm). A 3 GHz bandpass filter (BPF1, TFC 3GHz, TeraXion) extracts the frequency component at 193424.72 GHz (1549.918 nm), which is amplified using a high power EDFA (HP-EDFA1, APEDFA-C-10-B-FA, Amonics) and passed through BPF2 (TB9 Optical Grating Filter, JDS Uniphase). POL3 then realigns the polarization of the pulses in case of power dependent polarization rotation in HP-EDFA1. The signal pulses are subsequently passed through a polarization modulator (POM, Corning PC-410), which is driven by a square waveform with a period of 4 s and an adjustable peak voltage from the arbitrary waveform generator, thereby modulating the polarization of the signal. The signal passes through PC1 followed by a 50:50 coupler where one arm leads to a shutter (SH1) which remains closed, while the other arm connects to a second coupler (C1) combining the signal pulses with pulses from the reference branch.

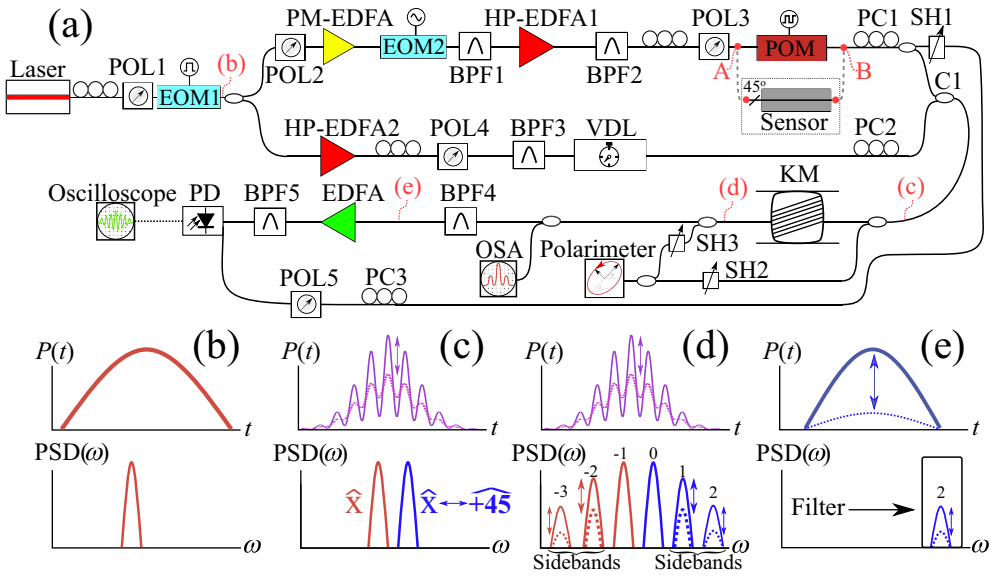

Fig. 2. (a) The experimental setup used for investigating the dependence of frequency sideband generation via the Kerr effect on polarization. (b-e): The light in the time- and angular frequency domains at different points along the optical path. Modulating the polarization of the signal pulses away from a state of co-polarization with the reference pulses reduces the power of the higher order sidebands according to Eq. (5).

Optics EXPRESS

Pulses in the reference branch, are amplified by HP-EDFA2 (AEDFA-33B-FA, Amonics) and have their polarization realigned by POL4 in case of power dependent polarization rotation in the amplifier. The pulses are filtered by BPF3 (Ultra Narrow Filter, AOS) and then passed through a variable delay line (VDL, MDL-002, General Photonics) followed by PC2 and C1. The time delay introduced by the VDL is adjusted to ensure that the reference- and signal pulses arrive at C1 simultaneously.

A small portion of the combined signal and reference pulses is extracted by a coupler and sent through an open SH2 to a polarimeter (IPM5300, THORLABS). By turning on the reference- and signal pulses individually, their polarizations can be adjusted using PC1 and PC2 to coincide when a 0V signal is applied to the POM. The combined signal and reference pulses propagate through a Kerr medium (KM) consisting of a 5.7 km highly nonlinear fiber (418SG 04611A, Draka Comteq). SH2 is closed and a portion of the output of the Kerr medium is extracted and sent through SH3 to the polarimeter. By turning on the initially copolarized reference and signal pulses individually, the polarimeter measures the change in α induced by wavelength dependent, randomly varying birefringence along the Kerr medium. Launching the co-polarized signal- and reference pulses into the Kerr medium individually with several different choices of polarization states, their relative angle on the Poincaré sphere at the output of the Kerr medium remains below 8.58°. When light propagates in a medium with randomly varying birefringence, the state of polarization changes with a beat length of $L_B = \lambda/|n_x - n_y|$. Assuming $|n_x - n_y| = 10^{-7}$, which is a typical average value for the local birefringence in commercially available single mode fibers [18], the beat lengths for the reference- and signal pulses are 15.50014 m and 15.49918 m respectively, implying that they have undergone 367.739 and 367.761 beat cycles respectively at the end of the 5.7 km Kerr medium. Such an estimated drift of $(367.761 - 367.739) \cdot 100\% = 2.2\%$ of a beat cycle between the signal and reference pulses corresponds to a relative angle on the Poincaré sphere of $360° \cdot 0.022 = 7.92°$, which is comparable to the experimentally measured maximum drift of 8.58°. Because the maximum drift of 2.2% is relatively small, the impact of wavelength dependent randomly varying birefringence on light propagating in the Kerr medium can safely be ignored.

The spectrum of the output of the Kerr medium is measured using an optical spectrum analyzer (OSA, AP2043B, APEX). Two spectra measured with identical reference- and signal powers, but different relative polarizations, are presented in Fig. 1(b). The measured spectra show that propagation in the Kerr medium leads to the generation of sidebands due to self-induced nonlinear phase modulation and that the power of generated sidebands depends on α. The output of the Kerr medium then passes through BPF4 (XTM-50, EXFO), which extracts the n^{th} order sideband. This sideband signal is amplified by an EDFA (AEDFA-PA-25-B-FA, Amonics), passed through BPF5 (TFC 3GHz, TeraXion) to eliminate residual ASE noise from the amplifier and finally detected by a photodiode (PD, Model 1592 3.5 GHz, New Focus). The PD is connected to an oscilloscope (infiniium DSO81204B, Agilent) sampling at 20 GSa/s and averaging 16 traces to reduce the impact of optical intensity fluctuations and electrical noise.

SH2 is opened, and the input angle on the Poincaré sphere between the reference and signal pulses is recorded for a range of voltages applied to the POM. BPF4 and BPF5 are adjusted to extract each sideband, and the oscilloscope is programmed to record the traces with the highest and lowest intensity. In Fig. 3, measurements for $n = 1$ to $n = 5$ of the maximum trace corresponding to $\alpha = 0°$ is shown in blue along with the minimum traces corresponding to $\alpha = 57.93°$ in orange. The traces have been normalized to the peak power of the maximum trace. The theoretical ratio of the minimum trace to the maximum trace calculated using Eq. (5) is plotted in green, showing close agreement with experimental results. Figure 4 presents the measured and analytically calculated ratios for sidebands 1 through 5 and maximum angles ranging from 21.53° to 63.50°. Figure 4 also presents ratios calculated numerically by solving the NLSE using the Split Step Fourier Method in the presence of randomly varying birefringence [19,20], and the

Optics EXPRESS

ratio for the first order sideband raised to the n^{th} integer power. The experimentally measured ratios agree well with the analytically and numerically calculated values, confirming the validity of Eq. (5). Discrepancies between theoretical and experimental ratios arise from electrical noise and fluctuations in the optical power of the recorded traces. As described in other works on sideband generation, extracting pulses from higher order sidebands effectively magnifies their intensity noise causing inaccuracies in the measured maximum and minimum traces [9,15].

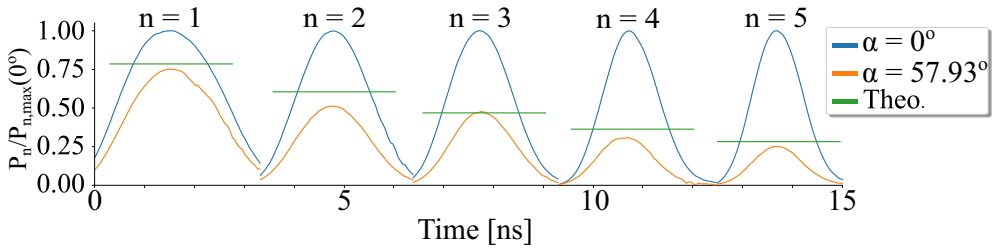

Fig. 3. Experimental measurements of the maximum and minimum traces acquired by varying α from 0° to 57.93°. The measured power has been normalized to the peak power of the maximum trace corresponding to $\alpha = 0°$.

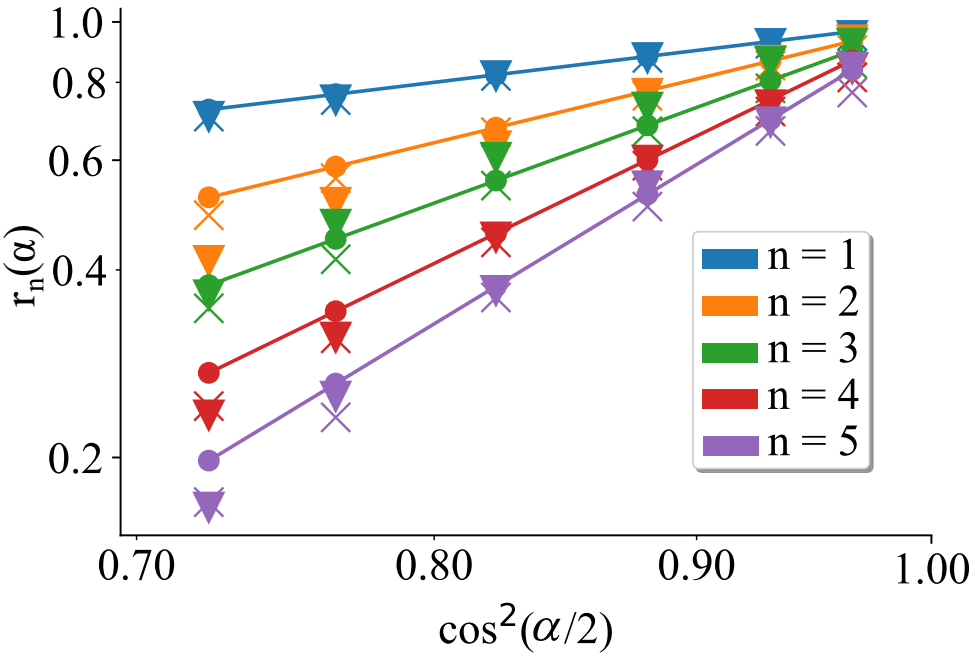

Fig. 4. Double logarithmic plot of the ratio in Eq. (5) for different sidebands and α values in the range from 21.53° to 63.50°. Straight lines (−): Analytically calculated ratio obtained using $\cos^{2n}(\alpha/2)$. Circles (○): Ratio according to numerical simulation. Triangles (▽): Experimentally determined ratio. Crosses (×): Experimental ratio for r_1 raised to the n^{th} power.

The practical utility of polarization sensitivity enhancement using higher order sidebands is demonstrated by combining this effect with a polarimetric sensor. The POM is detached from the connectors labelled A and B in Fig. 2(a) and replaced with a polarimetric sensor consisting of a

Optics EXPRESS

PM fiber spliced at a 45° angle with the output of POL3. The PM fiber under test (FUT) is glued to a metal cantilever to which weights can be attached. When polarized pulses from POL3 reach the FUT, the incoming light is split evenly between the fast and slow axes. As the signal pulses travel through the polarimetric sensor, the accumulated phase shift between light in the fast and slow axes causes the state of polarization to alternate between linear and circular. Bending the cantilever by applying weight induces strain in the FUT and alters the phases accumulated by light travelling along the fast and slow axes, which changes the polarization state of light at the end of the FUT. SH1 is opened and PC3 aligns the principal axis of the FUT at a 45° angle with the polarization axis of POL5, producing a raw signal whose peak power varies according to Malus' law. A static delay line ensures that the processed signal and the raw signal arrive at the PD with a time delay that allows them to be captured in the same oscilloscope trace. PC2 is adjusted such that variations in the polarization of the signal pulse lead to maximum variation in the power of the sidebands. Subsequently, the peak powers of the raw- and sideband signals are equalized, enabling a direct comparison of their responses to a change in polarization caused by increased weight on the cantilever. Adding identical 4 g weights, each applying a force of ~ 40 mN, to the end of the cantilever changes the power of the raw signal and the signal generated by extracting the 3rd order sideband as presented in Fig. 5(a). Recording the peak power as a function of applied weight as presented in Fig. 5(b) shows that the raw signal follows Malus' law, while the enhanced signal follows cosine to the 6th power in agreement with Eq. (4). Furthermore, the maximum slope for the enhanced signal is 1.45 times larger than the slope for the raw signal in agreement with the value of 1.55 predicted by Eq. (1), demonstrating sensitivity enhancement in a practical application. The curve for the raw signal is approximately linear over a range of 400 mN, while the curve for the enhanced signal is approximately linear in a 200 mN range, which illustrates the trade-off between sensitivity and dynamic range.

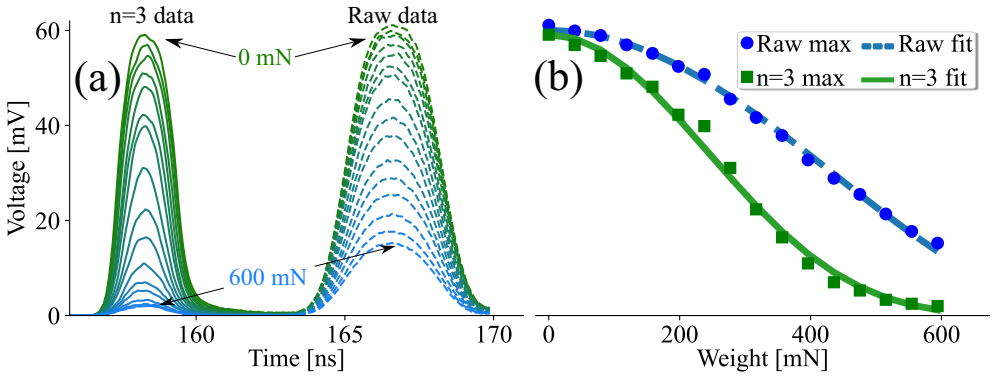

Fig. 5. (a) Oscilloscope data showing the power of the raw signal from a conventional polarimetric sensor (right) and enhanced measurements from the 3rd order sideband (left) as the weight applied at the end of the cantilever is increased from 0 to 600 mN in steps of 40 mN. The enhanced signal shows a greater change in voltage per applied weight than the raw signal, indicating enhanced sensitivity to changes in polarization. (b) Peak voltage of the two signals versus applied weight. The curve for the raw signal follows the square of the cosine of the applied weight while the curve for the 3rd order sideband follows cosine to the 6th power as predicted by Eq. (4).

4. Discussion

A number of simplifications are used in the analytical model for polarization dependent sideband generation via the Kerr effect. The presented model ignores the impact of attenuation in the

Optics EXPRESS

Kerr medium, which in the general case can be accounted for by replacing the length of the fiber with an effective length, $L_{\text{eff}} = [1 - \exp(-\alpha_L L)]/\alpha_L$, where α_L is the loss coefficient. The presented model also ignores the impact of chromatic dispersion, which is justifiable when the dispersion length is much greater than the nonlinear length. The dispersion length is given by $L_D = 2\pi c T_0^2/\lambda^2 D$, where c is the speed of light in vacuum, T_0 is the pulse duration, λ is the central wavelength and D is the chromatic dispersion. Using $T_0 = 2\pi/(4\omega_d) = 20.75$ ps corresponding to the full width at half maximum within one cycle of the interference signal, $\lambda = 1550$ nm and $D = 3$ ps/(nm·km) as reported in [21] leads to $L_D = 112.5$ km. In contrast, the nonlinear length is given by $L_{\text{NL}} = 1/\gamma P$ with γ being the waveguide nonlinearity parameter and P being the peak power. The present model is valid for $0 < \phi_{\text{NL}} < \sqrt{1+n}$ and using $\phi_{\text{NL}} = 2\gamma LP$, where $P = \sqrt{P_r P_s}$, while operating under the condition $\phi_{\text{NL}} < 1$ leads to $L_{\text{NL}} \approx 2L \approx 11.4$ km. Because $L_D \gg L_{\text{NL}}$, the assumption of negligible chromatic dispersion underlying the analytical model is valid in the presented experiment.

The enhanced sensitivity to changes in polarization for higher order sidebands can be used for improving existing polarimetric sensing systems. Examples include polarization-OTDR, which has been used for measuring magnetic fields generated by prototype fusion reactors [22]. Equation (3) also enables the calculation of the state of polarization of the n^{th} order sideband. Because the polarization of the n^{th} order sideband is a function of the input power, which varies with time for non-square pulses, extracting higher order sidebands produces pulses with time dependent states of polarization. The generation of such pulses, which is a topic of ongoing research, could be used to analyze the properties of material surfaces [23]. Another potential application exploits the dependence of sideband power on relative polarization to build an all-optical polarimeter without the need for physical polarizers or waveplates for detection. Such applications will be explored in future work.

5. Conclusion

Enhancement of the sensitivity to changes in polarization based on the Kerr effect is demonstrated for sidebands up to $n = 5$. This all-optical signal processing approach is combined with a polarimetric sensor to achieve a sensitivity improvement by a factor 1.45 for the 3rd order sideband. The theoretical model provides an analytical expression that agrees with experimental results. The technique can be applied to existing systems measuring changes in relative polarization to improve measurement sensitivity.

Funding. Canada Research Chairs (75-67138); Natural Sciences and Engineering Research Council of Canada (DG-2020-06302).

Disclosures. The authors declare no conflicts of interest.

Data Availability. Data underlying the results presented in this paper are available in Ref. [24].

Supplemental document. See Supplement 1 for supporting content.

References

1. A. J. Rogers, "Polarization-optical time domain reflectometry: a technique for the measurement of field distributions," Appl. Opt. **20**(6), 1060–1074 (1981).
2. R. H. Stolen and E. H. Turner, "Faraday rotation in highly birefringent optical fibers," Appl. Opt. **19**(6), 842–845 (1980).
3. H. Zhang, Y. Dong, J. Leeson, L. Chen, and X. Bao, "High sensitivity optical fiber current sensor based on polarization diversity and a faraday rotation mirror cavity," Appl. Opt. **50**(6), 924–929 (2011).
4. M. Étienne Louis, "Mémoire sur la mesure du pouvoir réfringent des corps opaques," in *Bulletin de la Société philomathique de Pari*, vol. 1-11 (Société philomathique de Paris, Paris, 1826), pp. 77–81, 6th ed.
5. A. E. Willner, S. Khaleghi, M. R. Chitgarha, and O. F. Yilmaz, "All-optical signal processing," J. Lightwave Technol. **32**(4), 660–680 (2014).
6. C. J. McKinstrie, S. Radic, and A. H. Gnauck, "All-optical signal processing byfiber-based parametric devices," Opt. Photonics News **18**(3), 34–40 (2007).
7. G. Moille, E. F. Perez, J. R. Stone, A. Rao, X. Lu, T. S. Rahman, Y. K. Chembo, and K. Srinivasan, "Ultra-broadband Kerr microcomb through soliton spectral translation," Nat. Commun. **12**(1), 7275 (2021).

Optics EXPRESS

8. B. Vanus, C. Baker, L. Chen, and X. Bao, "High extinction ratio optical pulse characterization method via single-photon counting," Appl. Opt. **60**(1), 20–23 (2021).
9. B. Vanus, C. Baker, L. Chen, and X. Bao, "All-optical intensity fluctuation magnification using kerr effect," Opt. Express **28**(3), 3789–3794 (2020).
10. B. Vanus, C. Baker, L. Chen, and X. Bao, "All-optical pulse peak power stabilization and its impact in phase-otdr vibration detection," OSA Continuum **4**(5), 1430–1436 (2021).
11. O. Krarup, C. Baker, L. Chen, and X. Bao, "Nonlinear resolution enhancement of an fbg based temperature sensor using the kerr effect," Opt. Express **28**(26), 39181–39188 (2020).
12. B. Wang, X. Fan, S. Wang, J. Du, and Z. He, "Millimeter-resolution long-range ofdr using ultra-linearly 100 ghz-swept optical source realized by injection-locking technique and cascaded fwm process," Opt. Express **25**(4), 3514–3524 (2017).
13. B. Wang, X. Fan, Q. Liu, J. Du, and Z. He, "Spatial resolution enhancement in optical coherence domain reflectometry using high-order fwm process," in *Asia Communications and Photonics Conference 2016*, (Optica Publishing Group, 2016), p. AF1A.5.
14. J. Du and Z. He, "Sensitivity enhanced strain and temperature measurements based on fbg and frequency chirp magnification," Opt. Express **21**(22), 27111–27118 (2013).
15. Y. Wang, O. Krarup, L. Chen, and X. Bao, "Frequency sweep extension using the kerr effect for static temperature measurement range enhancement in chirped pulse ϕ-otdr," Opt. Express **29**(15), 23202–23212 (2021).
16. A. Boskovic, S. V. Chernikov, J. R. Taylor, L. Gruner-Nielsen, and O. A. Levring, "Direct continuous-wave measurement of n2 in various types of telecommunication fiber at 1.55 μm," Opt. Lett. **21**(24), 1966–1968 (1996).
17. F. W. J. Olver, B. O. Daalhuis, D. W. Lozier, B. I. Schneider, R. F. Boisvert, C. W. Clark, B. R. Miller, B. V. Saunders, H. S. Cohl, and M. A. McClain, "NIST Digital Library of Mathematical Functions," http://dlmf.nist.gov/10.12, Release 1.0.27 of 2020-06-15.
18. E. A. Kuzin, B. I. Escamilla, F. G. Zainos, J. Haus, and J. Estudillo-Ayala, "Measurements of beat length in short low-birefringence fibers," in *Conference on Lasers and Electro-Optics*, (Optical Society of America, 2002), p. CThO21.
19. O. Krarup, "Custom Nonlinear Schroedinger Equation solution in Jones formalism," https://doi.org/10.6084/m9.figshare.16944094 (2021).
20. O. Krarup, "Dispersion data for NLSE code," https://doi.org/10.6084/m9.figshare.16944091.v1 (2021).
21. C. Baker, L. Chen, and X. Bao, "Sensitivity enhancement beyond the wavelength limit in a novel sub-micron displacement sensor," Opt. Express **23**(14), 17838–17844 (2015).
22. M. Wuilpart, A. Gusarov, P. Moreau, W. Leysen, and P. Mégret, "Use of a polarization otdr for the measurement of plasma current in the tore supra thermonuclear fusion reactor," in *Advanced Photonics 2017 (IPR, NOMA, Sensors, Networks, SPPCom, PS)*, (Optical Society of America, 2017), p. SeW2E.5.
23. C. K. Keyser, R. K. Martin, H. Lopez-Aviles, K. Nguyen, A. M. Adams, and D. Christodoulides, "Single-pulse, kerr-effect mueller matrix lidar polarimeter," Opt. Express **28**(9), 13694–13713 (2020).
24. O. Krarup, "Data collected and analyzed in this work," figshare (2021), https://figshare.com/articles/dataset/Data/17087522.

6.1 Supplement

This section contains the supplement to the paper on enhanced polarimetric sensing, where the complete model for the dependence of sideband power on input polarization is derived. In the interest of deriving the most general possible model, the input field in the published supplement contains a phase shift, δ, between the two lasers, making it differ from Eq. 3.62. At the time of publication, it was not realized that the overall phase shift, δ, is redundant, since defining $\delta = -\delta'$ yields

$$\begin{aligned}
&\exp\left(-i\frac{1}{2}\omega_d t - i\delta'\right) + \exp\left(i\frac{1}{2}\omega_d t\right) \\
&= \left[\exp\left(-i\frac{1}{2}\omega_d t - i\delta'/2\right) + \exp\left(i\frac{1}{2}\omega_d t + i\delta'/2\right)\right]\exp\left(-i\delta'/2\right) \\
&= \left[\exp\left(-i\frac{1}{2}\omega_d\left(t + \delta'/\omega_d\right)\right) + \exp\left(i\frac{1}{2}\omega_d\left(t + \delta'/\omega_d\right)\right)\right]\exp\left(-i\delta'/2\right) \\
&= \left[\exp\left(-i\frac{1}{2}\omega_d\tau\right) + \exp\left(i\frac{1}{2}\omega_d\tau\right)\right]\exp\left(-i\delta'/2\right),
\end{aligned}$$

which implies that δ only affects the overall phase of the field and none of the SOPs.

Research Article | Vol. 30, No. 9 / 25 Apr 2022 / Optics Express 13985
Optics EXPRESS

Sensitivity enhancement of fiber optical polarimetric sensors using self-induced nonlinear phase modulation via the Kerr effect

OLE KRARUP,* CHAMS BAKER, LIANG CHEN, AND XIAOYI BAO

Fiber Optics Group, Department of Physics, University of Ottawa, Ottawa, Canada K1N 6N5, Canada
okrarup@uottawa.ca

Abstract: This work presents an analytical model accounting for the impact of optical polarization on the generation of frequency sidebands by the Kerr effect in a highly nonlinear fiber. Theoretical analysis shows that for a relative polarization angle, α, between two input lasers expressed on the Poincaré sphere, the optical power of the n^{th} order sideband is proportional to $\cos^{2n}(\alpha/2)$. This theoretical result enables a novel all-optical technique for interrogating changes in polarization with higher sensitivity than conventional measurement schemes using linear polarizers. The predicted theoretical relationship between the sideband power and the relative polarization angle is verified experimentally and sensitivity enhancement by a factor of 1.45 compared to a conventional polarimetric sensor is demonstrated for the 3rd order sideband. This novel nonlinear approach, which allows dynamic range to be traded for an enhanced ability to detect small polarization variations, has potential applications in fusion reactor monitoring, instrumentation and material characterization.

1. Introduction

For environmental sensing, systems relying on optical fibers have a number of advantages compared to electrical devices. Apart from speed, durability and immunity to electromagnetic interference, optical fibers allow for novel sensing schemes based on the polarization of light. Various environmental perturbations can be detected as they affect the birefringence in optical fibers, leading to measurable changes in the state of polarization of light propagating within. Examples of such sensing schemes include polarization optical time domain reflectometry (P-OTDR) [1] and magnetic field sensing using the Faraday effect [2], which has been applied to detect electrical current variations on the order of 1 mA [3]. When incident polarized light has an angle θ with the axis of a polarizer, the output intensity follows Malus' law [4], $I = I_0 \cos^2(\theta)$, where I_0 is the incident intensity, and the sensitivity is $dI/d\theta = -I_0 \sin(2\theta)$ with an extremum at $\theta = 45°$. If a hypothetical optical system could cause the detected intensity to follow the relation $I = I_0 \cos^{2n}(\theta)$, the maximum sensitivity is increased by a factor

$$\epsilon_n = \frac{2n}{\sqrt{2n-1} \cdot \left(1 + \frac{1}{(2n-1)}\right)^n} \tag{1}$$

at $\theta = \arctan((2n-1)^{-1/2})$. For example, when $n = 3$, maximum sensitivity is achieved at $\theta = 24.1°$ and is approximately 1.55 times greater than for the $n = 1$ case corresponding to Malus' law.

All-optical signal processing refers to techniques for manipulating the wavelength, polarization, phase and amplitude of signals using nonlinear effects. Such methods have been employed to enhance optical signals used in telecommunication [5], to amplify weak signals [6], and to generate supercontinuum light [7]. Compared to linear processing methods, all-optical signal processing approaches utilizing the Kerr effect enable improved performance of fiber based

#454492 https://doi.org/10.1364/OE.454492
Journal © 2022 Received 23 Jan 2022; revised 28 Mar 2022; accepted 30 Mar 2022; published 11 Apr 2022

Optics EXPRESS

environmental sensors. When two frequencies of light are launched into a highly nonlinear optical fiber, frequency sidebands are generated. The powers of the sidebands are proportional to integer exponents of the input powers, which has been exploited to improve the extinction ratio of pulses in OTDR, resulting in an enhanced signal to noise ratio (SNR) [8]. The power dependence of the sidebands has also been utilized to magnify small power fluctuations [9], stabilize signals to reduce intensity noise [10], and to enhance the resolution of a fiber Bragg grating (FBG) based temperature sensor [11]. Furthermore, if the frequency difference between two lasers launched into a Kerr medium is increased by $\Delta\omega$, the n^{th} order sideband will shift by $n\Delta\omega$, thereby extending the laser sweeping range. This sweep extension has been applied to enhance the resolution of optical frequency domain reflectometry (OFDR) and to improve the sensitivity of an FBG used for strain sensing [12–14]. It has also been used to enhance the frequency sweeping rate of signals used in chirped-pulse phase-OTDR (CP ϕ-OTDR), extending the sensing range of single-shot measurements [15]. None of these models include the effects of polarization on the powers of the generated sidebands and results indicate that ignoring polarization is only valid if the incident lasers are co-polarized. A detailed theoretical model describing how sideband generation via the Kerr effect depends on polarization would lead to a deeper understanding of the underlying physics and enable novel sensing schemes.

In this paper, we propose a fully analytical model for calculating the polarization dependence of the powers of frequency sidebands generated by the Kerr effect. Theoretical and experimental results show that when birefringence in the nonlinear medium can be ignored, the power of the frequency sidebands as a function of incident polarization follows a simple analytical expression. The polarization dependence of the sideband power is experimentally exploited to increase the sensitivity of a polarimetric sensor by a factor of 1.45 for the 3rd order sideband. Finally, limitations of the presented analytical model are discussed along with potential applications to existing polarization based sensors.

2. Theory

A detailed derivation of the following results is presented in Supplement 1. Launching lasers at two different angular frequencies, ω_r and ω_s with $\omega_r<\omega_s$, into an optical fiber with a length, L, and a waveguide nonlinearity parameter, γ, the electric field amplitude at the input is given by

$$|A_{in}\rangle = \sqrt{P_r}\begin{pmatrix}\cos\theta\\ \sin\theta e^{i\phi}\end{pmatrix}e^{i\delta}e^{-i0.5\omega_d t} + \sqrt{P_s}\begin{pmatrix}\cos\beta\\ \sin\beta e^{i\xi}\end{pmatrix}e^{i0.5\omega_d t}, \tag{2}$$

where P_r and P_s are respectively the powers of the reference and the signal, $\omega_d = \omega_s - \omega_r$, θ and β are respectively the angles of the polarization vectors relative to the x-axis for the reference and the signal, ϕ and ξ are respectively the phase differences between the orthogonal polarization components of the fields for the reference and the signal, while δ is a phase delay between the two lasers. Computing the power of the input field yields $\langle A_{in}|A_{in}\rangle = P_r + P_s + 2\sqrt{P_r P_s}\cos(\alpha/2)\cos(\omega_d t + k)$, where k is a phase factor, which depends on the values of θ, β, ϕ, ξ and δ, while α is the angle between the reference and signal fields when represented as vectors on the Poincaré sphere as visualized in Fig. 1(a).

Neglecting dispersion, attenuation and random birefringence along the fiber, the Nonlinear Schrödinger Equation (NLSE) reduces to $\partial_z|A(z)\rangle = i\gamma\langle A|A\rangle|A(z)\rangle$, which is solved analytically to obtain an expression for the field amplitude at the output of the fiber, $|A_{out}\rangle = |A_{in}\rangle \exp(i\gamma L(P_r + P_s))\exp(i2\gamma L\sqrt{P_r P_s}\cos(\alpha/2)\cos(\omega_d t + k))$. Applying the Jacobi-Anger expansion [16,17], the output field is expressed as an infinite sum of frequency sidebands spaced $\omega_d/2\pi$ apart, and is

Optics EXPRESS

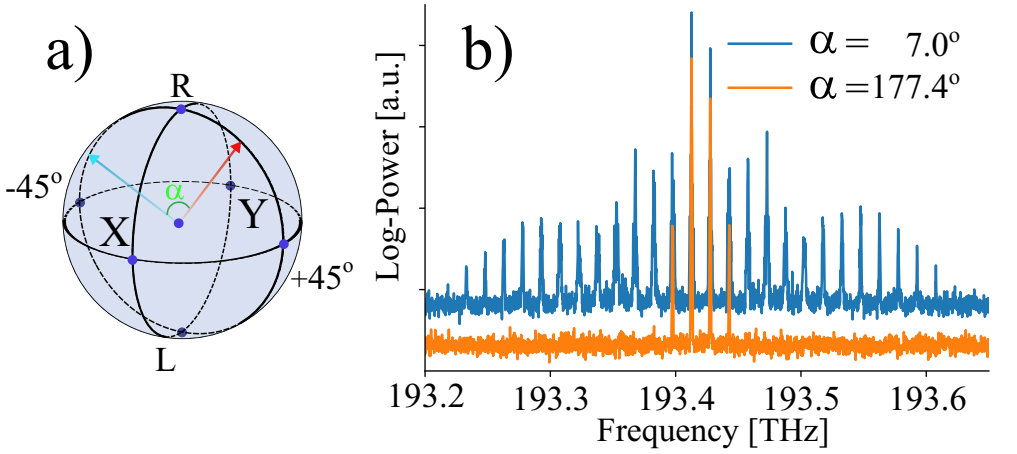

Fig. 1. (a) The polarizations of the lasers in Eq. (2) represented on the Poincaré sphere. If their relative angle, α, is zero, the two lasers are co-polarized. For $\alpha = 180°$, the polarizations of the two lasers are orthogonal, which prevents them from interfering and generating sidebands. (b) Optical spectra recorded after the Kerr medium for reference and signal pulses that are almost completely copolarized (blue) and ones that are almost completely orthogonal (orange). Traces have been vertically offset for clarity.

given by $|A_{out}\rangle = \exp\left(i\gamma L(P_r + P_s)\right) \sum_{n=-\infty}^{\infty} i^n e^{ink} e^{i(n+0.5)\omega_d t} |A_n\rangle$, where

$$|A_n\rangle = \left[\begin{pmatrix} i\sqrt{P_r}\cos\theta e^{i(\delta+k)} J_{n+1}(\phi_{\mathrm{NL}}) + \sqrt{P_s}\cos\beta J_n(\phi_{\mathrm{NL}}) \\ i\sqrt{P_r}\sin\theta e^{i\phi} e^{i(\delta+k)} J_{n+1}(\phi_{\mathrm{NL}}) + \sqrt{P_s}\sin\beta e^{i\xi} J_n(\phi_{\mathrm{NL}}) \end{pmatrix}\right], \tag{3}$$

and $\phi_{\mathrm{NL}} = 2\gamma L\sqrt{P_r P_s}\cos(\alpha/2)$. The subscript $n = -1$ corresponds to the frequency component at $\omega_r/2\pi$, while $n = 0$ corresponds to the frequency component at $\omega_s/2\pi$. The power of the n^{th} order sideband is $\langle A_n|A_n\rangle = P_r J_{n+1}^2(\phi_{\mathrm{NL}}) + P_s J_n^2(\phi_{\mathrm{NL}})$, which implies that the powers of the sidebands at the output of the fiber depend on the initial angle, α. Introducing the normalization, $x = \gamma L P_s$, $y = \gamma L P_r$, $z_n = \gamma L\langle A_n|A_n\rangle$, and applying the asymptotic approximation of the Bessel functions for $n>0$ and $0<\phi_{\mathrm{NL}}<\sqrt{1+n}$, the power of the n^{th} order sideband is

$$z_n \approx \frac{x^n y^{n+1}}{[n!]^2}\cos^{2n}(\alpha/2), \tag{4}$$

implying that the power of the n^{th} order sideband decreases as α increases towards its maximum value of 180°. Defining $z_n^{(max)} = z_n(\alpha = 0)$ and $z_n^{(min)} = z_n(\alpha)$, the ratio of these two quantities for the n^{th} order sideband is

$$r_n(\alpha) = \frac{z_n^{(min)}}{z_n^{(max)}} = \cos^{2n}(\alpha/2) = r_1^n(\alpha). \tag{5}$$

Thus, if the angle between the reference and signal is changed from 0 to α, the ratio of minimum power to maximum power will be smaller for higher order sidebands.

3. Experimental setup and results

The experimental setup used for investigating the enhanced response to variations in relative polarization is presented in Fig. 2(a). The temporal power and the power spectral density

Optics EXPRESS

(PSD) of the light at different points along the optical path are illustrated in Figs. 2(b-e). A laser (NLL:PS-NLL-1550.12, Teraxion) with a linewidth of 5 kHz emitting at 193412.72 GHz (1550.014 nm) is aligned to a linear polarizer (POL1) ensuring light propagation in only one of the polarization axes of an electro-optical modulator (EOM1, MXPE-LN-10, Photline) that is driven by an arbitrary waveform generator (AFG 3252, Tektronix) to obtain optical pulses with a duration of 4 ns. Nanosecond pulses are utilized instead of a continuous wave laser to suppress the effect of stimulated Brillouin scattering (SBS) on subsequent all-optical signal processing and measurements. Using a 50:50 coupler, the laser pulses are split into two branches: the signal branch and the reference branch. Pulses in the signal branch are polarized by POL2 and amplified using a polarization maintaining erbium doped fiber amplifier (PM-EDFA, EDFA100P, THORLABS). The signal is then sinusoidally modulated using EOM2 (OC-192, JDS UNIPHASE) driven at a frequency of 12 GHz by an electronic radio frequency source (83752A, Hewlett Packard) to generate two new frequency components located at 193400.72 GHz (1550.110 nm) and 193424.72 GHz (1549.918 nm). A 3 GHz bandpass filter (BPF1, TFC 3GHz, TeraXion) extracts the frequency component at 193424.72 GHz (1549.918 nm), which is amplified using a high power EDFA (HP-EDFA1, APEDFA-C-10-B-FA, Amonics) and passed through BPF2 (TB9 Optical Grating Filter, JDS Uniphase). POL3 then realigns the polarization of the pulses in case of power dependent polarization rotation in HP-EDFA1. The signal pulses are subsequently passed through a polarization modulator (POM, Corning PC-410), which is driven by a square waveform with a period of 4 s and an adjustable peak voltage from the arbitrary waveform generator, thereby modulating the polarization of the signal. The signal passes through PC1 followed by a 50:50 coupler where one arm leads to a shutter (SH1) which remains closed, while the other arm connects to a second coupler (C1) combining the signal pulses with pulses from the reference branch.

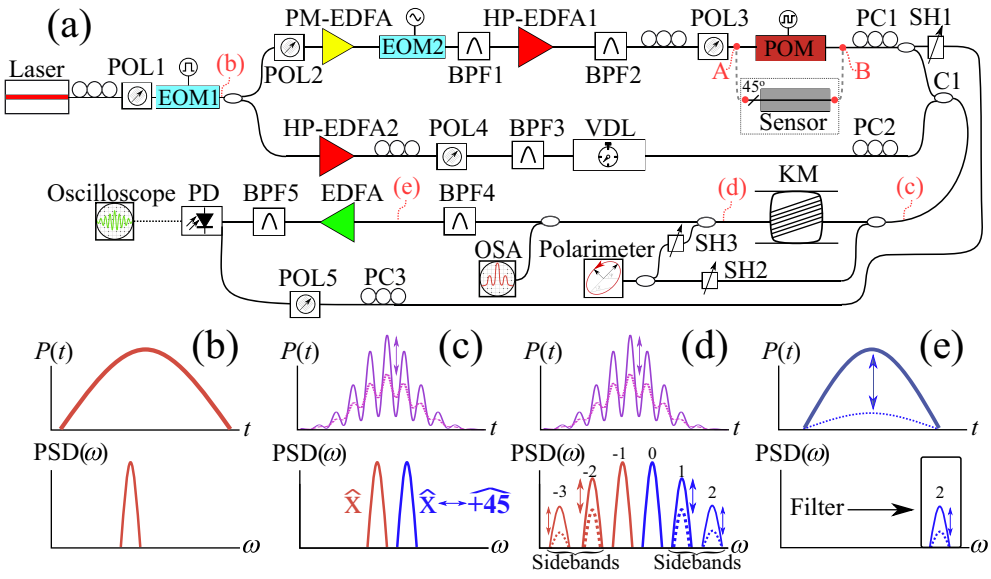

Fig. 2. (a) The experimental setup used for investigating the dependence of frequency sideband generation via the Kerr effect on polarization. (b-e): The light in the time- and angular frequency domains at different points along the optical path. Modulating the polarization of the signal pulses away from a state of co-polarization with the reference pulses reduces the power of the higher order sidebands according to Eq. (5).

Optics EXPRESS

Pulses in the reference branch, are amplified by HP-EDFA2 (AEDFA-33B-FA, Amonics) and have their polarization realigned by POL4 in case of power dependent polarization rotation in the amplifier. The pulses are filtered by BPF3 (Ultra Narrow Filter, AOS) and then passed through a variable delay line (VDL, MDL-002, General Photonics) followed by PC2 and C1. The time delay introduced by the VDL is adjusted to ensure that the reference- and signal pulses arrive at C1 simultaneously.

A small portion of the combined signal and reference pulses is extracted by a coupler and sent through an open SH2 to a polarimeter (IPM5300, THORLABS). By turning on the reference- and signal pulses individually, their polarizations can be adjusted using PC1 and PC2 to coincide when a 0V signal is applied to the POM. The combined signal and reference pulses propagate through a Kerr medium (KM) consisting of a 5.7 km highly nonlinear fiber (418SG 04611A, Draka Comteq). SH2 is closed and a portion of the output of the Kerr medium is extracted and sent through SH3 to the polarimeter. By turning on the initially copolarized reference and signal pulses individually, the polarimeter measures the change in α induced by wavelength dependent, randomly varying birefringence along the Kerr medium. Launching the co-polarized signal- and reference pulses into the Kerr medium individually with several different choices of polarization states, their relative angle on the Poincaré sphere at the output of the Kerr medium remains below 8.58°. When light propagates in a medium with randomly varying birefringence, the state of polarization changes with a beat length of $L_B = \lambda/|n_x - n_y|$. Assuming $|n_x - n_y| = 10^{-7}$, which is a typical average value for the local birefringence in commercially available single mode fibers [18], the beat lengths for the reference- and signal pulses are 15.50014 m and 15.49918 m respectively, implying that they have undergone 367.739 and 367.761 beat cycles respectively at the end of the 5.7 km Kerr medium. Such an estimated drift of $(367.761 - 367.739) \cdot 100\% = 2.2\%$ of a beat cycle between the signal and reference pulses corresponds to a relative angle on the Poincaré sphere of $360° \cdot 0.022 = 7.92°$, which is comparable to the experimentally measured maximum drift of 8.58°. Because the maximum drift of 2.2% is relatively small, the impact of wavelength dependent randomly varying birefringence on light propagating in the Kerr medium can safely be ignored.

The spectrum of the output of the Kerr medium is measured using an optical spectrum analyzer (OSA, AP2043B, APEX). Two spectra measured with identical reference- and signal powers, but different relative polarizations, are presented in Fig. 1(b). The measured spectra show that propagation in the Kerr medium leads to the generation of sidebands due to self-induced nonlinear phase modulation and that the power of generated sidebands depends on α. The output of the Kerr medium then passes through BPF4 (XTM-50, EXFO), which extracts the n^{th} order sideband. This sideband signal is amplified by an EDFA (AEDFA-PA-25-B-FA, Amonics), passed through BPF5 (TFC 3GHz, TeraXion) to eliminate residual ASE noise from the amplifier and finally detected by a photodiode (PD, Model 1592 3.5 GHz, New Focus). The PD is connected to an oscilloscope (infiniium DSO81204B, Agilent) sampling at 20 GSa/s and averaging 16 traces to reduce the impact of optical intensity fluctuations and electrical noise.

SH2 is opened, and the input angle on the Poincaré sphere between the reference and signal pulses is recorded for a range of voltages applied to the POM. BPF4 and BPF5 are adjusted to extract each sideband, and the oscilloscope is programmed to record the traces with the highest and lowest intensity. In Fig. 3, measurements for $n = 1$ to $n = 5$ of the maximum trace corresponding to $\alpha = 0°$ is shown in blue along with the minimum traces corresponding to $\alpha = 57.93°$ in orange. The traces have been normalized to the peak power of the maximum trace. The theoretical ratio of the minimum trace to the maximum trace calculated using Eq. (5) is plotted in green, showing close agreement with experimental results. Figure 4 presents the measured and analytically calculated ratios for sidebands 1 through 5 and maximum angles ranging from 21.53° to 63.50°. Figure 4 also presents ratios calculated numerically by solving the NLSE using the Split Step Fourier Method in the presence of randomly varying birefringence [19,20], and the

Optics EXPRESS

ratio for the first order sideband raised to the n^{th} integer power. The experimentally measured ratios agree well with the analytically and numerically calculated values, confirming the validity of Eq. (5). Discrepancies between theoretical and experimental ratios arise from electrical noise and fluctuations in the optical power of the recorded traces. As described in other works on sideband generation, extracting pulses from higher order sidebands effectively magnifies their intensity noise causing inaccuracies in the measured maximum and minimum traces [9,15].

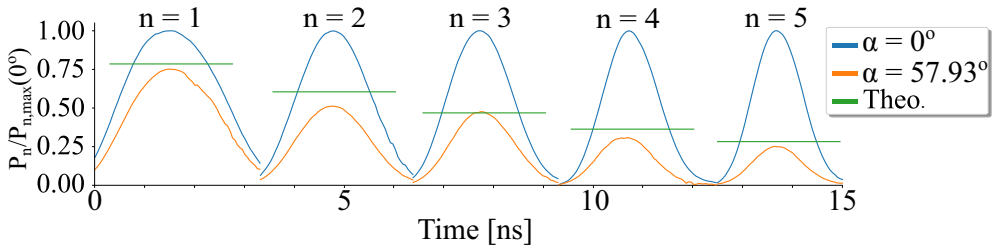

Fig. 3. Experimental measurements of the maximum and minimum traces acquired by varying α from 0° to 57.93°. The measured power has been normalized to the peak power of the maximum trace corresponding to $\alpha = 0°$.

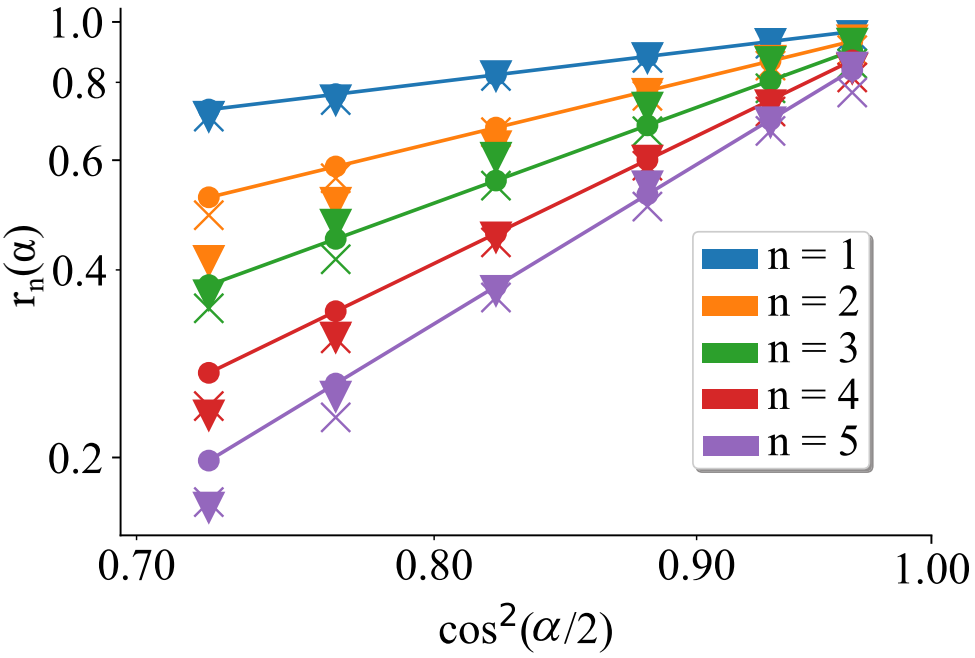

Fig. 4. Double logarithmic plot of the ratio in Eq. (5) for different sidebands and α values in the range from 21.53° to 63.50°. Straight lines (−): Analytically calculated ratio obtained using $\cos^{2n}(\alpha/2)$. Circles (○): Ratio according to numerical simulation. Triangles (▽): Experimentally determined ratio. Crosses (×): Experimental ratio for r_1 raised to the n^{th} power.

The practical utility of polarization sensitivity enhancement using higher order sidebands is demonstrated by combining this effect with a polarimetric sensor. The POM is detached from the connectors labelled A and B in Fig. 2(a) and replaced with a polarimetric sensor consisting of a

Optics EXPRESS

PM fiber spliced at a 45° angle with the output of POL3. The PM fiber under test (FUT) is glued to a metal cantilever to which weights can be attached. When polarized pulses from POL3 reach the FUT, the incoming light is split evenly between the fast and slow axes. As the signal pulses travel through the polarimetric sensor, the accumulated phase shift between light in the fast and slow axes causes the state of polarization to alternate between linear and circular. Bending the cantilever by applying weight induces strain in the FUT and alters the phases accumulated by light travelling along the fast and slow axes, which changes the polarization state of light at the end of the FUT. SH1 is opened and PC3 aligns the principal axis of the FUT at a 45° angle with the polarization axis of POL5, producing a raw signal whose peak power varies according to Malus' law. A static delay line ensures that the processed signal and the raw signal arrive at the PD with a time delay that allows them to be captured in the same oscilloscope trace. PC2 is adjusted such that variations in the polarization of the signal pulse lead to maximum variation in the power of the sidebands. Subsequently, the peak powers of the raw- and sideband signals are equalized, enabling a direct comparison of their responses to a change in polarization caused by increased weight on the cantilever. Adding identical 4 g weights, each applying a force of ~ 40 mN, to the end of the cantilever changes the power of the raw signal and the signal generated by extracting the 3rd order sideband as presented in Fig. 5(a). Recording the peak power as a function of applied weight as presented in Fig. 5(b) shows that the raw signal follows Malus' law, while the enhanced signal follows cosine to the 6th power in agreement with Eq. (4). Furthermore, the maximum slope for the enhanced signal is 1.45 times larger than the slope for the raw signal in agreement with the value of 1.55 predicted by Eq. (1), demonstrating sensitivity enhancement in a practical application. The curve for the raw signal is approximately linear over a range of 400 mN, while the curve for the enhanced signal is approximately linear in a 200 mN range, which illustrates the trade-off between sensitivity and dynamic range.

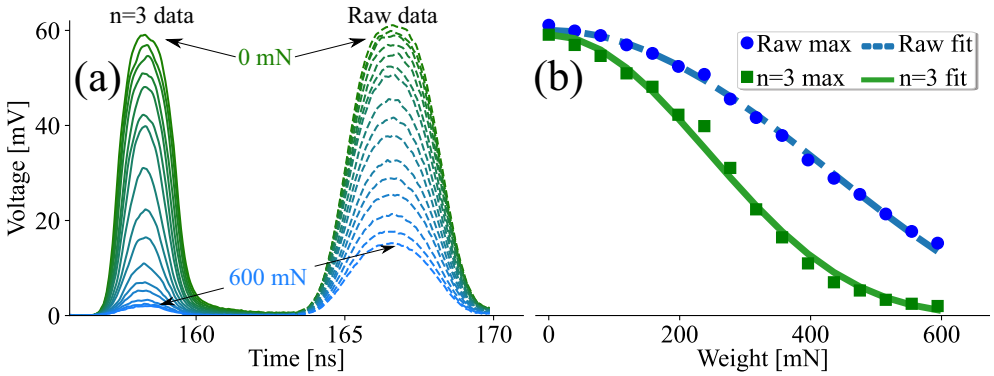

Fig. 5. (a) Oscilloscope data showing the power of the raw signal from a conventional polarimetric sensor (right) and enhanced measurements from the 3rd order sideband (left) as the weight applied at the end of the cantilever is increased from 0 to 600 mN in steps of 40 mN. The enhanced signal shows a greater change in voltage per applied weight than the raw signal, indicating enhanced sensitivity to changes in polarization. (b) Peak voltage of the two signals versus applied weight. The curve for the raw signal follows the square of the cosine of the applied weight while the curve for the 3rd order sideband follows cosine to the 6th power as predicted by Eq. (4).

4. Discussion

A number of simplifications are used in the analytical model for polarization dependent sideband generation via the Kerr effect. The presented model ignores the impact of attenuation in the

Optics EXPRESS

Kerr medium, which in the general case can be accounted for by replacing the length of the fiber with an effective length, $L_{\text{eff}} = [1 - \exp(-\alpha_L L)]/\alpha_L$, where α_L is the loss coefficient. The presented model also ignores the impact of chromatic dispersion, which is justifiable when the dispersion length is much greater than the nonlinear length. The dispersion length is given by $L_D = 2\pi c T_0^2/\lambda^2 D$, where c is the speed of light in vacuum, T_0 is the pulse duration, λ is the central wavelength and D is the chromatic dispersion. Using $T_0 = 2\pi/(4\omega_d) = 20.75$ ps corresponding to the full width at half maximum within one cycle of the interference signal, $\lambda = 1550$ nm and $D = 3$ ps/(nm·km) as reported in [21] leads to $L_D = 112.5$ km. In contrast, the nonlinear length is given by $L_{\text{NL}} = 1/\gamma P$ with γ being the waveguide nonlinearity parameter and P being the peak power. The present model is valid for $0 < \phi_{\text{NL}} < \sqrt{1+n}$ and using $\phi_{\text{NL}} = 2\gamma LP$, where $P = \sqrt{P_r P_s}$, while operating under the condition $\phi_{\text{NL}} < 1$ leads to $L_{\text{NL}} \approx 2L \approx 11.4$ km. Because $L_D \gg L_{\text{NL}}$, the assumption of negligible chromatic dispersion underlying the analytical model is valid in the presented experiment.

The enhanced sensitivity to changes in polarization for higher order sidebands can be used for improving existing polarimetric sensing systems. Examples include polarization-OTDR, which has been used for measuring magnetic fields generated by prototype fusion reactors [22]. Equation (3) also enables the calculation of the state of polarization of the n^{th} order sideband. Because the polarization of the n^{th} order sideband is a function of the input power, which varies with time for non-square pulses, extracting higher order sidebands produces pulses with time dependent states of polarization. The generation of such pulses, which is a topic of ongoing research, could be used to analyze the properties of material surfaces [23]. Another potential application exploits the dependence of sideband power on relative polarization to build an all-optical polarimeter without the need for physical polarizers or waveplates for detection. Such applications will be explored in future work.

5. Conclusion

Enhancement of the sensitivity to changes in polarization based on the Kerr effect is demonstrated for sidebands up to $n = 5$. This all-optical signal processing approach is combined with a polarimetric sensor to achieve a sensitivity improvement by a factor 1.45 for the 3rd order sideband. The theoretical model provides an analytical expression that agrees with experimental results. The technique can be applied to existing systems measuring changes in relative polarization to improve measurement sensitivity.

Funding. Canada Research Chairs (75-67138); Natural Sciences and Engineering Research Council of Canada (DG-2020-06302).

Disclosures. The authors declare no conflicts of interest.

Data Availability. Data underlying the results presented in this paper are available in Ref. [24].

Supplemental document. See Supplement 1 for supporting content.

References

1. A. J. Rogers, "Polarization-optical time domain reflectometry: a technique for the measurement of field distributions," Appl. Opt. **20**(6), 1060–1074 (1981).
2. R. H. Stolen and E. H. Turner, "Faraday rotation in highly birefringent optical fibers," Appl. Opt. **19**(6), 842–845 (1980).
3. H. Zhang, Y. Dong, J. Leeson, L. Chen, and X. Bao, "High sensitivity optical fiber current sensor based on polarization diversity and a faraday rotation mirror cavity," Appl. Opt. **50**(6), 924–929 (2011).
4. M. Étienne Louis, "Mémoire sur la mesure du pouvoir réfringent des corps opaques," in *Bulletin de la Société philomathique de Pari*, vol. 1-11 (Société philomathique de Paris, Paris, 1826), pp. 77–81, 6th ed.
5. A. E. Willner, S. Khaleghi, M. R. Chitgarha, and O. F. Yilmaz, "All-optical signal processing," J. Lightwave Technol. **32**(4), 660–680 (2014).
6. C. J. McKinstrie, S. Radic, and A. H. Gnauck, "All-optical signal processing byfiber-based parametric devices," Opt. Photonics News **18**(3), 34–40 (2007).
7. G. Moille, E. F. Perez, J. R. Stone, A. Rao, X. Lu, T. S. Rahman, Y. K. Chembo, and K. Srinivasan, "Ultra-broadband Kerr microcomb through soliton spectral translation," Nat. Commun. **12**(1), 7275 (2021).

Optics EXPRESS

8. B. Vanus, C. Baker, L. Chen, and X. Bao, "High extinction ratio optical pulse characterization method via single-photon counting," Appl. Opt. **60**(1), 20–23 (2021).
9. B. Vanus, C. Baker, L. Chen, and X. Bao, "All-optical intensity fluctuation magnification using kerr effect," Opt. Express **28**(3), 3789–3794 (2020).
10. B. Vanus, C. Baker, L. Chen, and X. Bao, "All-optical pulse peak power stabilization and its impact in phase-otdr vibration detection," OSA Continuum **4**(5), 1430–1436 (2021).
11. O. Krarup, C. Baker, L. Chen, and X. Bao, "Nonlinear resolution enhancement of an fbg based temperature sensor using the kerr effect," Opt. Express **28**(26), 39181–39188 (2020).
12. B. Wang, X. Fan, S. Wang, J. Du, and Z. He, "Millimeter-resolution long-range ofdr using ultra-linearly 100 ghz-swept optical source realized by injection-locking technique and cascaded fwm process," Opt. Express **25**(4), 3514–3524 (2017).
13. B. Wang, X. Fan, Q. Liu, J. Du, and Z. He, "Spatial resolution enhancement in optical coherence domain reflectometry using high-order fwm process," in *Asia Communications and Photonics Conference 2016*, (Optica Publishing Group, 2016), p. AF1A.5.
14. J. Du and Z. He, "Sensitivity enhanced strain and temperature measurements based on fbg and frequency chirp magnification," Opt. Express **21**(22), 27111–27118 (2013).
15. Y. Wang, O. Krarup, L. Chen, and X. Bao, "Frequency sweep extension using the kerr effect for static temperature measurement range enhancement in chirped pulse ϕ-otdr," Opt. Express **29**(15), 23202–23212 (2021).
16. A. Boskovic, S. V. Chernikov, J. R. Taylor, L. Gruner-Nielsen, and O. A. Levring, "Direct continuous-wave measurement of n2 in various types of telecommunication fiber at 1.55 μm," Opt. Lett. **21**(24), 1966–1968 (1996).
17. F. W. J. Olver, B. O. Daalhuis, D. W. Lozier, B. I. Schneider, R. F. Boisvert, C. W. Clark, B. R. Miller, B. V. Saunders, H. S. Cohl, and M. A. McClain, "NIST Digital Library of Mathematical Functions," http://dlmf.nist.gov/10.12, Release 1.0.27 of 2020-06-15.
18. E. A. Kuzin, B. I. Escamilla, F. G. Zainos, J. Haus, and J. Estudillo-Ayala, "Measurements of beat length in short low-birefringence fibers," in *Conference on Lasers and Electro-Optics*, (Optical Society of America, 2002), p. CThO21.
19. O. Krarup, "Custom Nonlinear Schroedinger Equation solution in Jones formalism," https://doi.org/10.6084/m9.figshare.16944094 (2021).
20. O. Krarup, "Dispersion data for NLSE code," https://doi.org/10.6084/m9.figshare.16944091.v1 (2021).
21. C. Baker, L. Chen, and X. Bao, "Sensitivity enhancement beyond the wavelength limit in a novel sub-micron displacement sensor," Opt. Express **23**(14), 17838–17844 (2015).
22. M. Wuilpart, A. Gusarov, P. Moreau, W. Leysen, and P. Mégret, "Use of a polarization otdr for the measurement of plasma current in the tore supra thermonuclear fusion reactor," in *Advanced Photonics 2017 (IPR, NOMA, Sensors, Networks, SPPCom, PS)*, (Optical Society of America, 2017), p. SeW2E.5.
23. C. K. Keyser, R. K. Martin, H. Lopez-Aviles, K. Nguyen, A. M. Adams, and D. Christodoulides, "Single-pulse, kerr-effect mueller matrix lidar polarimeter," Opt. Express **28**(9), 13694–13713 (2020).
24. O. Krarup, "Data collected and analyzed in this work," figshare (2021), https://figshare.com/articles/dataset/Data/17087522.

Chapter 7

All-optical polarimeter

The four authors listed in this paper, titled "All-optical polarimeter for laser Stokes vector measurement using self-induced nonlinear phase modulation", published in Optics Express [96], contributed in the following ways. The present author developed the mathematical method for calculating the SOP from measurements of sideband power, constructed the setup, processed the data and wrote the bulk of the paper. Dr. Chams Baker provided key suggestions for improving the setup and advice on editing the paper. Prof. Liang Chen and prof. Xiaoyi Bao made recommendations for the structure of the paper, including which aspects to explore in depth.

The purpose of this paper is to demonstrate a novel approach for determining the SOP of a laser using all-optical signal processing. Conventional, commercially available polarimeters typically use physical polarizers as a reference in schemes such as the one presented in Fig. 2.7, but Eq. 3.74 shows that one can use a laser instead. Because accurate measurement of optical polarization is useful for many scientific endeavours, the advantages and limitations of this new method were explored.

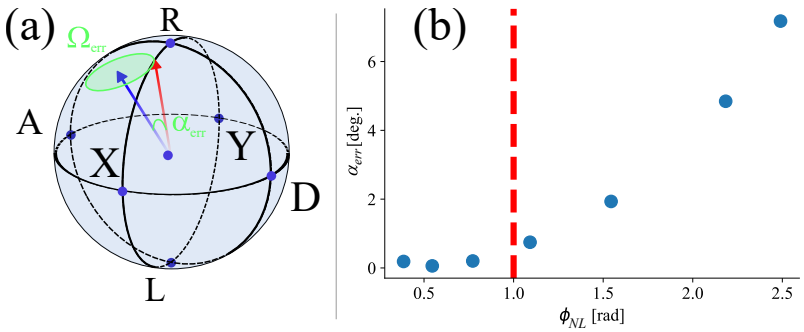

Figure 7.1: (a) Illustration of the error angle, α_{err}, and the error area, Ω_{err} when comparing the SOP computed numerically using the vector version of Eq. 3.38 (blue) and the actual SOP used for the simulation (red). (b) Error angle between initial SOP and the SOP determined using the numerical solution of the code implemented in [4] for different values of ϕ_{NL}. The rapid increase in the error for $\phi_{NL} > 1$ is in accordance with Eq. 3.72.

The error angle, α_{err} between the SOP measured by the conventional polarimeter and the SOP measured using the nonlinear method was determined to be at most 10.22° on the Poincaré sphere. Conventional polarimeters, including the one utilized as a reference in the present experiment, list SOP accuracies on the Poincaré sphere of approximately ±0.25° [97, 98], implying that the setup is not as accurate as commercially available devices. The main reason seems to be a bias introduced when determining the degree of circular polarization, most likely due to an imperfect calibration caused by randomly varying birefringence.

Another factor potentially reducing the fidelity of the method is the impact of operating with high optical powers, where $\phi_{NL} \approx 1$ causes Eq. 3.72 to be invalid. To investigate this effect, a numerical simulation of the vectorial version of Eq. 3.38 was conducted using the code in [4]. A wide signal pulse with a known SOP was overlapped with six reference pulses spaced 5 ns apart having SOPs along the cardinal directions of the Poincaré and equal powers. The simulation was carried out for a range of different signal powers allowing the initial SOP determined from the simulation to be calculated from Eq. 3.74 and α_{err} to be calculated from its dot product with the known initial SOP. Figure 7.1(a) contains an illustration of how α_{err} is defined, while Fig. 7.1(b) presents the results of the simulation, demonstrating a noticeable increase in α_{err} for $\phi_{NL} > 1$ as predicted by Eq. 3.72. Note that the effect of an excessive value of ϕ_{NL} is still small compared to the value of $\alpha_{err,max} = 10.22°$ determined in the experiment, indicating that reference laser misalignment caused by randomly varying birefringence is likely the main source of error in the presented paper.

Research Article | Vol. 30, No. 22 / 24 Oct 2022 / Optics Express 40136
Optics EXPRESS

All-optical polarimeter for laser Stokes vector measurement using self-induced nonlinear phase modulation

OLE KRARUP,[1,2,*] CHAMS BAKER,[1] LIANG CHEN,[1] AND XIAOYI BAO[1]

[1] Fiber Optics Group, Department of Physics, University of Ottawa, Ottawa, K1N 6N5, Canada
[2] okrarup@uottawa.ca
[*] ole.krarup.dk@gmail.com

Abstract: This paper utilizes an analytical model of polarization dependent frequency sideband generation via the Kerr effect in a highly nonlinear fiber to determine the state of polarization (SOP) of a laser by all-optical means. Theoretical analysis shows that the power of the n^{th} order sideband generated by the propagation of two lasers with distinct frequencies in the nonlinear medium is proportional to $\cos^{2n}(\alpha/2)$, where α is the angle between the normalized Stokes vectors representing the SOPs of the lasers on the Poincaré sphere. By tailoring the SOP of one laser acting as a reference and experimentally measuring the power of the first order sideband, the SOP of the laser under test is recovered with an error smaller than 10.22° on the Poincaré sphere corresponding to 0.8% the sphere's total area. Comparing the SOPs of two lasers without referencing them to fixed polarizers enables potential applications in remote environmental sensing, novel polarization division multiplexing schemes for enhanced telecommunication data rates, and scientific instrumentation.

1. Introduction

Environmental sensing based on optical fibers has several advantages over methods based on electrical signals. These advantages include durability, small size, and immunity to electromagnetic interference, which make optical fibers ideal for collecting data in harsh environments. Fiber optical sensing systems detect changes in the surrounding environment by measuring variations in the amplitude, phase, frequency or polarization of light propagating in fibers. Particularly, variations in the state of polarization (SOP) of light caused by altered birefringence in the glass has been used to measure changes in applied strain, magnetic fields and ambient temperature [1–3]. To determine if two laser signals are co-polarized, it is typically necessary to launch them into a polarimeter, where their SOPs are determined with reference to physical polarizers whose orientations in space remain fixed. Directly measuring the degree of co-polarization of two lasers with respect to each other without the need for an external reference could enable novel sensing schemes and new approaches to polarimeter instrumentation.

All-optical signal processing refers to a collection of techniques for manipulating light with light, which is used in a variety of applications for overcoming limitations of conventional sensing methods [4–6]. For example, sidebands generated via nonlinear self-induced phase modulation have been used for extending the sensing range in chirped pulse optical time domain reflectometry (CP-OTDR) [7], refining the resolution of optical frequency domain reflectometry (OFDR) [8] and fiber optical sensors [9], increasing the sensitivity of fiber Bragg grating (FBG) based thermometers [10], and increasing the extinction ratio of pulses used for long range OTDR [11]. When attenuation and chromatic dispersion are neglected, the power of each sideband as a function of the powers of the input lasers can be calculated analytically [12], allowing for deeper insight into the behavior of sinusoidally modulated optical signals in a nonlinear

#467714 https://doi.org/10.1364/OE.467714
Journal © 2022 Received 13 Jun 2022; revised 29 Sep 2022; accepted 4 Oct 2022; published 14 Oct 2022

Optics EXPRESS

medium and enabling a variety of novel applications. Furthermore, if the wavelength dependence of randomly varying birefringence in the nonlinear medium is low, the power of the n^{th} order sideband is proportional to $\cos^{2n}(\alpha/2)$, where $0\circ \leq \alpha \leq 180\circ$ is the angle between the vectors representing the SOPs of the input lasers on the Poincaré sphere. This proportionality relation has been exploited to enhance the sensitivity of a polarimetric strain sensor [13]. In addition, the dependence on α suggests that the SOP of a signal laser can be recovered by launching it into a nonlinear medium along with a reference laser and measuring the power of the generated sidebands.

This paper presents an all-optical approach for polarimeter implementation, where the SOP of a signal laser is measured relative to the SOP of a reference laser without using polarizers for detection. An analytical model is developed for describing the impact of relative polarization between the two lasers on frequency sidebands generated by the Kerr effect. The results of this model are utilized to develop a new method for extracting the SOP of the signal laser from measurements of sideband power. The new polarimetric method is experimentally demonstrated by measuring the SOP of the signal laser with an error on the Poincaré sphere below 10.22°, corresponding to 0.8% of the sphere's total area. Limitations of the proposed technique are discussed along with potential applications for distributed polarimetric sensing, innovative polarization based multiplexing schemes for telecommunications and all-optical polarimeter instrumentation.

2. Theory

A detailed derivation of the following expressions is presented in [13]. Launching lasers at two different angular frequencies, ω_r and ω_s with $\omega_r > \omega_s$, into an optical fiber with a length, L, and a waveguide nonlinearity parameter, γ, the electric field amplitude at the input is given by

$$|A_{in}\rangle = \sqrt{P_s}\begin{pmatrix}\cos\theta\\ \sin\theta e^{i\phi}\end{pmatrix}e^{i\delta}e^{-i0.5\omega_d t} + \sqrt{P_r}\begin{pmatrix}\cos\beta\\ \sin\beta e^{i\xi}\end{pmatrix}e^{i0.5\omega_d t}, \tag{1}$$

where P_r and P_s are respectively the powers of the reference and the signal, $\omega_d = \omega_r - \omega_s$ is the angular frequency difference, β and θ are respectively the angles of the polarization vectors relative to the x-axis for the reference and the signal, ξ and ϕ are respectively the phase differences between the orthogonal polarization components of the fields for the reference and the signal, and δ is a phase delay between the two lasers. The power of the input field is $P_{in} = \langle A_{in}|A_{in}\rangle = P_r + P_s + 2\sqrt{P_r P_s}\cos(\alpha/2)\cos(\omega_d t + k)$, where α is the angle between the reference and signal fields when represented as vectors on the Poincaré sphere as visualized in Fig. 1(a), and k is a phase term that depends on the values of θ, β, ϕ, ξ and δ.

Neglecting dispersion, attenuation and random birefringence along the fiber, the Nonlinear Schrödinger Equation (NLSE) reduces to $\partial_z|A(z)\rangle = i\gamma\langle A|A\rangle|A(z)\rangle$, which is solved analytically to obtain an expression for the power of the n^{th} order sideband, $P_n = \langle A_n|A_n\rangle = P_s J_{n+1}^2(\phi_{\mathrm{NL}}) + P_r J_n^2(\phi_{\mathrm{NL}})$, where $\phi_{\mathrm{NL}} = 2\gamma L\sqrt{P_r P_s}\cos(\alpha/2)$. Introducing the normalization, $x = \gamma L P_r$, $y = \gamma L P_s$, $z_n = \gamma L P_n$, and applying the asymptotic approximation of the Bessel functions for $n>0$ and $0<\phi_{\mathrm{NL}}<\sqrt{1+n}$ leads to

$$z_n \approx \frac{x^n y^{n+1}}{[n!]^2}\cos^{2n}(\alpha/2) = Z_{\max,\mathrm{n}}\cos^{2n}(\alpha/2). \tag{2}$$

For an arbitrary SOP of the signal laser represented using the normalized Stokes formalism, $\hat{S} = (a, b, c)^T$, and a polarization for the reference laser along the X-direction, $\hat{X} = (1, 0, 0)^T$, the relative angle is $\alpha_X = \arccos(\hat{S}\cdot\hat{X}) = \arccos(a)$. The power of the first order sideband given a reference laser SOP along $\hat{X}$ is $P_{1,X}$, abbreviated as P_X, and is given by $P_X = P_{\max}\cos^2(\alpha_X/2)$,

Optics EXPRESS

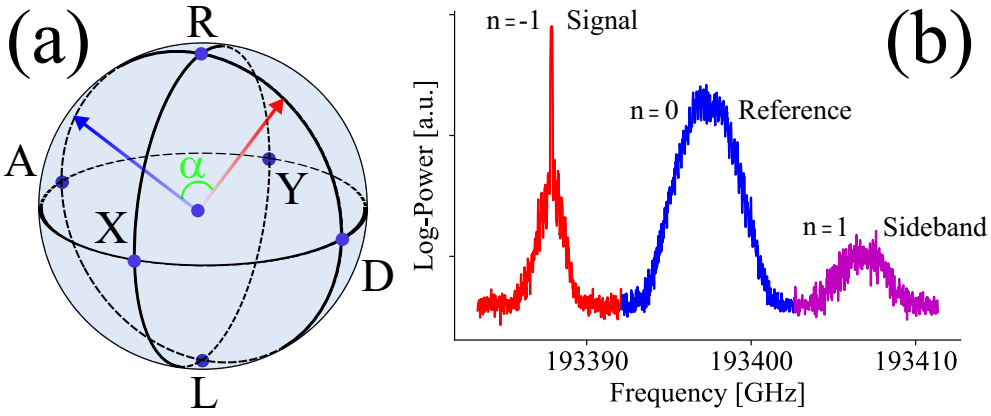

Fig. 1. (a) Visualization of the angle, α, between the SOP of a reference pulse and the SOP of the signal laser represented on the Poincaré sphere. (b) Optical spectrum measured after the Kerr medium.

where $P_{\max} = Z_{\max,1}/(\gamma L)$, implying that $\alpha_X = 2\arccos(\sqrt{P_X/P_{\max}}) = \arccos(a)$. Using the identity, $2\arccos(u) = \arccos(2u^2 - 1)$ [14], shows that $a = 2P_X/P_{\max} - 1$. Similarly, a reference laser SOP along the Y-direction, $\hat{Y} = (-1, 0, 0)^T$, yields $-a = 2P_Y/P_{\max} - 1$. Adding the expressions for a and $-a$ shows that $P_{\max} = P_X + P_Y$. Therefore, if the sideband powers, P_X and P_Y, generated by reference lasers with SOPs corresponding to $\hat{X}$ and $\hat{Y}$ are measured, the Stokes component, a, of the signal SOP can be calculated from $a = 2P_X/(P_X + P_Y) - 1$. This analysis can be repeated for $\hat{D} = (0, 1, 0)$ and $\hat{A} = (0, -1, 0)$ corresponding to light polarized along the +45° diagonal and –45° anti-diagonal respectively, as well as $\hat{R} = (0, 0, 1)$ and $\hat{L} = (0, 0, -1)$ corresponding to right hand circular light and left hand circular light. Doing so yields the following expression for the measured SOP of the signal laser,

$$\hat{S}^{(\text{measured})} = \begin{pmatrix} 2\frac{P_X}{P_X+P_Y} - 1 \\ 2\frac{P_D}{P_D+P_A} - 1 \\ 2\frac{P_R}{P_R+P_L} - 1 \end{pmatrix}. \tag{3}$$

Thus, the SOP of a signal laser can be determined from measurements of the power values of the 1st order sideband produced by sending the signal laser into a highly nonlinear fiber along with reference laser pulses polarized along the six cardinal directions on the Poincaré sphere.

3. Experimental setup and results

The experimental setup utilized to conduct all-optical measurements of the SOP of a signal laser is presented in Fig. 2(a). Figures 2(b)-(e) show the power as a function of time and the power spectral density (PSD) of the light at different points along the optical path. The reference signal is generated by a laser (Laser-R, PS-NLL-1550, TeraXion) emitting at 193397.436 GHz (1550.217 nm) and passed through two Electro Optical Modulators (EOM1, MXPE-LN-10, Photline) (EOM2,OC-192 Modulator, JDS uniphase) driven by a dual pulse generator (DPG, 8130A, Hewlett Packard). To minimize the pedestal of the generated pulses and maximize the extinction ratio, the DPG output is disabled and the DC bias of each modulator is adjusted to minimize the power transmitted through the EOMs, as monitored using a dual port power meter (DPM, ML910B, Anritsu). The DPG is then set to emit 1 ns electrical pulses from both output ports, and the time delay between the two electrical pulses is tuned to ensure that EOM2 only

Optics EXPRESS

transmits when it receives an optical pulse from EOM1. Using two EOMs further ensures that leakage of continuous wave (CW) light from Laser-R is minimized, leading to a reduction in measurement distortion. The reference pulse is amplified using a polarization maintaining erbium doped fiber amplifier (PM-EDFA, EDFA100P, Thorlabs) and a high power EDFA (HP-EDFA1, APEDFA-C-10-B-FA, Amonics). Subsequently, the reference light passes through a bandpass filter (BPF1, Ultra Narrow Filter, AOS) and is aligned with a polarizer (POL-R) by adjusting a polarization controller (PC-R). Using a primary 1x6 coupler, the reference pulse is split into six different branches, each containing a polarization controller (PC-(1-6)) and a variable optical attenuator (VOA-(1-6)), whereupon a secondary 1x6 coupler recombines the pulses from all six branches. The lengths of the branches are tailored such that the six 1 ns pulses exit the secondary 1x6 coupler with a delay of 5 ns between neighbouring pulses, as illustrated in Fig. 2(b), to minimize power fluctuations caused by interference due to temporal overlap. The six reference pulses are then amplified by an EDFA (AEDFA-PA-25-B-FA, Amonics) followed by a HP-EDFA (HP-EDFA2, AEDFA-33-B-FA, Amonics) before passing through a 3 GHz bandpass filter (BPF2, TFC, TeraXion). Upon reaching a 1:99 coupler (C1), 1% of the propagating light is sent to a photodiode (PD1, DSC10H, Discovery Semiconductors Inc.) attached to an oscilloscope (infiniium DSO81204B, Agilent) sampling at 40 GSa/s. Using the trace measured by the scope, the VOA's are adjusted to ensure that all six pulses have identical peak powers. The remaining 99% of the reference light from C1 is passed to a 50:50 coupler (C2).

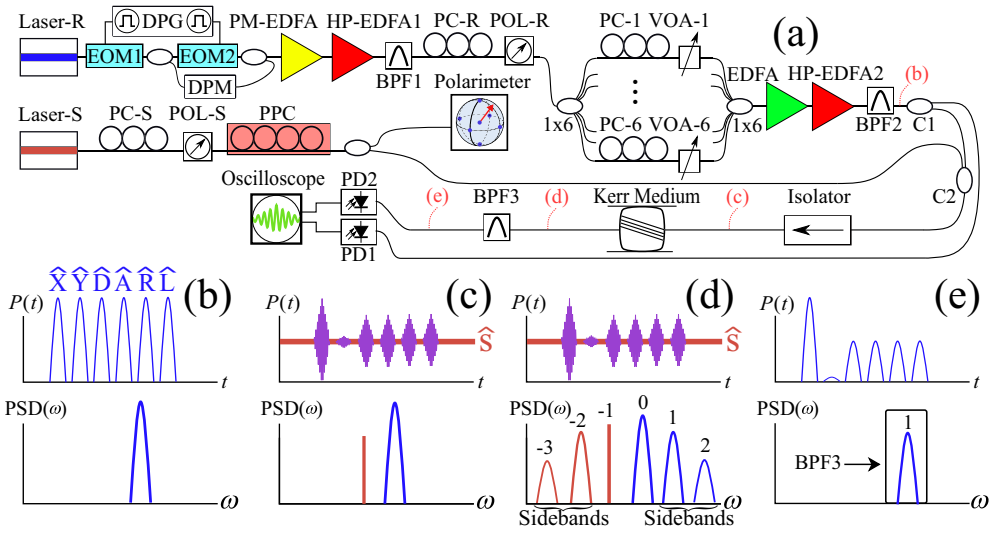

Fig. 2. (a) The experimental setup used for measuring the state of polarization, $\hat{S}$, of the signal laser using sidebands generated via the Kerr effect. (b-e): The light in the time- and angular frequency domains at different points along the optical path. Six reference pulses with polarizations aligned along the cardinal directions on the Poincaré sphere will experience different amounts of nonlinear phase modulation when interfering with the signal as described by Eq. (2). From the relative powers of the pulses measured when filtering out the 1st order sideband, the state of polarization of the signal can be recovered using Eq. (3).

The signal is generated by a distributed feedback laser (DFB) (Laser-S, NLK1556STG, NEL) emitting CW light at 193388.123 GHz (1550.211 nm). The signal polarization is aligned with the transmission axis of POL-S by adjusting PC-S, and then is passed through a programmable polarization controller (PPC, 11896A, Hewlett Packard). A coupler directs 10% of the signal power to a conventional polarimeter (IPM5300, Thorlabs) and the remaining 90% is combined with the six reference pulses using C2. The power of the CW signal is low enough to avoid

Optics EXPRESS

stimulated Brillouin scattering (SBS) that can distort the measurement. The combined signal and reference light is then passed through an optical isolator to a 5.7 km highly nonlinear fiber (418SG 04611A, Draka Comteq) that leads to the generation of frequency sidebands with a spacing of 9.312 GHz equal to the frequency separation between the signal- and the reference laser. Using a bandpass filter (BPF3, XTM-50, EXFO) light in the 1st order sideband at 193406.749 GHz (1550.062 nm) is extracted and detected using a photodiode (PD2, Model 1592 3.5GHz, New Focus) connected to the oscilloscope, which averages 512 traces to reduce the impact of electrical noise and optical power fluctuations.

To calibrate the setup, the PPC is adjusted such that the SOP of the signal as measured by the conventional polarimeter is along $\hat{X}$. Then, PC-1 and PC-2 are adjusted until the detected power of the first sideband pulse is maximized and the detected power of the second sideband pulse is minimized. For additional accuracy, the signal SOP is changed to $\hat{Y}$ using the PPC, whereupon the power of the first sideband pulse is minimized and the power of the second sideband pulse is maximized. Setting the signal SOP to $\hat{D}$ and $\hat{A}$, the procedure is repeated for sideband pulses 3 and 4. Finally, the same procedure is carried out for SOPs corresponding to $\hat{R}$ and $\hat{L}$ to correctly align sideband pulses 5 and 6. (Dataset 1, Ref. [15]).

Having calibrated the polarizations of the reference pulses, the setup is ready to measure any SOP of the signal. A set of 20 consecutive signal SOPs is generated using the PPC and for each SOP, the peak powers of the six sideband pulses are extracted, whereupon the Stokes parameters are determined using Eq. (3). The Stokes parameters of each signal SOP are also measured by the conventional polarimeter and presented in Figs. 3(a)-(b), showing close agreement with the measurements obtained using the proposed setup. To characterize the measurement error, the angle error, α_{err}, between the Stokes vectors obtained using the conventional polarimeter and the proposed setup is obtained for 190 random signal SOPs, showing that $\alpha_{\text{err,max}} = 10.22°$. The surface area of a spherical cap for a cone with an apex angle of $2\alpha_{\text{err,max}}$ comprises an error area corresponding to $\Omega_{\text{err,max}}/4\pi = 0.8\%$ of the surface of the Poincaré sphere. The error area implies that for a Stokes vector measured using the current setup, the true Stokes vector will at worst be located within a patch centered at the measurement corresponding to 0.8% of the total area of the sphere. In Fig. 3(c), a histogram of the 190 measured values of $\Omega_{\text{err}}/4\pi$ in percentage is presented, which indicates that approximately 70% of measurements have $\Omega_{\text{err}}/4\pi$ below 0.4%.

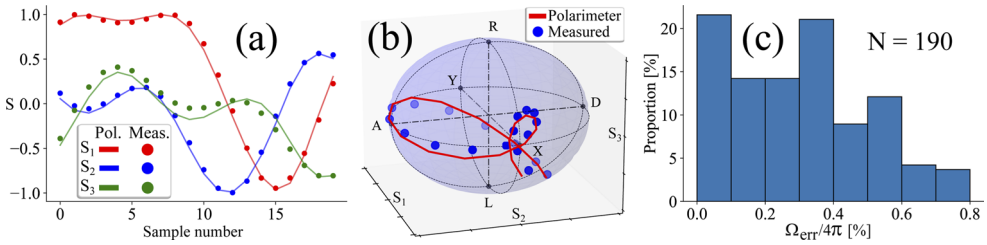

Fig. 3. (a) Stokes parameters for a 20-step sweep of polarizations with lines indicating the SOP determined by a conventional polarimeter and the data points representing the SOP determined from measurements according to Eq. (3). (b) The SOP according to the polarimeter and the measured SOP represented on the Poincaré sphere. Figure generated using [16]. (c) Histogram of N = 190 values of the area created by a spherical cap with an apex angle of $2\alpha_{\text{err}}$ compared to the total area of the unit sphere, where α_{err} is the angle on the Poincaré sphere between the measured SOP and the SOP according to the polarimeter. The maximum value of α_{err} is 10.22°, corresponding to 0.8% of the area of the Poincaré sphere. The discrepancy in (a) between the value of S_3 measured by the conventional polarimeter and the value obtained using the presented method as well as the maximum value of α_{err} are attributed to an imperfect calibration of the SOPs of the referenced pulses caused by randomly varying birefringence in the Kerr medium

Optics EXPRESS

4. Discussion

The model for polarization dependent sideband generation relies on simplifying assumptions. Attenuation in the Kerr medium is ignored, but can be accounted for by replacing the length of the fiber, L, with the effective length, $L_{\text{eff}} = (1 - \exp(-\alpha_L L))/\alpha_L$, where α_L is the attenuation coefficient. Dispersion is assumed to be negligible, which is a valid assumption when the dispersion length, L_D, is much greater than the nonlinear length, L_{NL}, where $L_D = 2\pi c T_0^2/\lambda^2 D$, c is the speed of light, T_0 is the pulse duration, λ is the wavelength of the light, D is the chromatic dispersion, and $L_{\text{NL}} = 1/\gamma P$. Using $T_0 = 2\pi/4\omega_d = 27$ ps corresponding to the full width at half maximum of one beat cycle, $\lambda = 1550$ nm and $D = 3$ ps/(nm·km) as reported in [17] leads to $L_D \approx 190$ km. In comparison, the presented model for sideband generation is valid when $0 < \phi_{\text{NL}} < \sqrt{1+n}$, implying that using $2\gamma LP = \phi_{\text{NL}} < 1$ with $P = \sqrt{P_r P_s}$ leads to $L_{\text{NL}} = 1/\gamma P \approx 2L \approx 11.4$ km, indicating that chromatic dispersion can be neglected. The model also neglects the impact of wavelength dependent random birefringence in the Kerr medium. Previous results indicate that for $\omega_d/2\pi \approx 10$ GHz, the total drift in the SOP at the end of the Kerr medium utilized in this experiment amounts to at most 8.58° on the Poincaré sphere [13]. Therefore, neglecting the drift in the relative SOP when the signal and reference propagate through the Kerr medium is valid for the purpose of deriving Eq. (2). However, when calibrating the SOP of the reference pulses by minimizing their power, the SOP drift introduced by wavelength dependent random birefringence means that even if the SOPs are orthogonal at the input of the fiber, some sideband power will always be produced at its output. Therefore, it is not possible to consistently achieve a perfect calibration of the reference pulses. Ideal calibration of the reference pulses can be achieved using a Kerr medium with less wavelength dependent randomly varying birefringence or simply by using a shorter fiber length.

The presented experiment utilizes six reference pulses polarized along the cardinal directions on the Poincaré sphere to recover the SOP of the signal. Utilizing six pulses ensures that the signal SOP is always close to at least one of the references, guaranteeing the measurement of a strong signal inside the dynamic range of the detector. Furthermore, the use of six reference pulses makes the derivation of Eq. (3) and the calibration of the setup simple, but overdetermines the system of equations to be solved. An alternate configuration using only four reference pulses whose SOPs on the Poincaré sphere form a tetrahedron also allows for the determination of the SOP of the signal laser. However, using only four reference pulses increases the complexity of the analysis and increases the measurement error as the signal SOP is less likely to be close to one of the reference SOPs.

In this experiment, imperfections in the electronics of the DPG lead to the generation of pulses that have a high power peak with a duration of 1 ns followed by a low power tail. Along with the effect of wavelength dependent random birefringence, the overlap of the tail of one pulse with the peak of next pulse impedes efforts to consistently calibrate the system. The issue of overlapping pulses can be solved by enhancing the extinction ratio of the pulse generated by the DPG [11]. Enhancing the pulse extinction ratio would allow a closer spacing between the reference pulses, which in turn would allow for a higher sampling rate. Using six pulses spaced 5 ns apart implies a theoretical maximum sampling rate of $1/(6 \cdot 5\text{ ns}) = 33.3$ MHz. If the tails of the 1 ns pulses are eliminated and a 4-pulse scheme is utilized, the maximum theoretical sampling rate would be $1/(4 \cdot 1\text{ ns}) = 250$ MHz. Alternatively, in a more complex system where the signal is split so that measurements can be conducted in parallel, the measurement rate only depends on the duration of the reference pulse, which for a 1 ns pulse is 1 GHz. Furthermore, the duration of the reference pulse must be longer than $T_d = 2\pi/\omega_d$, which cannot be made arbitrarily small because an increased value of ω_d increases the error that arises from wavelength dependent random birefringence.

The all-optical signal processing method described in this paper allows the SOPs of two lasers to be compared to each other directly without referencing them to polarizers. A conventional

Optics EXPRESS

measurement, which also avoids polarizers, could be conducted by shining the two lasers onto the same photodiode and adjusting their polarizations to maximize or minimize the recorded power of the generated beat tone, but the largest ω_d that can be used in such an experiment is limited by smallest cutoff frequency of the employed electronics. Apart from instrumentation of an all-optical polarimeter, another potential application of direct comparison of the SOPs of two lasers is telecommunications. Just as quadrature amplitude modulation (QAM) relies on measuring the phase difference between the signal laser pulses and a reference laser acting as a local oscillator, the presented method enables measuring the SOP of a signal laser with respect to a reference laser allowing for advanced polarization division multiplexing (PDM) where each point on the Poincaré sphere serves as a channel as visualized in Fig. 4 and experimentally investigated in [18]. Even though the experimental setup presented in this work is costly and implementing advanced PDM requires further expensive additions to allow for parallel detection of the Stokes components, this PDM approach will increase the bandwidth of existing systems by at least 1 order of magnitude making the high cost of the system negligible in comparison to the price of installing additional undersea fiber cables. Furthermore, future advances in photonic integrated circuits (PIC) would allow the system to be implemented on a single chip.

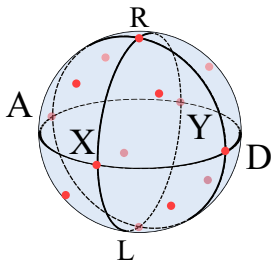

Fig. 4. Visualization of advanced polarization division multiplexing scheme with channels represented by red dots located at the cardinal directions of the Poincaré sphere and at the center of each octant.

Enhanced sensitivity to changes in polarization for the power of higher order sidebands was demonstrated in [13]. If a sideband order higher than $n = 1$ is used in the present experiment, the Stokes component, a, in $\hat{S} = (a, b, c)^T$ is given by $a = 2P_X^{1/n}/(P_X^{1/n} + P_Y^{1/n}) - 1$, which makes the measured SOP more sensitive for values of α_X close to 180° and less sensitive for values closer to 0°. Extracting multiple sidebands separately could therefore provide a way to measure the SOP with enhanced sensitivity for a range of different angles. Such a flexible approach to enhanced sensitivity could be useful in sensing schemes based on polarization-OTDR when detecting small variations in the SOP caused by environmental disturbances [19].

The presented analysis only utilizes the power of the 1st order sideband but the model derived in [13] allows the SOPs of the sidebands to be predicted. The model relates the SOPs of the sidebands to the properties of the incident light including optical powers, initial SOPs and relative phase of the two lasers. The dependence of the SOP of the sidebands on the properties of the signal laser and the reference laser provides versatile approaches for environmental sensing. Additionally, optical pulses with time dependent SOPs have been utilized for the characterization of material surfaces [20]. Further practical advantages of determining the SOPs of the sidebands will be a subject of future investigation.

5. Conclusion

A method for measuring the SOP of a laser based on an analytical model for polarization dependent frequency sideband generation and all-optical signal processing is demonstrated. Results show that the SOP can be determined with an error of 10.22°, which corresponds to 0.8%

Optics EXPRESS

of the area of the Poincaré sphere. The presented technique allows for the measurement of the SOP of a signal laser using a reference laser with the potential to increase telecommunication data rates, improve the sensitivity of distributed environmental sensors and enable novel approaches for polarimetric instrumentation.

Funding. Canada Research Chairs (75-67138); Natural Sciences and Engineering Research Council of Canada (DG-2020-06302).

Disclosures. The authors declare no conflicts of interest.

Data availability. Data underlying the results presented in this paper are available in Dataset 1, Ref. [15].

References

1. A. J. Rogers, "Polarization-optical time domain reflectometry: a technique for the measurement of field distributions," Appl. Opt. **20**(6), 1060–1074 (1981).
2. R. H. Stolen and E. H. Turner, "Faraday rotation in highly birefringent optical fibers," Appl. Opt. **19**(6), 842–845 (1980).
3. H. Zhang, Y. Dong, J. Leeson, L. Chen, and X. Bao, "High sensitivity optical fiber current sensor based on polarization diversity and a Faraday rotation mirror cavity," Appl. Opt. **50**(6), 924–929 (2011).
4. A. E. Willner, S. Khaleghi, M. R. Chitgarha, and O. F. Yilmaz, "All-optical signal processing," J. Lightwave Technol. **32**(4), 660–680 (2014).
5. C. J. McKinstrie, S. Radic, and A. H. Gnauck, "All-optical signal processing byfiber-based parametric devices," Opt. Photonics News **18**(3), 34–40 (2007).
6. G. Moille, E. F. Perez, J. R. Stone, A. Rao, X. Lu, T. S. Rahman, Y. K. Chembo, and K. Srinivasan, "Ultra-broadband Kerr microcomb through soliton spectral translation," Nat. Commun. **12**(1), 7275 (2021).
7. Y. Wang, O. Krarup, L. Chen, and X. Bao, "Frequency sweep extension using the kerr effect for static temperature measurement range enhancement in chirped pulse ϕ-otdr," Opt. Express **29**(15), 23202–23212 (2021).
8. B. Wang, X. Fan, S. Wang, J. Du, and Z. He, "Millimeter-resolution long-range ofdr using ultra-linearly 100 ghz-swept optical source realized by injection-locking technique and cascaded fwm process," Opt. Express **25**(4), 3514–3524 (2017).
9. O. Krarup, C. Baker, L. Chen, and X. Bao, "Nonlinear resolution enhancement of an fbg based temperature sensor using the kerr effect," Opt. Express **28**(26), 39181–39188 (2020).
10. J. Du and Z. He, "Sensitivity enhanced strain and temperature measurements based on fbg and frequency chirp magnification," Opt. Express **21**(22), 27111–27118 (2013).
11. B. Vanus, C. Baker, L. Chen, and X. Bao, "High extinction ratio optical pulse characterization method via single-photon counting," Appl. Opt. **60**(1), 20–23 (2021).
12. A. Boskovic, S. V. Chernikov, J. R. Taylor, L. Gruner-Nielsen, and O. A. Levring, "Direct continuous-wave measurement of n2 in various types of telecommunication fiber at 1.55 μm," Opt. Lett. **21**(24), 1966–1968 (1996).
13. O. Krarup, C. Baker, L. Chen, and X. Bao, "Sensitivity enhancement of fiber optical polarimetric sensors using self-induced nonlinear phase modulation via the Kerr effect," Opt. Express **30**(9), 13985–13993 (2022).
14. "*NIST Digital Library of Mathematical Functions*," https://dlmf.nist.gov/4.24#E14, Release 1.0.27 of 2020-06-15. F. W. J. Olver, A. B. Olde Daalhuis, D. W. Lozier, B. I. Schneider, R. F. Boisvert, C. W. Clark, B. R. Miller, B. V. Saunders, H. S. Cohl, and M. A. McClain, eds.
15. O. Krarup, "Kerr polarimeter data," figshare (2022), https://doi.org/10.6084/m9.figshare.19604233.
16. J. del Hoyo, L. M. Sanchez-Brea, and A. Soria-Garcia, "Open source library for polarimetric calculations py_pol," in *Computational Optics 2021*, vol. 11875 D. G. Smith, F. Wyrowski, and A. Erdmann, eds., International Society for Optics and Photonics (SPIE, 2021), pp. 12–20.
17. C. Baker, L. Chen, and X. Bao, "Sensitivity enhancement beyond the wavelength limit in a novel sub-micron displacement sensor," Opt. Express **23**(14), 17838–17844 (2015).
18. Q. Xiang, Y. Yang, Q. Zhang, and Y. Yao, "Joint, accurate and robust optical signal-to- noise ratio and modulation format monitoring scheme using a single stokes-parameter-based artificial neural network," Opt. Express **29**(5), 7276–7287 (2021).
19. M. Wuilpart, A. Gusarov, P. Moreau, W. Leysen, and P. Mégret, "Use of a polarization otdr for the measurement of plasma current in the tore supra thermonuclear fusion reactor," in *Advanced Photonics 2017 (IPR, NOMA, Sensors, Networks, SPPCom, PS)*, (Optical Society of America, 2017), p. SeW2E.5.
20. C. K. Keyser, R. K. Martin, H. Lopez-Aviles, K. Nguyen, A. M. Adams, and D. Christodoulides, "Single-pulse, Kerr-effect Mueller matrix LiDAR polarimeter," Opt. Express **28**(9), 13694–13713 (2020).

Chapter 8

Summary, future work and conclusion

8.1 Summary

The research conducted in this thesis seeks to enhance the performance of fiber optical environmental sensors beyond what is possible with conventional methods by developing new ways of processing sensor signal using nonlinear effects. Limiting factors of commonly applied fiber optical sensing schemes were highlighted and it was explained how frequency sidebands generated via the Kerr effect as described using a general vector model can overcome these limitations. Four peer reviewed papers were presented, demonstrating the validity of the theoretical principles through concrete experiments.

The first paper shows how the fact that sideband power is proportional to integer exponents of the laser powers launched into a nonlinear fiber can be exploited to enhance the resolution of a fiber optical temperature sensor by a factor of 3.35 with potential applications in industrial monitoring, spectroscopy and imaging.

The second paper, written collaboratively, demonstrates how the response of higher order sidebands to changes in the frequency difference between the input lasers can be exploited to extend the chirping rate of chirped optical pulses having durations on the scale of nanoseconds by factors up to 6 with applications in photonics, range-finding and sensing.

The third paper validates the vector model of sideband generation by showing that the predicted increase in the sensitivity of a polarimetric sensor matches the one determined experimentally. The experimentally measured increase in the polarimetric sensitivity by a factor of 1.45 is consistent with the predicted value of 1.55 resulting from the fundamental effects described by the model. The technique allows the sen-

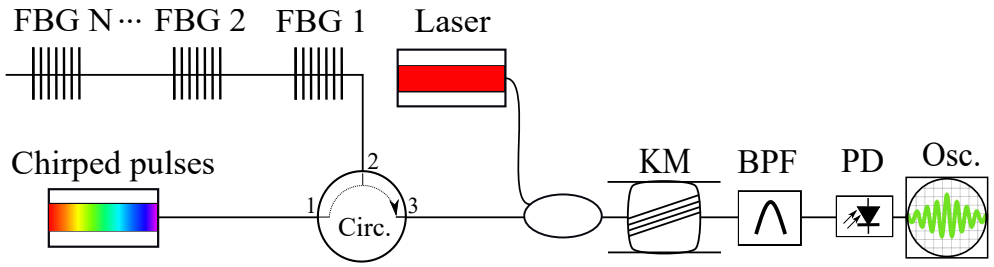

Figure 8.1: Proposed setup for applying resolution enhancement to distributed sensing. A chirped pulse with a frequency range greater than the bandwidth of an array of identical, weak FBGs produces a signal consisting of a pulse train, where the arrival time of the peak of each pulse depends on the temperature of the corresponding grating. By using the Kerr effect to potentiate this signal, the resolution of each FBG sensor can be enhanced.

sitivity of fiber optical polarimetric sensors measuring strain and magnetic fields to be enhanced.

Finally, the fourth paper utilizes the vector model to develop a novel approach for measuring the SOP of a laser by all-optical means with applications in scientific instrumentation and polarization division multiplexing for telecommunications.

8.2 Future work

The experiments presented in this thesis involve relatively simple, point-like sensors to highlight the impact of optical signal processing using the Kerr effect. Having demonstrated the validity of the theoretical analysis and the mechanisms for enhancing resolution, chirping range and polarimetric sensitivity, these techniques can now be applied to more sophisticated sensor types.

For example, since the magnitude of the resolution enhancement effect detailed in Chapter 4 depends on the inherent shape of the FBG spectrum, gratings with sharper spectra, such as π-shifted gratings or a weak grating whose bandwidth is given by Eq. 2.13 will benefit more from resolution enhancement than the strong gratings shown in Fig. 2.1(e). Thus, to increase the resolution of a distributed measurement system, resolution enhancement can be applied to the signal generated by using a chirped pulse with a wide frequency range to interrogate an array of weak FBGs inscribed at regular intervals in a fiber as visualized in Fig. 8.1. Furthermore, the ability to generate an optical output signal, which is an integer exponent of the input signal could find uses in analog optical computers, which have been proposed for solving specialized problems in areas such as machine learning with better performance than digital electronic methods [99].

Given a chirped pulse generated by one of the methods listed in Tab. 2.1, the method described in Chapter 5 not only produces one pulse with an increased chirp-

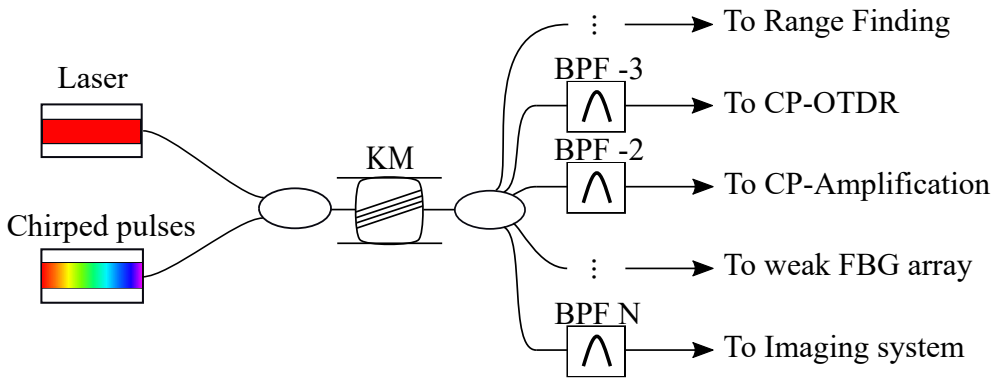

Figure 8.2: Proposed setup for generating a large number of mutually coherent chirped pulses with different chirping rates for different technical applications, including the one suggested in Fig. 8.1.

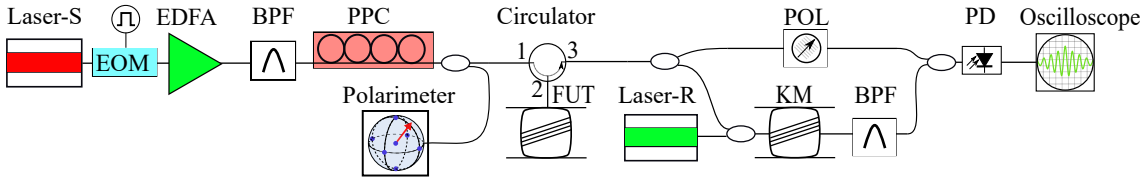

Figure 8.3: Setup diagram of proposed experiment for investigating enhanced P-OTDR. A reference P-OTDR trace is generated using a conventional polarizer, while an enhanced trace is generated by launching the light backscattered from the FUT into a Kerr medium along with a reference laser to generate sidebands, whose powers are given by Eq. 3.72, which can be individually extracted using a bandpass filter.

ing rate, but a whole set of coherent pulses at different frequencies with different chirping rates, including ones where the chirping direction is reversed. Thus, the presented technique can be exploited for the instrumentation of a device, which can provide mutually coherent, chirped optical pulses with a range of chirping rates for scientific, industrial and sensing applications as visualized in Fig. 8.2 [100, 101, 102]. For example, flexibly choosing the chirping rate of the pulses in the setup proposed in Fig. 8.1 while keeping their durations fixed would allow one to adjust the duration of the signal pulses from the FBG array before resolution enhancement is applied.

With regards to Chapter 6, the increased sensitivity to changes in polarization for higher order sidebands predicted by Eq. 3.72 can be exploited to enhance polarization-OTDR (P-OTDR) sensing schemes [103]. Using the setup proposed in Fig. 8.3, where the same P-OTDR signal from a FUT is sent to both a conventional polarizer following Malus' law and a to Kerr medium along with a reference laser, where the power of the generate sidebands follow Eq. 3.72, the increase in sensitivity to distributed changes in polarization can be investigated.

The polarimetry method presented in Chapter 7 might enable novel polarization division multiplexing schemes for telecommunication with constellation points distributed evenly over the surface of the Poincaré sphere. If the method is extended

to detect partially polarized light, constellation points could be placed inside the Poincaré sphere to further increase data rates. For such a technology to be deployed in telecommunication, miniaturizing the system to fit on a photonic chip would most likely be required.

The experiment in Chapter 7 uses a conventional polarimeter utilizing physical polarizers to calibrate the six reference pulses and to serve as a basis of comparison for the experimentally determined SOPs. However, calibrating the six reference pulses without relying on a conventional polarimeter is possible. Assuming for simplicity that the signal laser is polarized along $\hat{L}$, the six pulses extracted from the 1st order sideband will initially have random powers. First, the polarization of the sixth reference pulse can be tuned until its corresponding sideband power is maximized, while the fifth reference pulse can be tuned until its corresponding sideband power is minimized. The fifth reference pulse is now aligned with the "north pole" of the Poincaré sphere, while the sixth reference pulse is aligned with its "south pole". Then, the SOP of the signal can be changed to ensure that the fifth and sixth sideband pulses have equal power, which can only happen when the signal SOP is located somewhere on the "equator" of the Poincaré sphere. Defining this equatorial signal SOP as the $\hat{A}$ polarization, the polarization of the fourth reference pulse can then be adjusted to maximize its corresponding sideband power, while the polarization of the third reference pulse is altered to minimize its corresponding sideband power. Finally, the SOP of the signal can be adjusted until sideband pulses three to six are all at half of their maximum powers, ensuring that the signal SOP is either along the $\hat{X}$ or $\hat{Y}$ directions. Repeating the process of maximizing and minimizing the respective sideband powers one final time for the two remaining pulses ensures that all six reference pulses are calibrated against the SOP of the signal without relying on external polarizers.

8.3 Conclusion

This thesis has explored new approaches to processing and enhancing signals from fiber sensors by exploiting nonlinear effects to conduct all-optical signal processing. The demonstrated improvements in resolution, range and sensitivity can be applied to existing fiber sensors monitoring critical, high-value infrastructure and provide avenues for developing new sensing schemes. Furthermore, the presented techniques can be extended to related fields including spectroscopy, imaging and telecommunications. By adding a small contribution to centuries of studies in optics, this thesis will hopefully inspire further research into practical applications of manipulating light with light.

Bibliography

[1] K. O. Hill, Y. Fujii, D. C. Johnson, and B. S. Kawasaki. Photosensitivity in optical fiber waveguides: Application to reflection filter fabrication. *Applied Physics Letters*, 32(10):647–649, 1978. arXiv:https://doi.org/10.1063/1.89881, doi:10.1063/1.89881.

[2] Chung E. Taylor, Henry F. & Lee. Apparatus and method for fiber optic intrusion sensing. Technical Report US5194847A, United States Patent, 1991. URL: https://patentimages.storage.googleapis.com/50/68/e7/7bff4f28e28b5e/US5194847.pdf.

[3] J. Pastor-Graells, H. F. Martins, A. Garcia-Ruiz, S. Martin-Lopez, and M. Gonzalez-Herraez. Single-shot distributed temperature and strain tracking using direct detection phase-sensitive otdr with chirped pulses. *Opt. Express.*, 24(12):13121–13133, Jun 2016. URL: http://www.opticsexpress.org/abstract.cfm?URI=oe-24-12-13121, doi:10.1364/OE.24.013121.

[4] Ole Krarup. Custom Nonlinear Schroedinger Equation solution in Jones formalism. URL: https://doi.org/10.6084/m9.figshare.16944094.

[5] Jeremy Stolow and Birgit Meyer. Enlightening religion: Light and darkness in religious knowledge and knowledge about religion. *Critical Research on Religion*, 9(2):119–125, 2021. arXiv:https://doi.org/10.1177/20503032211015276, doi:10.1177/20503032211015276.

[6] M. Suhail Zubairy. *A Very Brief History of Light*, pages 3–24. Springer International Publishing, Cham, 2016. doi:10.1007/978-3-319-31903-2_1.

[7] O. Darrigol. *A History of Optics from Greek Antiquity to the Nineteenth Century*. OUP Oxford, 2012. URL: https://books.google.ca/books?id=ImM62wvWE_cC.

[8] S. Halliwell. *Plato: Republic X*. Aris & Phillips Classical Texts. Liverpool University Press, 1988. URL: https://books.google.ca/books?id=gHBvEAAAQBAJ.

[9] D.C. Lindberg. *Theories of Vision from Al-kindi to Kepler*. Chicago History of Science and Medicine. University of Chicago Press, 1981. URL: https://books.google.ca/books?id=-8A_auBvyFoC.

[10] Christiaan Huygens. *Traité de la lumière*. Pieter van der Aa, 1690. URL: https://archive.org/details/bub_gb_X9PKaZlChggC.

[11] I. Newton. *Opticks:: Or, a Treatise of the Reflexions, Refractions, Inflexions and Colours of Light. Also Two Treatises of the Species and Magnitude of Curvilinear Figures.*. Eighteenth century collections online. Smith and Walford, 1704. URL: https://gallica.bnf.fr/ark:/12148/bpt6k3362k/f235.item#.

[12] M.O. Scully and M.S. Zubairy. *Quantum Optics*. Cambridge University Press, 1997. URL: https://books.google.ca/books?id=9lkgAwAAQBAJ.

[13] 1861-1941 Meyer, Kirstine Bjerrum. *Om Ole Rømers opdagelse af lysets tøven,*. Skrifter, naturvidenskabelig og mathematisk afdeling. A.F. Høst & Søn, Københavnn,, 1915. URL: https://da.wikisource.org/wiki/Om_Ole_R%C3%B8mers_Opdagelse_af_Lysets_T%C3%B8ven.

[14] H.Fizeau. Sur une experience relative a la vitesse de propagation de la lumière. *Comptes rendus hebdomadaires des séances de l'Académie des sciences*, pages 90–93, July 1849. URL: https://gallica.bnf.fr/ark:/12148/bpt6k2986m/f94.item.

[15] A. Einstein. Über die vom relativitätsprinzip geforderte trägheit der energie. *Annalen der Physik*, 328(7):371–384, 1907. URL: https://onlinelibrary.wiley.com/doi/abs/10.1002/andp.19073280713, arXiv:https://onlinelibrary.wiley.com/doi/pdf/10.1002/andp.19073280713, doi:10.1002/andp.19073280713.

[16] M. Planck and M. Masius. *The Theory of Heat Radiation*. P. Blakiston's Son & Company, 1914. URL: https://books.google.ca/books?id=1ekvAAAAIAAJ.

[17] Rune Mørup Greve Pommer. Den sene vikingetids amfibiske enhed. Master's thesis, Saxo Institute, University of Copenhagen, 2017.

[18] Judith McKenzie. *The Architecture of Alexandria and Egypt 300 B.C.–A.D. 700*. The Yale University Press Pelican History of Art Series. Yale University Press, 2011.

[19] R.W. Burns and Institution of Electrical Engineers. *Communications: An International History of the Formative Years*. Communications: An International History of the Formative Years. Institution of Engineering and Technology, 2004.

[20] D.R. Goff, K.S. Hansen, and M.K. Stull. *Fiber Optic Video Transmission: The Complete Guide*. Focal Press, 2003.

[21] A.G. Bell. Selenium and the Photophone1. *Nature*, 22(569):500–503, September 1880. doi:10.1038/022500a0.

[22] Manfred Börner. Mehrstufiges Übertragungssystem für in pulscodemodulation dargestellte nachrichten. Technical Report , DE1254513B, DEUTSCHES PATENTAMT, 1967. URL: https://worldwide.espacenet.com/patent/search/family/007557308/publication/DE1254513B?q=pn%3DDE1254513.

[23] K C Kao and T W Davies. Spectrophotometric studies of ultra low loss optical glasses i: single beam method. *Journal of Physics E: Scientific Instruments*, 1(11):1063–1068, nov 1968. doi:10.1088/0022-3735/1/11/303.

[24] Jeff. Hecht. *City of light : the story of fiber optics / Jeff Hecht*. Oxford University Press New York, 1999.

[25] E. Desurvire, J. R. Simpson, and P. C. Becker. High-gain erbium-doped traveling-wave fiber amplifier. *Opt. Lett.*, 12(11):888–890, Nov 1987. URL: http://opg.optica.org/ol/abstract.cfm?URI=ol-12-11-888, doi:10.1364/OL.12.000888.

[26] R.J. Mears, L. Reekie, I.M. Jauncey, and D.N. Payne. Low-noise erbium-doped fibre amplifier operating at 1.54μm. *Electronics Letters*, 23(19):1026–1028, 1987. URL: https://eprints.soton.ac.uk/78511/.

[27] Robert T. Weverka. Wavelength router. Technical Report , US 6,501,877 B1, United States Patent, 2002. URL: https://patentimages.storage.googleapis.com/6c/69/06/803ada4b2e8da9/US6501877.pdf.

[28] R. H. Stolen and E. P. Ippen. Raman gain in glass optical waveguides. *Applied Physics Letters*, 22(6):276–278, 1973. arXiv:https://doi.org/10.1063/1.1654637, doi:10.1063/1.1654637.

[29] A. Splett, C. Kurzke, and K. Petermann. Ultimate transmission capacity of amplified optical fiber communication systems taking into account fiber nonlinearities. *Proc. ECOC 1993*, 2:41–44, 01 1993.

[30] P. Poggiolini, Gabriella Bosco, Andrea Carena, Vittorio Curri, Yanchao Jiang, and Fabrizio Forghieri. A detailed analytical derivation of the gn model of non-linear interference in coherent optical transmission systems. *arXiv*, September 2012. URL: https://arxiv.org/abs/1209.0394.

[31] Gautam Hegde, S Asokan, and Gopalkrishna Hegde. Fiber bragg grating sensors for aerospace applications: a review. *ISSS Journal of Micro and Smart Systems*, pages 1–19, April 2022. URL: https://link.springer.com/article/10.1007/s41683-022-00101-z.

[32] Fiber Optic Sensing Association. Fosa case studies & papers. URL: https://www.fiberopticsensing.org/page/fosa-case-studies.

[33] A. Perot and Charles Fabry. On the Application of Interference Phenomena to the Solution of Various Problems of Spectroscopy and Metrology. *Astrophysical Journal*, 9:87, Feb 1899. URL: https://ui.adsabs.harvard.edu/abs/1899ApJ.....9...87P, doi:10.1086/140557.

[34] E. Hecht. *Optics*. Always learning. Pearson, 2014. URL: https://books.google.ca/books?id=ZakzngEACAAJ.

[35] Alan E. Willner, Salman Khaleghi, Mohammad Reza Chitgarha, and Omer Faruk Yilmaz. All-optical signal processing. *J. Lightwave Technol.*, 32(4):660–680, Feb 2014. URL: http://opg.optica.org/jlt/abstract.cfm?URI=jlt-32-4-660.

[36] Colin J. McKinstrie, Stojan Radic, and Alan H. Gnauck. All-optical signal processing byfiber-based parametric devices. *Opt. Photon. News*, 18(3):34–40, Mar 2007. URL: http://www.optica-opn.org/abstract.cfm?URI=opn-18-3-34, doi:10.1364/OPN.18.3.000034.

[37] Gregory Moille, Edgar F. Perez, Jordan R. Stone, Ashutosh Rao, Xiyuan Lu, Tahmid Sami Rahman, Yanne K. Chembo, and Kartik Srinivasan. Ultra-broadband Kerr microcomb through soliton spectral translation. *Nature Communications*, 12(1):7275, December 2021. doi:10.1038/s41467-021-27469-0.

[38] Yang Lu. *Study of the Kerr Phase-Interrogator and Its Applications*. PhD thesis, University of Ottawa, 11 2015. URL: https://ruor.uottawa.ca/handle/10393/33376?mode=full.

[39] Benoit Vanus. *All-Optical Signal Processing Using the Kerr Effect for Fiber-Based Sensors*. PhD thesis, University of Ottawa, 10 2021. URL: https://ruor.uottawa.ca/handle/10393/42827?mode=full.

[40] Royal Institution of Great Britain. *Notices of the Proceedings of the Meeting of the Members of the Royal Institution of Great Britain*. Number v. 14. 1896. URL: https://books.google.ca/books?id=ZrloHemOmUEC&pg=PA355&redir_esc=y#v=onepage&q&f=false.

[41] J. Chapront, M. Chapront-Touzé, and G. Francou. Determination of the lunar orbital and rotational parameters and of the ecliptic reference system orientation from LLR measurements and IERS data. *Astronomy and Astrophysics*, 343:624–633, March 1999. URL: https://ui.adsabs.harvard.edu/abs/1999A&A...343..624C.

[42] Augustin-Jean Fresnel and Gavin Richard (tr./ed.) Putland. On the calculation of the tints that polarization develops in crystalline plates, & postscript, February 2021. doi:10.5281/zenodo.4561712.

[43] J. Peatross and M. Ware. *Physics of Light and Optics*. Self-published online at optics.byu.edu/textbook, 2015. URL: https://optics.byu.edu/textbook.

[44] Ingemar Petermann. *Fibre Bragg Gratings : Characterization, Realization and Simulation*. PhD thesis, KTH, School of Information and Communication Technology (ICT), 01 2007. URL: http://www.diva-portal.org/smash/record.jsf?pid=diva2%3A12052&dswid=6318.

[45] *NIST Digital Library of Mathematical Functions*. http://dlmf.nist.gov/10.2.E1, Release 1.1.5 of 2022-03-15. F. W. J. Olver, A. B. Olde Daalhuis, D. W. Lozier, B. I. Schneider, R. F. Boisvert, C. W. Clark, B. R. Miller, B. V. Saunders,H. S. Cohl, and M. A. McClain, eds. URL: http://dlmf.nist.gov/10.2.E1.

[46] K.C. Kao and G.A. Hockham. Dielectric-fibre surface waveguides for optical frequencies. *Proceedings of the Institution of Electrical Engineers*, 113:1151–1158(7), July 1966. URL: https://digital-library.theiet.org/content/journals/10.1049/piee.1966.0189, doi:10.1049/piee.1966.0189.

[47] R. C. Alferness, C. H. Joyner, M. D. Divino, M. J. R. Martyak, and L. L. Buhl. Narrowband grating resonator filters in ingaasp/inp waveguides. *Applied Physics Letters*, 49(3):125–127, 1986. arXiv:https://doi.org/10.1063/1.97199, doi:10.1063/1.97199.

[48] Victor Chernyak and I. Immoreev. A brief history of radar. *Aerospace and Electronic Systems Magazine, IEEE*, 24:B1 – B32, 10 2009. doi:10.1109/MAES.2009.5282288.

[49] Whitlow W. L. Au and Douglas W. Martin. *Sonar Discrimination of Metallic Plates by Dolphins and Humans*. Springer US, Boston, MA, 1988. doi:10.1007/978-1-4684-7493-0_86.

[50] Tadeusz Gudra, Joanna Furmankiewicz, and Krzysztof Herman. *Bats Sonar Calls and its Application in Sonar Systems*, pages 209–234. BoD – Books on Demand, 09 2011. doi:10.5772/23199.

[51] George J Frye. Time domain reflectometry system having a current source for locating discontinuities in a transmission line. Technical Report US3434049A, United States Patent, 1965. URL: https://patents.google.com/patent/US3434049A/en.

[52] Wanseok Seo. *Fiber optic intrusion sensor investigation*. PhD thesis, Texas A&M University, 1994. Copyright - Database copyright ProQuest LLC; ProQuest does not claim copyright in the individual underlying works; Last updated - 2022-02-27. URL: https://www.proquest.com/docview/304154294.

[53] J.F. Weller L. Goldberg, H.F. Taylor. Feedback effects in a laser diode due to rayleigh backscattering from an optical fibre. *Electronics Letters*, 18:353–354(1), April 1982. URL: https://digital-library.theiet.org/content/journals/10.1049/el_19820241.

[54] John P. Dakin. Distributed optical fiber sensors. In John P. Dakin and Alan D. Kersey, editors, *Distributed and Multiplexed Fiber Optic Sensors II*, volume 1797, pages 76 – 108. International Society for Optics and Photonics, SPIE, 1993. URL: https://doi.org/10.1117/12.141304.

[55] Zinan Wang, Li Zhang, Song Wang, Naitian Xue, Fei Peng, Mengqiu Fan, Wei Sun, Xianyang Qian, Jiarui Rao, and Yunjiang Rao. Coherent phase-otdr based on i/q demodulation and homodyne detection. *Opt. Express.*, 24(2):853–858, Jan 2016. URL: http://www.opticsexpress.org/abstract.cfm?URI=oe-24-2-853, doi:10.1364/OE.24.000853.

[56] A E Alekseev, V S Vdovenko, B G Gorshkov, V T Potapov, and D E Simikin. A phase-sensitive optical time-domain reflectometer with dual-pulse diverse frequency probe signal. *Laser Physics*, 25(6):065101, apr 2015. doi:10.1088/1054-660x/25/6/065101.

[57] Gaosheng Fang, Tuanwei Xu, Shengwen Feng, and Fang Li. Phase-sensitive optical time domain reflectometer based on phase-generated carrier algorithm.

J. Lightwave Technol., 33(13):2811–2816, Jul 2015. URL: http://jlt.osa.org/abstract.cfm?URI=jlt-33-13-2811.

[58] H. Kogelnik. Filter response of nonuniform almost-periodic structures. *The Bell System Technical Journal*, 55(1):109–126, 1976. doi:10.1002/j.1538-7305.1976.tb02062.x.

[59] Isa Navruz and Ahmet Altuncu. Design of a chirped fiber bragg grating for use in wideband dispersion compensation. In *New Trends in Computer Networks*, 2005. URL: https://www.semanticscholar.org/paper/Design-of-a-chirped-Fiber-Bragg-Grating-for-Use-in-Navruz-Altuncu/c926ae44a6af9a195fb470872b0cc9ace7910b07.

[60] T. Erdogan. Fiber grating spectra. *Journal of Lightwave Technology*, 15(8):1277–1294, 1997. doi:10.1109/50.618322.

[61] EXFO. *High-power continuous tunable laser*, 2022. URL: https://www.exfo.com/en/products/lab-manufacturing-testing/optical-light-sources/t100s-hp/.

[62] Agilent. *Hewlett-Packard function generator (legacy)*. URL: https://testequipment.center/Product_Documents/Agilent-83640A-Specifications-E36D7.pdf.

[63] Govind Agrawal. Chapter 3 - group-velocity dispersion. In Govind Agrawal, editor, *Nonlinear Fiber Optics (Fifth Edition)*, Optics and Photonics, pages 57–86. Academic Press, Boston, fifth edition edition, 2013. doi:10.1016/B978-0-12-397023-7.00003-6.

[64] Keysight. *Agile Signal Generator (State of the art)*, 2021. URL: https://www.keysight.com/ca/en/assets/7018-04543/data-sheets/5992-0092.pdf.

[65] Govind Agrawal. Chapter 4 - self-phase modulation. In Govind Agrawal, editor, *Nonlinear Fiber Optics (Fifth Edition)*, Optics and Photonics, pages 87–128. Academic Press, Boston, fifth edition edition, 2013. doi:10.1016/B978-0-12-397023-7.00004-8.

[66] FORC-Photonics. *Commercially available Chirped FBG*, 2020. URL: https://www.forc-photonics.ru/en/fiber_gratings/standard_FBG_types/1/322.

[67] Ieee standard test procedures for antennas. *ANSI/IEEE Std 149-1979*, pages 1–144, 1979. doi:10.1109/IEEESTD.1979.120310.

[68] H. Poincaré. *Théorie mathématique de la lumière II.* Paris, G. Carré, 1892. URL: https://archive.org/details/thoriemathma00poin/page/306/mode/2up.

[69] Malus Étienne Louis. Mémoire sur la mesure du pouvoir réfringent des corps opaques. In *Bulletin de la Société philomathique de Pari*, volume 1-11, pages 77–81. Société philomathique de Paris, Paris, 6 edition, 1826. URL: https://hdl.handle.net/2027/chi.44245876?urlappend=%3Bseq=87.

[70] Prasad Dandu, Andrei Gusarov, Philippe Moreau, Willem Leysen, Sung-Moon Kim, Patrice Mégret, and Marc Wuilpart. Plasma current measurement in iter with a polarization-otdr: impact of fiber bending and twisting on the measurement accuracy. *Appl. Opt.*, 61(9):2406–2416, Mar 2022. URL: http://opg.optica.org/ao/abstract.cfm?URI=ao-61-9-2406, doi:10.1364/AO.443984.

[71] R. Y. Chiao, E. Garmire, and C. H. Townes. Self-trapping of optical beams. *Phys. Rev. Lett.*, 13:479–482, Oct 1964. URL: https://link.aps.org/doi/10.1103/PhysRevLett.13.479, doi:10.1103/PhysRevLett.13.479.

[72] Govind Agrawal. Chapter 2 - group-velocity dispersion. In Govind Agrawal, editor, *Nonlinear Fiber Optics (Fifth Edition)*, pages 27–56. Academic Press, Boston, fifth edition edition, 2013. doi:10.1016/B978-0-12-397023-7.00002-4.

[73] Robert W. Boyd. Chapter 1 - the nonlinear optical susceptibility. In Robert W. Boyd, editor, *Nonlinear Optics (Third Edition)*, pages 1–67. Academic Press, Burlington, third edition edition, 2008. URL: https://www.sciencedirect.com/science/article/pii/B9780123694706000010, doi:10.1016/B978-0-12-369470-6.00001-0.

[74] E. Schrödinger. An undulatory theory of the mechanics of atoms and molecules. *Phys. Rev.*, 28:1049–1070, Dec 1926. URL: https://link.aps.org/doi/10.1103/PhysRev.28.1049, doi:10.1103/PhysRev.28.1049.

[75] Eugene P. Gross. Structure of a quantized vortex in boson systems. *Il Nuovo Cimento (1955-1965)*, 20:454–477, 1961. URL: https://api.semanticscholar.org/CorpusID:121538191.

[76] Lev P. Pitaevskii. Vortex lines in an imperfect bose gas. *ZhETF*, 40:451–454, 1961. URL: http://www.jetp.ras.ru/cgi-bin/e/index/r/40/2/p646?a=list.

[77] Akira Hasegawa and Frederick Tappert. Transmission of stationary nonlinear optical pulses in dispersive dielectric fibers. i. anomalous dispersion. *Applied Physics Letters*, 23(3):142–144, 1973. arXiv:https://doi.org/10.1063/1.1654836, doi:10.1063/1.1654836.

[78] Thiab R Taha and Mark I Ablowitz. Analytical and numerical aspects of certain nonlinear evolution equations. ii. numerical, nonlinear schrödinger equation. *Journal of Computational Physics*, 55(2):203–230, 1984. URL: https://www.sciencedirect.com/science/article/pii/0021999184900032, doi:10.1016/0021-9991(84)90003-2.

[79] Govind Agrawal. Chapter 6 - polarization effects. In Govind Agrawal, editor, *Nonlinear Fiber Optics (Fifth Edition)*, Optics and Photonics, pages 193–244. Academic Press, Boston, fifth edition edition, 2013. doi:10.1016/B978-0-12-397023-7.00006-1.

[80] Govind Agrawal. Appendix b - numerical code for the nls equation. In Govind Agrawal, editor, *Nonlinear Fiber Optics (Fifth Edition)*, Optics and Photonics, pages 615–617. Academic Press, Boston, fifth edition edition, 2013. doi:10.1016/B978-0-12-397023-7.00015-2.

[81] A. Boskovic, S. V. Chernikov, J. R. Taylor, L. Gruner-Nielsen, and O. A. Levring. Direct continuous-wave measurement of n2 in various types of telecommunication fiber at 1.55 μm. *Opt. Lett.*, 21(24):1966–1968, Dec 1996. doi:10.1364/OL.21.001966.

[82] *NIST Digital Library of Mathematical Functions*. http://dlmf.nist.gov/10.12, Release 1.0.27 of 2020-06-15. F. W. J. Olver, A. B. Olde Daalhuis, D. W. Lozier, B. I. Schneider, R. F. Boisvert, C. W. Clark, B. R. Miller, B. V. Saunders,H. S. Cohl, and M. A. McClain, eds. URL: http://dlmf.nist.gov/10.12.

[83] *NIST Digital Library of Mathematical Functions*. http://dlmf.nist.gov/10.7.E3, Release 1.0.27 of 2020-06-15. F. W. J. Olver, A. B. Olde Daalhuis, D. W. Lozier, B. I. Schneider, R. F. Boisvert, C. W. Clark, B. R. Miller, B. V. Saunders,H. S. Cohl, and M. A. McClain, eds. URL: http://dlmf.nist.gov/10.7.3.

[84] Bin Wang, Xinyu Fan, Shuai Wang, Jiangbing Du, and Zuyuan He. Millimeter-resolution long-range ofdr using ultra-linearly 100 ghz-swept optical source realized by injection-locking technique and cascaded fwm process. *Opt. Express.*, 25(4):3514–3524, Feb 2017. doi:10.1364/OE.25.003514.

[85] Jiangbing Du and Zuyuan He. Sensitivity enhanced strain and temperature measurements based on fbg and frequency chirp magnification. *Opt. Express.*, 21(22):27111–27118, Nov 2013. doi:10.1364/OE.21.027111.

[86] Eric W. Weisstein. Harmonic addition theorem. From MathWorld—A Wolfram Web Resource. Last visited on 20/05/2021. URL: https://mathworld.wolfram.com/HarmonicAdditionTheorem.html.

[87] Ole Krarup, Chams Baker, Liang Chen, and Xiaoyi Bao. Nonlinear resolution enhancement of an fbg based temperature sensor using the kerr effect. *Opt. Express*, 28(26):39181–39188, Dec 2020. doi:10.1364/OE.411179.

[88] P.V. Mamyshev. All-optical data regeneration based on self-phase modulation effect. In *24th European Conference on Optical Communication. ECOC '98 (IEEE Cat. No.98TH8398)*, volume 1, pages 475–476 vol.1, 1998. doi:10.1109/ECOC.1998.732666.

[89] Lord Rayleigh F.R.S. Lvi. investigations in optics, with special reference to the spectroscope. *The London, Edinburgh, and Dublin Philosophical Magazine and Journal of Science*, 8(51):477–486, 1879. arXiv:https://doi.org/10.1080/14786447908639715, doi:10.1080/14786447908639715.

[90] Yuan Wang, Ole Krarup, Liang Chen, and Xiaoyi Bao. Frequency sweep extension using the kerr effect for static temperature measurement range enhancement in chirped pulse ϕ-otdr. *Opt. Express*, 29(15):23202–23212, Jul 2021. doi:10.1364/OE.430682.

[91] Yuan Wang, Pedro Tovar, Liang Chen, and Xiaoyi Bao. Generation of high performance optical chirped pulse for distributed strain sensing application with high strain accuracy and larger measurement range. *Opt. Express*, 30(11):18518–18529, May 2022. URL: http://opg.optica.org/oe/abstract.cfm?URI=oe-30-11-18518, doi:10.1364/OE.454913.

[92] Ofer Shapira and Baruch Fischer. Localization of light in a random-grating array in a single-mode fiber. *J. Opt. Soc. Am. B*, 22(12):2542–2552, Dec 2005. URL: http://opg.optica.org/josab/abstract.cfm?URI=josab-22-12-2542, doi:10.1364/JOSAB.22.002542.

[93] Ole Krarup, Chams Baker, Liang Chen, and Xiaoyi Bao. Sensitivity enhancement of fiber optical polarimetric sensors using self-induced nonlinear phase modulation via the kerr effect. *Opt. Express*, 30(9):13985–13993, Apr 2022.

URL: http://opg.optica.org/oe/abstract.cfm?URI=oe-30-9-13985, doi:10.1364/OE.454492.

[94] Marc Wuilpart, Andrei Gusarov, Philippe Moreau, Willem Leysen, and Patrice Mégret. Use of a polarization otdr for the measurement of plasma current in the tore supra thermonuclear fusion reactor. In *Advanced Photonics 2017 (IPR, NOMA, Sensors, Networks, SPPCom, PS)*, page SeW2E.5. Optical Society of America, 2017. doi:10.1364/SENSORS.2017.SeW2E.5.

[95] Zhen Ma and Xiyuan Chen. Fiber bragg gratings sensors for aircraft wing shape measurement: Recent applications and technical analysis. *Sensors*, 19(1), 2019. URL: https://www.mdpi.com/1424-8220/19/1/55, doi:10.3390/s19010055.

[96] Ole Krarup, Chams Baker, Liang Chen, and Xiaoyi Bao. All-optical polarimeter for laser stokes vector measurement using self-induced nonlinear phase modulation. *Opt. Express*, 30(22):40136–40143, Oct 2022. URL: https://opg.optica.org/oe/abstract.cfm?URI=oe-30-22-40136, doi:10.1364/OE.467714.

[97] Thorlabs. *IPM5300*, 3 2008. URL: https://www.thorlabs.com/drawings/8b050d5756be75d8-C5FBB66C-06CE-0978-BCE64B198B955B4B/IPM5300-Manual.pdf.

[98] General Photonics. *PolaDetect, POD-201*, 2015. URL: https://lunainc.com/sites/default/files/assets/files/resource-library/POD-201-v11-9-9-15.pdf.

[99] Jiamin Wu, Xing Lin, Yuchen Guo, Junwei Liu, Lu Fang, Shuming Jiao, and Qionghai Dai. Analog optical computing for artificial intelligence. *Engineering*, 10:133–145, 2022. URL: https://www.sciencedirect.com/science/article/pii/S2095809921003349, doi:10.1016/j.eng.2021.06.021.

[100] T. Bosch, S. Pavageau, D. D'Alessandro, N. Servagent, V. Annovazzi-Lodi, and S. Donati. A low-cost, optical feedback laser range-finder with chirp-control. In *IMTC 2001. Proceedings of the 18th IEEE Instrumentation and Measurement Technology Conference. Rediscovering Measurement in the Age of Informatics (Cat. No.01CH 37188)*, volume 2, pages 1070–1074 vol.2, 2001. doi:10.1109/IMTC.2001.928244.

[101] Donna Strickland and Gerard Mourou. Compression of amplified chirped optical pulses. *Optics Communications*, 56(3):219–221, 1985. URL: https:

//www.sciencedirect.com/science/article/pii/0030401885901208, doi:10.1016/0030-4018(85)90120-8.

[102] Takashi Kato, Megumi Uchida, Yurina Tanaka, and Kaoru Minoshima. High-resolution 3d imaging method using chirped optical frequency combs based on convolution analysis of the spectral interference fringe. *OSA Continuum*, 3(1):20–30, Jan 2020. URL: http://opg.optica.org/osac/abstract.cfm?URI=osac-3-1-20, doi:10.1364/OSAC.381540.

[103] A. J. Rogers. Polarization-optical time domain reflectometry: a technique for the measurement of field distributions. *Appl. Opt.*, 20(6):1060–1074, Mar 1981. doi:10.1364/AO.20.001060.